A STUDY OF STATISTICAL EQUILIBRIUM IN A NUCLEAR SYSTEM AT LOW BOMBARDING ENERGIES

BY

Jeong Ho Lee

A DISSERTATION

Submitted to
Michigan State University
in partial fulfillment of the requirements
for the degree of

DOCTOR OF PHILOSOPHY

Department of Physics and Astronomy

1988

ABSTRACT

A STUDY OF STATISTICAL EQUILIBRIUM IN A NUCLEAR SYSTEM AT LOW BOMBARDING ENERGIES

BY

Jeong Ho Lee

We have studied a reaction of $^{40}Ar + ^{12}C$ at $E/A=8$, 10, and 12 MeV. Fragments ranging from the lithium isotopes to the titaniums were detected at small forward angles ($\theta\approx\pm11°$). Gamma-rays in coincidence with these fragments were also observed. The analysis of source velocities and simultaneous events suggests a characterization of complex fragment emission as a binary-decay process of the compound nucleus. In order to investigate whether the composite system formed from the projectile and the target ever reaches statistical equilibrium, the new temperature measurement proposed by Morrissey et al. has been applied to complex fragments including fragments of $A>10$ for the first time. Temperatures of 2-3 MeV, which roughly agree with those from the Fermi gas model under the assumption of thermal equilibrium, were obtained from the ^7Li, ^7Be, and ^{10}B at $E/A=8$ and 10 MeV, however temperatures from the fragments of $A>10$ show a fluctuation from nucleus to nucleus and also from transition to transition in the same nucleus.

In addition to this, temperatures for most fragments at E/A=12 MeV are lower than those at the lower beam energies. This discrepancy was taken as to be due to the effect of the preferential feeding from the higher-A nuclear unbound states rather than the non-equilibrium effects at this beam energy. For the heavy residual fragments, the observed relative populations of nuclear states are compared with those predicted by the CASCADE statistical model. The result suggests that heavy fragments with masses close to the total mass in the reaction are produced from the compound nucleus by the statistical emission of light particles, such as nucleons and alpha-particles. However, the relative populations of nuclear states for fragments of Z<20 show discrepancies between the observations and the predictions of the statistical model.

To my mother

ACKNOWLEDGMENTS

To my advisor, Dr. Walt Benenson, I owe my deepest gratitude for his guidance, encouragement, and supervision during my graduate career. As a civil engineer and a field-army artillery officer, I had never thought that the transformation to a nuclear physicist would even be possible. However, he made me believe that it was possible, and encouraged me to work hard and finally to finish this work. His patience, depth of vision, sense of humor, and understanding have been greatly appreciated and are acknowledged.

My special thanks go to Dr. David Morrissey for his continuous advice and comments on the work. His help, guidance, and deep knowledge of this field have made the completion of this work possible. In addition, I must thank Dr. Mitsuru Tohyama for his advice and numerous discussions, and Dr. Tetsuya Murakami for his instructions and fruitful discussions about the CASCADE model. There are also many more co-workers and contributors who I must mention for thanks; Drs. R. Blue, C. Bloch, E. Kashy, O. McHarris, and R. Ronningen, and also Y.M. Chen, K. Hanold, M.F. Mohar, and H.M. Xu.

Finally, I must offer special and sincere thanks to Mr. and Mrs. Imsuk Yang. Their interest in me and their care for me during the last four years have been just like family love to me. I also love their kids, Yuree and Sungsang. There are many more names in my heart, and I thank all of you - "Yuruboon, gamsahamnidah!"

TABLE OF CONTENTS

Chapter

LIST OF TABLES

LIST OF FIGURES

CHAPTER I: INTRODUCTION

I.1 Motivation

One of the main goals of intermediate energy heavy-ion physics is to create and study nuclear matter at high temperature and density. In order for this goal to be achieved, it must first be demonstrated that thermodynamic quantities, like temperature and density, are applicable and then that they are in fact measurable in nuclear reactions in this energy range. A key question, therefore, is whether thermal equilibrium is ever achieved in any part of the system. Another one is, if a hot-equilibrated system is produced in a reaction, how it decays into a cooler system.

In order to study the above questions a new method for temperature determination and study of population distribution was proposed by Morrissey and collaborators [Mo84a, Mo85a, Mo86a]. This method was inspired by temperature measurements of stellar surfaces and is essentially a measurement of the production of complex fragments in excited states. In order to test whether the method is in fact applicable to nuclear systems, an experiment [Mo86a] was devised for a low energy compound nuclear system in which thermal equilibrium has been shown to exist, and for which the temperature is known from the Fermi gas model. The results at E/A=8 MeV were consistent with thermal equilibrium at the calculated temperature but included a large correction for the rotational energy of the system, which had to be calculated with a model [Mo86a]. In addition the results of this experiment were limited to a light compound system which emitted light fragments [Mo86a].

This thesis describes a more definitive test of the population method for temperature determination by the utilization of a heavier compound nucleus for which the rotational energy is a much smaller contribution. In addition, the use of reverse kinematics permitted the study of excited heavy complex fragments and also heavy residual fragments for the first time. The energy range covered ranges over the region in which there is a transition from the very well understood compound nucleus into the incomplete-fusion regime, which is much more complex and less well understood.

I.2 Introduction

In low energy heavy-ion collisions, from the neighborhood of the Coulomb barrier up to bombarding energies of E/A=7-8 MeV, complete fusion (full-momentum transfer or formation of the compound nucleus) is a dominant process in the entrance channel. When the projectile energy increases but remains below a few tens of MeV/nucleon, the dominance of the complete-fusion process slowly fades out as the competition between complete and incomplete fusion (incomplete-momentum transfer or deep-inelastic scattering) becomes important. Thus, a multi-dimensional space in the entrance channel which includes the relative velocity [Mo84b, Ch83, He83, Vi82] and distance [Ba74] between two colliding nuclei, the mass asymmetry [Hi87, St85, Mo84b, Ch83, Ro83, Vi79, Ba74], and angular momentum [Hi87, Mo86b, Si86, Mi85, Hu83, Vi82, St77, Br76, Ba74, Co74, Kn60] is needed to characterize these processes.

The decay mode of the composite system formed through complete fusion or incomplete fusion has been well characterized in this relatively low energy regime. Emission of nuclei with masses of four or less (especially emission of protons, neutrons, and alpha-particles) at low beam energy is generally considered to arise from nuclear evaporation after energy thermalization. As the energy increases over the point at which incomplete fusion starts competing with complete fusion in the entrance channel, one can observe in addition light particles that evidently are emitted at an early stage of the reaction, prior to the formation of the composite system. This is known as pre-compound or pre-equilibrium product and is generally considered to be a forward-peaked high energy component [Mo85b].

Heavy residual fragment emission, which is connected to very light particle emission, is well characterized as the formation of evaporation residues and as the main decay mode of the compound nucleus with mass lighter than A=100 [Mo84b] in low energy reactions. For the higher projectile energies one must deal with the competition between the evaporation and the fission in the decay of the compound system because of the dramatic lowering of the fission barrier with increasing angular momentum [Co74, Pl74]. The production of evaporation residues at higher energies, therefore, is limited by angular-momentum-dependent fission competition. Incomplete fusion will commonly take place in a wide range of linear momentum transfers, hence the array of final states is expected to be doubly complicated by the combination of the entrance and exit channel effects. Since the two different processes for forming the composite system, complete fusion and incomplete fusion, are often indistinguishable from each other, some difficulties in experimentally defining the complete fusion process for heavy residual fragment emission arise as the beam energy increases. The general difficulties in the measurement of evaporation residue velocities to determine the average linear momentum transfer to the composite system and in the measurement of the angular correlations between the emitted complex fragments (or fragments with masses intermediated between the alpha-particle and the symmetric-fission products) to provide the information about the possible fission mechanism have been nicely avoided by employing a reverse-kinematics reaction [Ch87a, Hi87, Mo86b, Mi85, Mo84b, So84] and by characterizing the emission of complex fragments as a binary-decay process of the composite system [Ch86a, Mc85, So83].

Symmetric fission reactions which follow fusion processes and produce fragments close to one-half the mass of the composite system are traditionally observed in heavy systems. In light systems ($A \leqq 100$), in which the fissility parameter is smaller than the so-called Businaro-Gallone limit [Bu55], the distribution of fission products will be governed mainly by the mass, charge, and angular momentum of the composite system. The dependence on the fissility parameter and the role of the Businaro-Gallone point have been studied in Refs. Gr84 and So84. Different results from the two references may be combined to propose that below the Businaro-Gallone point the expected yields monotonically decrease toward symmetry, while at larger angular momenta, which lowers the Businaro-Gallone limit below the fissility parameter, a peak in the yield is expected at symmetry. This indicates that in higher energy reactions, within the critical angular momentum, the yield at symmetry will become larger than at lower energy [Mo87, Mo88]. One can also notice that production of the heavy complex fragments (especially close to the symmetric-fission products) via an incomplete-fusion process is less likely than that via a complete-fusion process because the pre-equilibrium light particles, in general, carry away a great amount of the orbital angular momentum in the entrance channel. Hence, the composite system has a much lower fraction of the angular momentum and a lower excitation energy than the completely fused system [Mo86b, Mi85]. The angular momentum effect on the distribution of the fission products can be associated, in a somewhat different manner, with a statistical emission theory developed by Moretto [Mo75]. A model introduced in Ref. Mo75 predicts that complex fragments with masses between alpha-particles and symmetric fission fragments must be emitted, although with lower probability compared to the yields of the heavy residual fragments and the very light particles, by decay of the compound nucleus. The standard evaporation formalism and the fission decay formalism are nicely combined in this model to describe the transition from the very light-particle emission to the emission of a very sizable fragment of the mass of symmetric-fission products. Hence the light complex fragments (but still $Z>2$) can be produced by both the evaporation and the fission process of the compound nucleus.

On the other hand, composite systems are often characterized as thermally equilibrated hot zones with a temperature (usually called "kinetic" temperature) which is obtained by fitting simple Maxwell-Boltzmann distributions to particle singles inclusive spectra. The concept of an equilibrated zone of nuclear matter has been also extended to the relativistic heavy-ion collisions by introduction of the "fireball" model [We76, Go78]. Evidence of the existence of a common moving source has been presented in a measurement of intermediate-rapidity light fragments in the intermediate energy range [Ja83, Ch83]. This broadly extended theory of the formation of a thermalized hot zone combined with the characterization of compound-nucleus emission of complex fragments [Ch86a, Mc85, So83] in the heavy-ion reactions has been widely accepted in studies of statistical equilibrium of the nuclear system at various energies. One of the most relevant methods to obtain information concerning the statistical behavior of the nuclear matter, therefore, is to measure the particle singles inclusive spectra for the light fragments, which may be emitted at longer time evolution, hence giving information about space-time extent, velocity, and energy involvement of the highly excited nuclear systems (or moving sources). The moving source fit [We82, Ja83] has been commonly used for reactions at various energies [e.g. Ch86b, Fi86, Po85, Fi84, We84], and evidence for more than one moving source, such as target-like slow moving source, intermediate-rapidity moving source, or projectile-like fast moving source, has been obtained as well. The temperatures deduced from this moving source fit generally exhibit a systematic dependency on bombarding energy, as expected, but not on the fragment mass.

A recently introduced nuclear temperature measurement by Morrissey et al. [Mo84a, Mo85a] has given another insight into the reaction mechanism. In this new technique, it is suggested that nuclear temperature also can be characterized by the relative population of bound states of light complex fragments (Li, Be) in nuclear reactions. The observed populations of the excited states at intermediate energy reactions, however, show that the deduced temperatures are significantly lower than those obtained from the kinetic energy distributions of the fragments. This similar discrepancy has been shown by other authors [Po85, Xu86, Ch87c], some of whom have extended this technique to the measurements of population of the particle unbound states in similar fragments [Po85, Ch87c]. This surprising result may imply that equilibrium is never achieved in this energy range. More complicated, but not unambiguous, explanations for this discrepancy have been presented; for example, preferential feedings to certain states from the particle unbound states in the higher-A nuclei [Mo85a, Mo84a, St83, Ha87, Ha88] and final state interactions among the expanding nuclei and nucleons [Bo84]. However, the corrections on these possible effects are not well known experimentally.

Morrissey et al. [Mo86a] has discussed the new temperature measurement more widely by the introduction of the average thermal temperature, which was calculated from the Fermi gas model and compared to the results obtained from reactions over a wider energy range (6.25 MeV $<$ E/A $<$ 25 MeV). Over this energy range, the major entrance channel process changes dramatically from complete fusion to incomplete fusion as the energy increases [Go84, St77]. In this measurement, populations of nuclear states are found to be distributed according to the average thermal temperature, which is described in Ref. Mo86b, at bombarding energies up to around E/A=8 MeV. However the population distributions appear to be much lower than the calculated values at energies of E/A=12 MeV and higher. The agreement of the two temperatures (the observed and the calculated) below E/A=8 MeV implies the formation of an equilibrated system. However, a correction for the fraction of the average rotational energy to the total excitation energy in a nuclear reaction must be made since it plays an important role in populating the light fragments. The latter can be studied further by comparing two different reactions, heavier and lighter systems, at similar energies, while the question on how the "kinetic" temperature is related with the population distribution of light fragments [Ch87c] remains as a complicated problem which is yet to be solved.

In this thesis we report the results of measurements for the reaction ^{40}Ar + ^{12}C at E/A=8, 10, and 12 MeV. The present experiment was performed as a continuation of a study of the thermal population of nuclear states reported in Ref. Mo86a. A heavier system (relative to that in Ref. Mo86a) was employed in the present experiment to study the importance of the rotational energy fraction on the nuclear temperature. Reactions at E/A=8, 10, 12 MeV may show very rapid changes in reaction mechanism at early stages of the collision, and studies of the light particle emission can provide valuable information concerning statistical equilibrium. Inclusion of the measurement at E/A=10 MeV was necessary in order to complement the large difference in the characteristic of the relative populations of the excited states between E/A=8 and 12 MeV, which is presented in Ref. Mo86a. The use of reverse kinematics avoids, in general, the detection of projectile-like light fragments and direct-reaction products. This may be compared to the normal kinematics, in which there exists the favored detection of fast-moving quasi-elastic or inelastic scattering light fragments. In addition, reverse kinematics permitted the detection of a large number of complex fragments as well as the heavy residual fragments in the present experiment. The detection of the heavy residual fragments and the clear identification of these fragments by charge for this reaction provided some advantages in studying the fusion process in this energy range. Gamma-rays in coincidence with fragments ranging from lithiums to titaniums were detected at all the projectile energies. The detection of gamma-rays in coincidence with the individual intermediate fragments ($12 \leq A \leq 23$) was possible owing to the excellent particle identification provided by the silicon surface barrier particle telescopes.

Experimental details are given in Ch. II. Particle singles inclusive spectra are presented in Ch. III. Evidence of the statistical-binary decay of the complex fragments is given by presenting the "peak-velocity" diagrams and results from the simultaneous events. In Ch. IV, the results for the population distribution of nuclear states for the complex fragments ($3 \leq Z \leq 11$) are presented. The first attempt to apply the new nuclear temperature measurement to the much heavier fragments ($A > 10$) is described in this chapter. Gamma-ray intensities measured in coincidence with heavy residual fragments are compared, for the first time, with the statistical model calculation in Ch V. Finally, summary and conclusions are presented in Ch. VI.

Throughout this thesis, the "light fragments" refer to the fragments with masses between the alpha-particle and the target nucleus (^{12}C). The "intermediate fragments" represent the fragments intermediate between the target nucleus and the projectile nucleus (^{40}Ar). However, for the practical reason, isotopes of Ar, Cl, and S are referred as the "heavy residual fragments", which are defined as fragments that may be evaporation residues from the composite system. "Light fragments" and "intermediate fragments" are often referred as "lighter complex fragments" and "heavier complex fragments", respectively, or the "complex fragments" altogether.

CHAPTER II: EXPERIMENTAL

II.1 Experimental Set-up

Mass fragments ranging from Z=3 to Z=22 were produced by the interaction of argon ions with a carbon target. Beams of 320 MeV $^{40}Ar^{6+}$ ions, 400 MeV $^{40}Ar^{7+}$ ions, and 480 MeV $^{40}Ar^{7+}$ ions were provided by the K500 cyclotron of the National Superconducting Cyclotron Laboratory at Michigan State University. The cyclotron periods were 107.558 ns, 95.934 ns, and 87.712 ns, respectively. The target was a self-supporting foil of ^{12}C, 490 μg/cm² thick. The target was mounted in an aluminum target ladder inside the scattering chamber with its plane at 45° relative to the beam. The chamber had 12 ports every 30° starting from 0° with the same vertical level. The beam entered through the open 180° port and exited through the open 0° port. The ports at 120° and 240° had 8.5cm x 19.5cm cylindrical aluminum cups with the center lines centered on the target, and the end of each aluminum cup was about 6 cm away from the target (see Figure II.1.1b). The rest of the ports had either a clear Lucite window or a Lexan plate with high-vacuum electronic feed-throughs. An arm was located at about 2 cm above the table inside the chamber, and both could be rotated from the outside the chamber. The beam was stopped in a Faraday cup, which was approximately 3.2 m downstream and was surrounded by water and lead shielding. The beam intensity was generally between 5 and 10 nA. Such a low beam intensity maintained the count rates of the gamma-ray detectors below 20,000 per second and thereby avoided count-rate dependent gain shifts.

Charged particles (Z>2) were detected in a set of three element silicon surface barrier telescopes each with a 50 mm^2 area. The events with Z=1 and Z=2 were rejected in a Motorola 68000 based system [Va85]. Telescopes were located inside the chamber approximately at the azimuthal angles of $\theta = \pm 11°$ relative to the beam and the polar angles of $\phi = \pm 4°$ [$(\theta,\phi)=(-11°,-4°)$, $(-11°,4°)$, $(11°,-4°)$, and $(11°,4°)$ for Tel-1, 2, 3, and 4, respectively]. This relatively small angle with respect to the beam line was used to optimize the count rate for the reverse kinematics while avoiding the detection of projectile fragments or direct reaction fragments by keeping the angles bigger than the classical grazing angle $\theta=6°$. Two telescopes at the same azimuthal angle were in one aluminum mount, which had provisons for liquid cooling. Refrigerated alcohol was run through the mounts to cool the detectors approximately to -20°C throughout the experiment. The three elements (Δ_1E-Δ_2E-E) of each particle telescope were 30 μm, 75 μm, and 1000 μm thick, respectively. Approximately 0.1 mg/cm^2 thick gold cover foils were placed on the collimators of the particle telescopes to reduce the number of electrons hitting the silicon detector. All of the four particle telescopes were placed approximately 20.3 cm from the target. The effective solid angle of each particle telescope was approximately 870 μsr. The particle identification of the particle telescopes was excellent for isotopes with charges up to Z=11, however only the Z-identification was possible for the heavier fragments (Z>11).

A set of eight NaI(Tl) scintillation detectors, 7.6cm x 7.6cm right cylinders, and a pair of Ge counters, 4.71cm x 4.36cm cylinders, were used to detect gamma-rays in coincidence with the particles. Eight NaI(Tl) scintillation detectors are placed on the domed lid of the scattering chamber with the azimuthal angles, $\Theta = \pm 20°$, $\pm 60°$, $\pm 120°$, and $\pm 160°$, and the same polar angle, $\phi = 49°$. Two Ge counters were placed at $\Theta = \pm 120°$ in a horizontal plane ($\phi = 0°$). A schematic diagram of the experimental setup is shown in Figure II.1.1. The Ge counters were cooled down by liquid nitrogen to approximately -196°C throughout the experiment. The resolutions of NaI(Tl) scintillation detectors were equal to 9.4% or less at $E_\gamma = 570$ KeV, and those of Ge counters were about 0.45% or less at the same gamma-ray energy. This good resolution for the germanium counters was necessary to identify the gamma-ray lines from the heavy residual fragments and to determine accurately the number of counts in those gamma-ray peaks. Since heavy residual fragments are slower moving sources ($\langle v \rangle \approx 0.1$ c) than the complex fragments, the Doppler Shift corrections for these fragments are relatively small. Therefore, errors which arise from the Doppler broadening due to the finite solid angles in the gamma-ray detectors will be also small. The NaI(Tl) scintillation detectors provided sufficient statistics in the gamma-ray energy spectra for most of the complex fragments. Even though the relatively poor resolution for the NaI(Tl) scintillation detectors makes it difficult to separate closely spaced gamma-ray lines, the bigger total detecting efficiency as compared to the Ge counters ($\varepsilon = 3.5\%$ at $E_\gamma = 430$ KeV while Ge counter had a total efficiency of 0.45% at the same gamma-ray energy) was essential in the detection of the gamma-rays in coincidence with complex fragments which have much lower yields than the heavy residual fragments. The gains of the gamma-ray amplifiers were set to observe a maximum gamma-ray energy of about 2.2 MeV.

II.2 Electronics

A schematic diagram of the basic electronics for the particle telescopes and the gamma-ray detectors is shown in the Figure II.2.1. ORTEC AD811 analog-to-digital convertors (ADC's) were used to digitize the pulse heights of the signals for the silicon detectors and the NaI(Tl) scintillation detectors, and 400MHz ADC Model 7420/G's were used for the Ge counters. The time information was recorded for all the detectors by using LeCroy 2228A time-to-digital convertors (TDC's).

A coincidence between Δ_1E and Δ_2E or Δ_2E and E silicon elements was required to get a valid particle telescope event. The valid event for Ge counters and that for NaI(Tl) scintillation detectors were formed separately, and at least one of the each gamma-ray detector type was required to fire. The particle singles mode was triggered by the particle telescopes only. The particle-gamma coincidences modes were triggered by the simultaneous event of at least one of the four particle telescopes and at least one of the ten gamma-ray detectors. The gamma-gamma coincidence mode, which was employed in the efficiency calibration of the gamma-ray detectors, was triggered by the simultaneous event of at least one of the eight NaI(Tl) scintillation detectors and at least one of the two Ge counters.

Selection of the mode was made between runs on a coincidence module. When this master gate coincidences mode was "true", and the computer signal "not busy" was present, the digitized pulse height, the time information, the integrated beam current signal, and the timing of the master gate against the cyclotron RF were recorded. A scaler buffer was made at every 3 minutes throughout the entire experiment. These

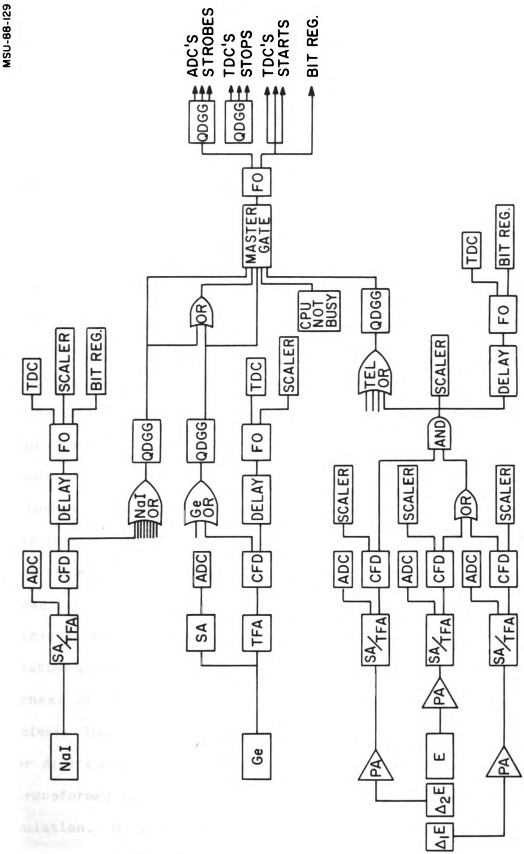

Figure II.2.1 Electronics Schematic.

buffers were sent to a Vax 11/750, and they were written to tape at 6250 bpi. Program SARA was used to sample the buffers during the experiment.

II.3 Calibration

An energy calibration was obtained for each silicon detector with pulsers and two alpha-sources (^{212}Pb and ^{249}Cf). The linearity of the electronics was checked with the pulsers four times during the experiment. Extra data for the calibration were taken right after the experiment with the gains increased by a factor of 3 for the Δ_1E and Δ_2E silicon detectors, and by a factor of 5 for the E silicon detectors. This new gain was set in order to get the alpha-lines on scale (^{212}Pb has alpha-particle lines of 6.051, 6.090, and 8.784 MeV, and ^{249}Cf has an alpha-particle line of 5.812 MeV, all of which are very close to the threshold set for the silicon detectors under the original gains for the experiment). Only the 8.784 and 5.812 MeV alpha-particle lines were used in this calibration because the 6.051 and 6.090 MeV alpha-particles are too closely located and also had too little statistics in comparison to those for the other two. A linear fit between the known alpha-particle energies and the observed channel numbers determined the calibration at the higher gains (except the Δ_1E silicon element, the thickness of which, 30 μm, was too thin to stop 8.784 MeV alpha-particles). Then, this calibration determined the energies for the pulser dial's readings at the same gains, and, finally this calibration was transformed to the original gains after a simple algebraic manipulation. More specifically, if the pulser dial's reading (PD) is defined as $PD=A_H+B_H\bullet Ch$ in the higher gains and $PD=A_L+B_L\bullet Ch$ in the original gains with Ch representing the channel number, and also if the energy in the higher gains is defined as E=A+B•Ch from the calibration of the alpha-lines, then the energy in the original gains can be expressed by

$$E = \left[A+\frac{B}{B_H}(A_L-A_H)\right] + B\frac{B_L}{B_H}\bullet Ch\ . \qquad (II.1)$$

A schematic explanation for this procedure is shown in Figure II.3.1. The superimposed lines are from the best linear-fitting for the data. The lowest-lying line represents the alpha-calibration. Geographically, this line can be transformed by rotating and shifting into the middle line which represents the pulser dial scale in terms of the channel number. After that, it can be transformed in the same sense into the the top line which represents the pulser dial scale at the original gain. A calibration for Δ_1E silicon detectors followed the same routine except for borrowing the calibration from the Δ_2E silicon detectors for the lower gains. This calibration was checked by generating a two-dimensional particle identification spectrum ($\Delta_1E+\Delta_2E$ vs E), and the particle separation in the spectrum was much clearer than that obtained simply by using the linear fit between the reading of the pulser dial and the observed pulse height. Two-dimensional particle identification spectra for the light fragments, the intermediate fragments, and the heavy residual fragments will be shown in Ch. III (Figures from III.1.1 to III.1.3c).

The energy calibration of the NaI(Tl) scintillation detectors and the Ge counters was performed several times throughout the experiment with gamma-ray sources. The Ge counters had very consistent calibrations, whereas the NaI(Tl) scintillation detectors had some drift problems, but the changes were within the resolutions of the detectors except the NaI(Tl) scintillation detector at $\Theta = -120°$, which was excluded from the analysis.

The detection efficiency calibrations of the Ge counters were obtained with a ^{152}Eu gamma-ray source (standard reference material 4218-C, National Bureau of Standard). The efficiency calibrations of the NaI(Tl) scintillation detectors were obtained with a gamma-gamma coincidence method using gamma-ray sources: ^{60}Co, ^{134}Cs, and ^{207}Bi. These gamma-ray sources have two prominent gamma lines with one following the other as a sequence. A gamma-ray singles mode run for the Ge counters was carried out for each gamma-ray source, and the excellent resolution of the Ge counter provided two sharp gamma-ray peaks for each source in the gamma-ray energy spectrum. Then, a gate was put in the preceding gamma-ray peak in the Ge-counter gamma-ray energy spectrum, and the sequential gamma-ray was observed in the NaI(Tl) scintillation detectors in the gamma-gamma coincidence mode. Multiple chance events of the preceding gamma-rays were subtracted from the sequential gamma-ray counts according to the assumed efficiency conversion factor and was iterated after the resulting efficiency calibration. Angular distribution effects were negligible after summing the efficiencies to get the total efficiency for the NaI(Tl) scintillation detectors. A reverse way of the coincidence calibration, by putting a gate in the sequential gamma-ray peak and observing the preceding gamma-rays, was also performed in order to check the efficiency calibration. These three gamma-ray sources gave the efficiencies for the gamma-ray energy

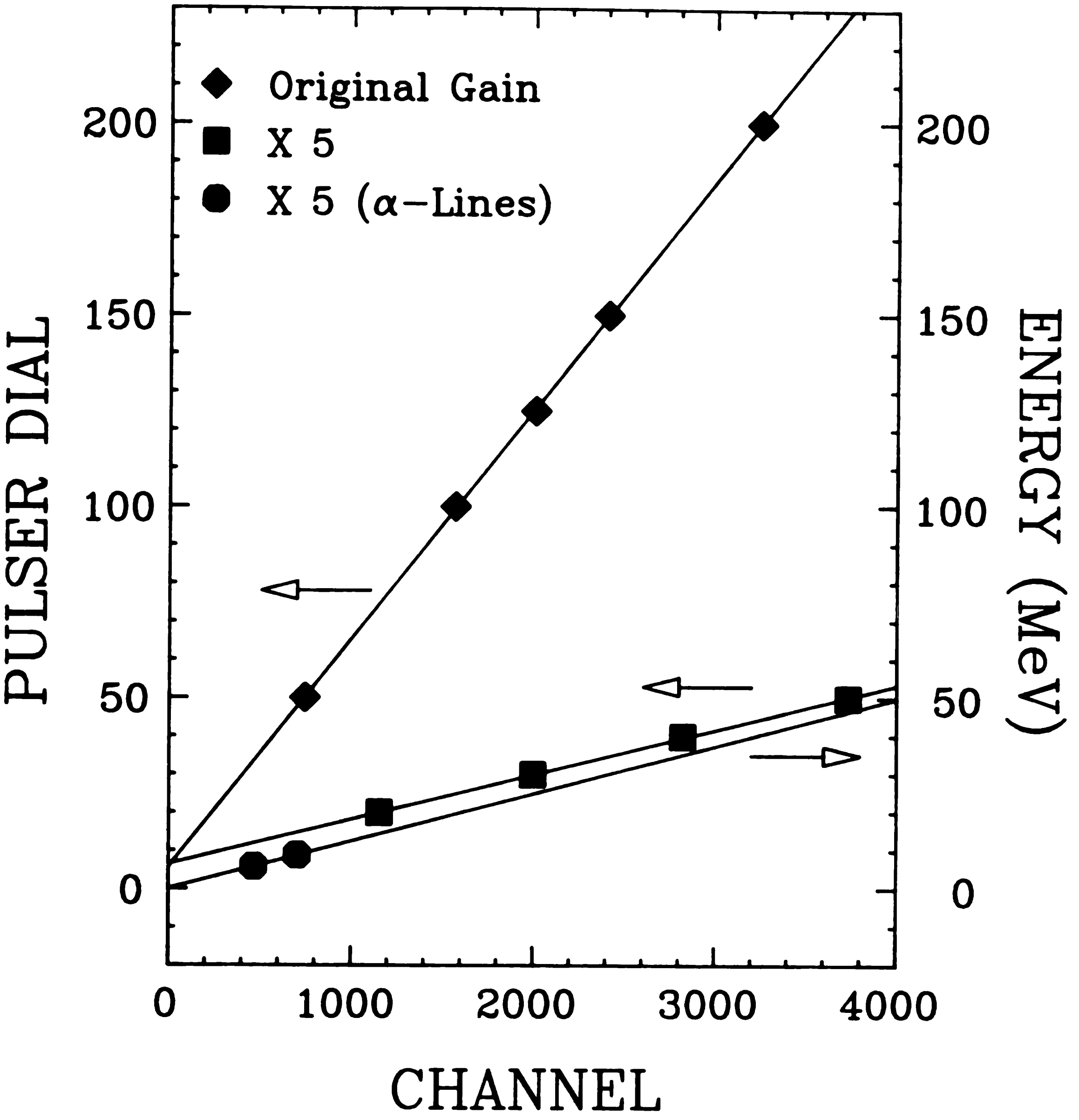

Figure II.3.1 Schematic of Si-element calibration.

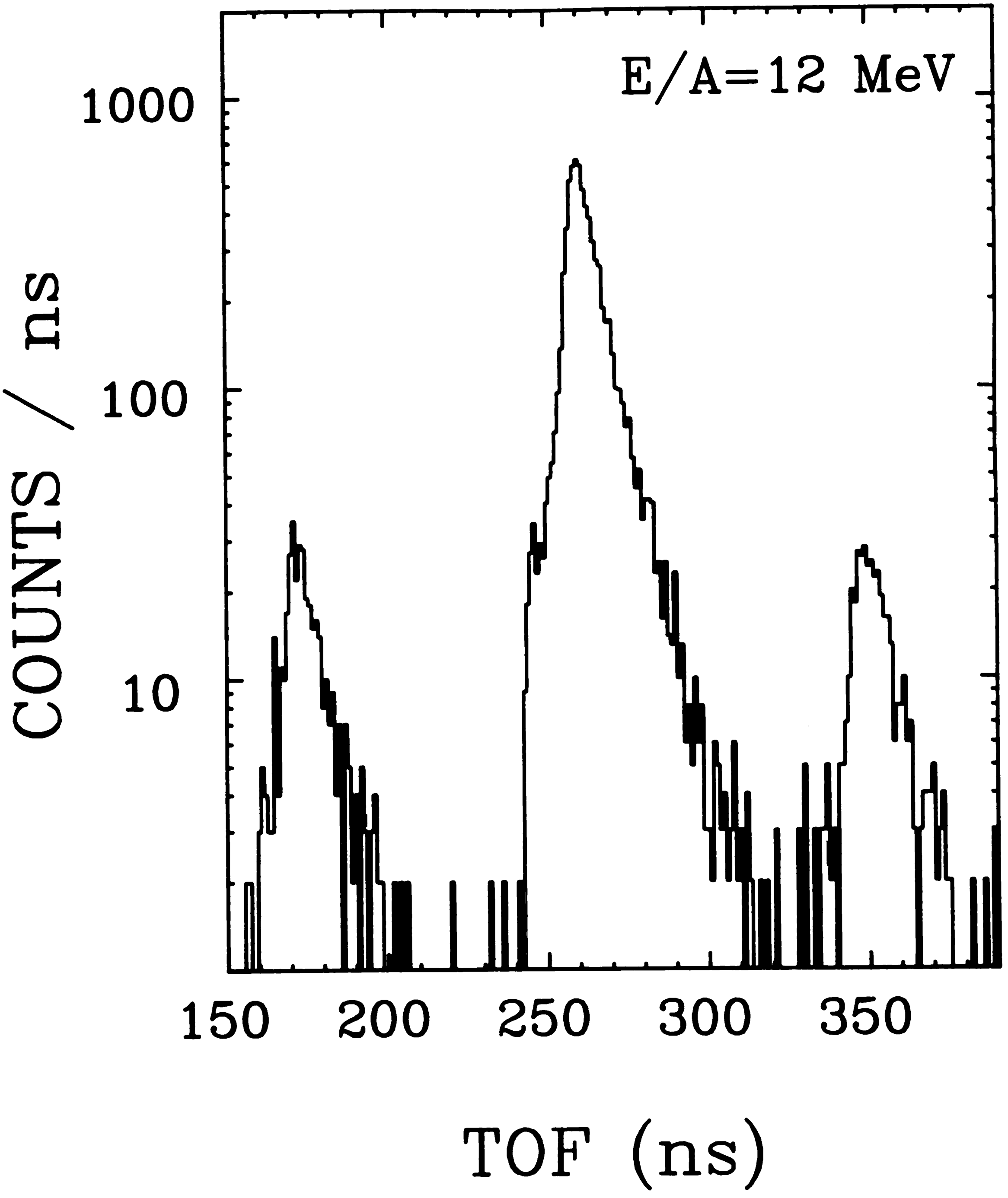

Figure II.3.2 Time-of-flight spectrum for gamma-rays in the NaI(Tl) detector at θ=20° in coincidence with ^{10}B fragments in any telescopes, E/A=12 MeV.

above 570 KeV. A gamma-ray singles run with the NaI(Tl) scintillation detectors was performed later on with a ^{166m}Ho multi-gamma-ray source to provide the shape of the efficiency curve for E_γ<570 KeV region, and the two curves were joined smoothly to give the efficiencies for the entire gamma-ray energy region.

The TDC's were calibrated by comparing the periodicity of the time-of-flight (TOF) histogram to the period of the cyclotron. Figure II.3.2 shows a TOF histogram for gamma-rays in the NaI(Tl) scintillation detector at the angle (Θ=20°, ϕ=49°) in coincidence with ^{10}B fragments for E/A=12 MeV. The ratio of a real-to-random coincidence was approximately 18:1 at this beam energy (typically it was about 35:1 at E/A=8 MeV and 25:1 at E/A=10 MeV). The average number of channels between the prominent peaks for each TDC was set equal to the cyclotron period, and this determined the TDC calibration, which was 0.25 ns/channel in the 2^{11} channel scale.

II.4 ^{8}Be Contamination in the ^{7}Li Singles Spectra

It is well known that particle singles spectra of ^{7}Li are contaminated by the production of the ground state of ^{8}Be and its subsequent α-α decay [Wo72, Bl86]. The Q-value of the ^{8}Be ground state decaying into a pair of alpha particles is 92 KeV, which is very low compared to half the typical total kinetic energy of 100 MeV, provides a very low relative kinetic energy between alpha particles. This indicates that there exists a very high probability for both α's from the ^{8}Be fragment to be detected simultaneously in a particle telescope. As discussed in Ref. Bl86, when two α's pass through a silicon element, they will lose the kinetic energy in a very similar way to that of a ^{7}Li, hence contaminating all the ^{7}Li singles inclusive kinetic energy spectra.

The evaluation of the contaminant fraction required a theoretical estimate of the ^{8}Be yield because of the lack of experimental data needed to employ the method suggested in Ref. B186. A statistical method was employed for this calculation. In a chemically equilibrated composite system, the population of nuclear states in the decay products is assumed to be relevant to the Boltzmann distribution with the excitation energy and the spin of the state and the chemical potential [To88, Ha87]. Therefore the total cross section of a nucleus produced from this system can be written as

$$\sigma \propto \sum_i (2j_i+1)\, e^{-\frac{B.E.+E_i-\mu_Z Z-\mu_N N}{\kappa T}} , \qquad (II.2)$$

where j_i and E_i are the spin and excitation energy of the state i, B.E. is the binding energy of the ground state of the nucleus, μ_Z and μ_N are the chemical potentials for proton and neutron, respectively, Z and N represent the numbers of protons and neutrons, respectively, and κT is the temperature of the system. The summation in i is over the states that decay into the ground state of the same nucleus. In comparison with the assumption that the fragment distributions depend mainly on the ground state properties of the emitted nuclei [So84, Mc85], the characteristic structures [Ha88, Ha87, Fi84, St83] are taken into account in Eq. IV.7 to formulate an expression of the relative population for a nuclear system. However feedings to the bound states from the particle unbound states in the high-A nuclear system [Ha88, Ha87, Fi87, Mo85a, Mo84a, St83], which will be discussed in Ch. IV, are not taken into consideration in this calculation.

Since the chemical potential and the temperature are the only unknown parameters in Eq. II.2, one needs only two cross sections or more to solve this equation if one is to deal in a same type of isotopes. We used the three cross sections of ^{7}Be, ^{9}Be, and ^{10}Be which are obtained in the present experiment. The result of the best fit is given in Table II.4.1. The temperatures of 2.6 MeV at E/A=8 MeV and 3.2 MeV at E/A=10 MeV are consistent with those from the Fermi gas model [shown in Ch. III], while the chemical potentials slightly differ from each other. Finally a Monte Carlo simulation [Bl86] was carried out to evaluate the probability of two alpha particles from the ground state of ^{8}Be entering the particle telescope simultaneously. The shape of the kinetic energy spectra of ^{8}Be was borrowed from that of ^{9}Be to consider the effect of the the punch-through problems in the ^{7}Li spectra on the evaluation of the contamination. The estimated contamination of the ^{8}Be on the ^{7}Li spectra were 10% at E/A=8 MeV and 4% at E/A=10 MeV. The ratios of the cross sections at E/A=12 MeV were not available because of the punch-through problems of the fast moving fragments. Nevertheless the estimated value at E/A=12 MeV was roughly about 1%, and this was statistically negligible. The changes in the deduced temperatures were from 1.1 MeV to 2.2 MeV at E/A=8 MeV and from 1.8 MeV to 2.4 MeV at E/A=10 MeV, however these were comparable to the statistical errors at the both cases. This relatively small contamination (compared to 50% in Ref. Bl86 and 70-90% in Ref. Mo86a) was mainly due to the smaller solid angles in the particle telescopes (we used ~0.9msr solid angle for each telescope, while solid angles in Ref. B186 were 5-22msr and those in Ref. Mo86a were approximately 24msr).

Table II.4.1 Evaluation of contamination of the ^{8}Be ground state in the ^{7}Li singles spectra.

E/A (MeV)	$R\left(\frac{^{7}\mathrm{Be}}{^{9}\mathrm{Be}}\right)$	$R\left(\frac{^{10}\mathrm{Be}}{^{9}\mathrm{Be}}\right)$	κT (MeV)	μ (MeV)	$R\left(\frac{^{8}\mathrm{Be}}{^{9}\mathrm{Be}}\right)$	Contamination
8	0.25	0.28	2.6	-8.65	2.4	10%
10	0.36	0.36	3.2	-8.95	1.4	4%

CHAPTER III: PARTICLE SINGLES

III.1 Data Analysis

The three-element silicon particle telescope provided a number of options for observing the yield in the different mass regions; (1) light fragments ($Z<6$), which include Li, Be, and B, (2) intermediate fragments, which refer to isotopes of C, N, O, F, Ne, and Na in this paper, (3) heavy fragments, which include isotopes of Mg, Al, Si, P, S, Cl, Ar, K, Ca, Sc, and Ti. Although some of heavy fragments are lighter than the projectile nucleus ^{40}Ar, this classification was chosen for convenience. The term "complex fragments" refers to both the light fragments and the intermediate fragments.

We obtained excellent particle identification for the individual light and intermediate fragments with charges $Z=3$ to $Z=11$ by generating two dimensional particle identification spectra. Isotope separation by Z only was obtained for fragments with $Z>11$, which leaves the identification within a given element unresolved for this heavy mass region. A spectrum of $\Delta_1E+\Delta_2E$ vs. E_{TOT} for the light fragments is shown in Figure III.1.1, and that for the intermediate fragments is shown in Figure III.1.2. Figures III.1.3(a-c) show two-dimensional spectra of Δ_1E vs. Δ_2E at E/A=8, 10, and 12 MeV, respectively. Unfortunately, the Z-separation of the heavy residual fragments is poorly displayed in these figures.

Even though a relatively large range of masses was observed with good identification, a number of problems arose from the limited energy range allowed by the gains in the silicon elements and also from their thicknesses. First, the total thickness of 1105μm in the three silicon element telescope was enough to stop the relatively fast moving light fragments, such as lithium and beryllium isotopes. As shown in Figure III.1.1, punch-through problems appear for some of the light fragments, and this limited the statistics for those fragments since the high energy part was missing. Secondly, the energy range in the Δ_2E-detector was too low to detect majority of the slow-moving intermediate fragments and most of the fast-moving heavy residual fragments. The energy range in the Δ_1E-detector was set to cover the entire mass range. Meanwhile, the maximum energy range set in the Δ_2E-detector was far below that required to utilize most of the intermediate and heavy residual fragments detected in the present experiment, as shown in Table III.1.1. The energy ranges of each silicon element for the particle telescopes are given in the part a) of the table. Part b) of Table III.1.1 shows the calculated energy losses in each silicon element for the predicted peak-velocity energies for both backward-scattering and forward-scattering fragments (in the center-of-mass frame) at E/A=10 MeV. As predicted from the calculation, the saturation of signals in Δ_2E amplifier for the fast-moving heavy residual fragments (especially for Z>12) are seen in Figures III.1.3(a-c). This means that the recorded kinetic energies of those fragments do not represent the real energies lost in the detectors. The peak velocity of the backward-scattering fragments in the center-of-mass frame was not expected to be observed for most of the fragments because of the threshold set in the detectors.

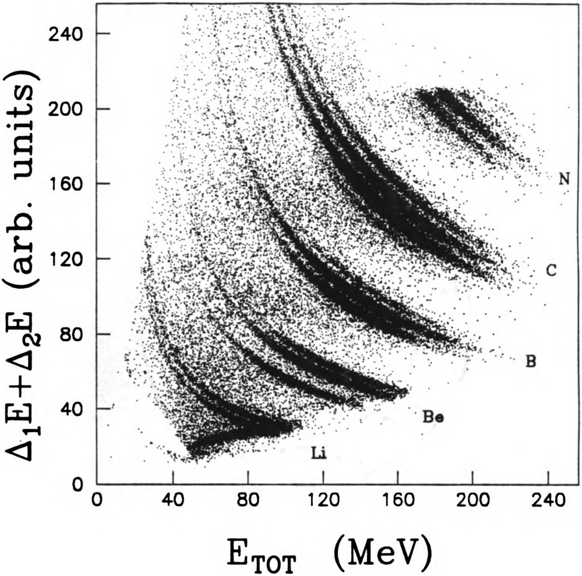

Figure III.1.1 $\Delta_1E+\Delta_2E$ vs E light fragment PID spectrum (Tel-2).

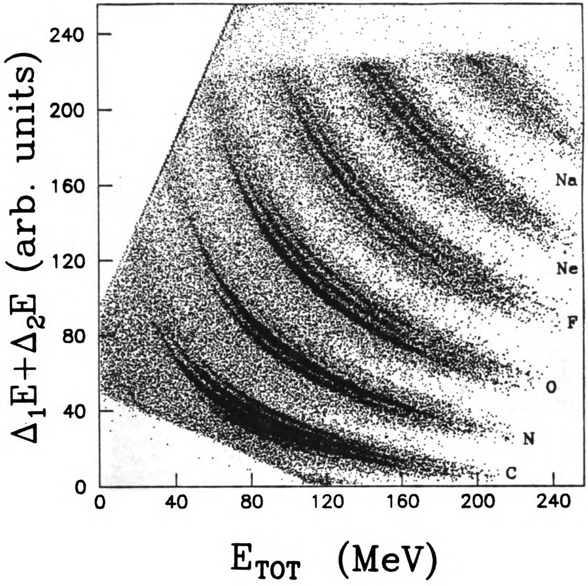

Figure III.1.2 $\Delta_1E+\Delta_2E$ vs E intermediate fragment PID spectrum (Tel-2).

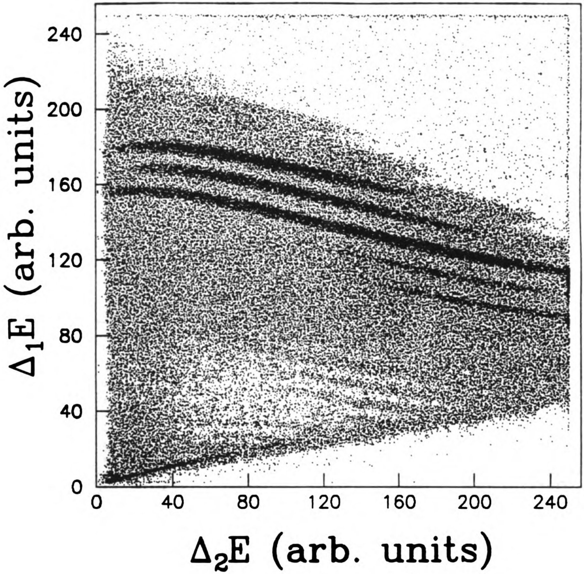

Figure III.1.3 Δ_1E vs Δ_2E PID spectra (Tel-4). a) At E/A=8 MeV.

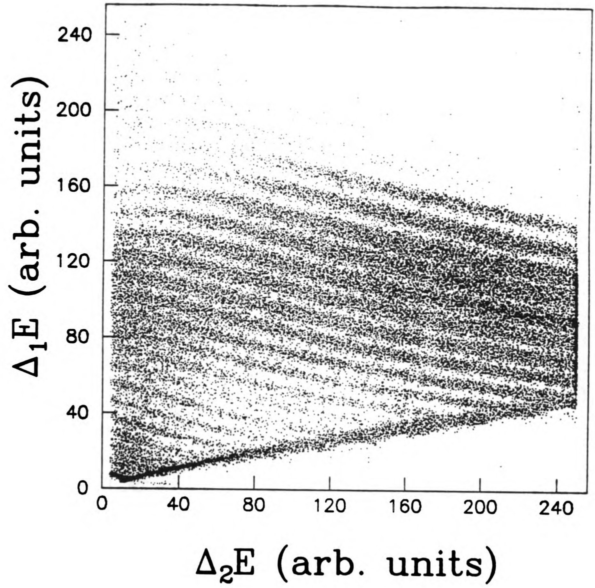

Figure III.1.3 (cont'd.) b) At E/A=10 MeV.

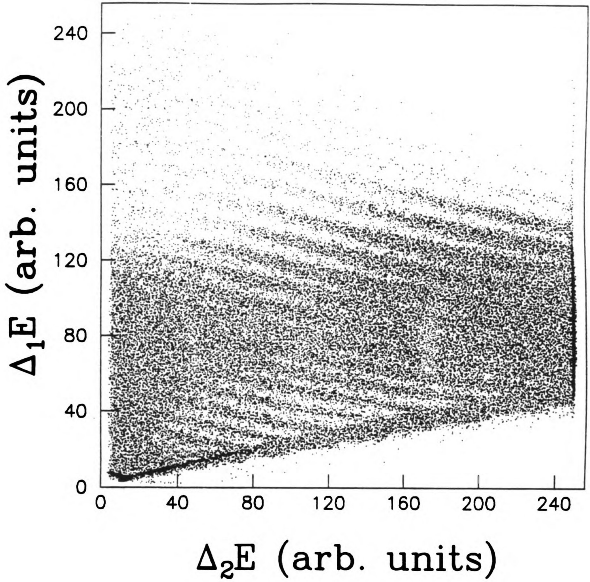

Figure III.1.3 (cont'd.) c) At E/A=12 MeV.

Table III.1.1 Detection of fragments. a) Energy ranges (units in MeV).

Telescope No.	Δ_1E	Δ_2E	E
1, 2, and 3	195	100	260
4	195	183	260

Table III.1.1 (cont'd.) b) Predicted kinetic energy and energy loss at E/A=10 MeV, θ_{lab}=11° (units in MeV).

	Backward Scattering					Forward Scattering				
Isotope	<KE>	Energy Loss				<KE>	Energy Loss			
		Δ_1E	Δ_2E	E	Total		Δ_1E	Δ_2E	E	Total
^{7}Li	5	5	0	0	5	107	2	4	84	90
^{7}Be	3	3	0	0	3	120	3	7	109	120
^{10}B	8	8	0	0	8	152	4	12	136	152
^{12}C	11	11	0	0	11	175	7	17	151	175
^{14}N	15	15	0	0	15	195	10	25	160	195
^{16}O	20	20	0	0	20	213	13	35	165	213
^{19}F	30	30	0	0	30	234	17	50	167	234
^{21}Ne	38	38	0	0	38	247	22	65	160	247
^{23}Na	47	47	0	0	47	258	26	75	157	258
^{25}Mg	57	57	0	0	57	266	32	97	137	266
^{27}Al	69	69	0	0	69	272	39	125	108	272
^{29}Si	83	83	0	0	83	276	47	160	69	276
^{31}P	99	96	3	0	99	277	56	202	19	277
^{34}S	126	106	20	0	126	276	67	209	0	276
^{36}Cl	151	112	39	0	151	268	79	189	0	268
^{38}Ar	184	115	69	0	184	252	95	157	0	252
^{41}K 1)						233	114	119	0	233
^{43}Ca						245	124	121	0	245
^{45}Sc						257	133	124	0	257
^{47}Ti						268	143	125	0	268
^{50}V						285	152	133	0	285

1) Given value for the nucleus of ^{41}K or heavier represents the predicted average energy as an evaporation residue. See the text.

Data from the particle-singles runs with telescope-4, which had a larger energy range in Δ_2E, were crucial in determining the peak velocities, and also better statistics were provided by the telescope-4 for the coincidences runs. None of the heavy residual fragments reached the last silicon element (E) in the present reaction, and most of the useful heavy residual fragment data are of those scattered into the back-hemisphere, but the physics should not be altered by this.

Techniques for the optimized selection of the thicknesses and the gain-settings in the silicon detectors could be improved in future experiments if one is to observe the complete mass region, however one has to deal with the resolution in the mass region of the most interest. The higher gain-settings established in the second silicon elements in the present experiment were necessary for the resolution of the light fragments. One may use two amplifiers per each silicon element with different gain-settings in order to detect the entire mass region without losing significant statistics (for instance, higher gain for lighter fragments and lower gain for heavier fragments).

III.2 Particle Singles Spectra

Particle-identification gates were drawn for each of the nuclei or isotopes in the different 2-dimensional spectra. Particle inclusive kinetic energy spectra for each of those gates were obtained for each particle telescope from the singles runs. Figures III.2.1(a-c) show the typical particle inclusive kinetic energy spectra of light fragments and intermediate fragments at each beam energy, and those for heavier fragments are shown in Figures III.2.2(a-c). The superimposed solid lines drawn in Figures III.2.1(a-c) represent a Maxwell-Boltzmann equation fit in the center-of-mass frame. This will be discussed in the following section along with the slope parameters and the Coulomb corrections. An interesting feature in the particle inclusive kinetic energy spectra shown in the figures is the evolution of the shapes from Maxwellian-like for the very light particles to Gaussian-like for the heavier fragments as predicted by Moretto [Mo75], which supports the theoretical work concerning a continuous transition of the decay mode from the evaporation-dominant mass region to the fission competition region as the fragment gets massive. The dashed lines shown in Figures III.2.2(a-c) represent $v_{CM}\cos\theta_{lab}$, where $\theta_{lab}\approx 11°$ for all of the fragments. The change in the shape of the particle inclusive kinetic energy spectra in Figures III.2.2(a-c) from the intermediate fragments to the heavy residual fragments is quite remarkable. One should notice that the two peaks in the kinetic energy spectra for fragments of Mg, Al, etc. (although many of them show only part of the peak because of the limited energy range) represent the backward-scattering fragments and the forward-scattering fragments in the center-of-mass frame.

Peak velocities for some selected masses at every available angle were taken from the kinetic energy spectra to draw velocity diagrams at each bombarding energy. These are shown in Figures III.2.3(a-c). The calculated Coulomb barriers for ^{7}Be, ^{19}F, and ^{27}Al are drawn (in order of decreasing radius) centered around the head of the center-of-mass velocity vector in order to compare with the peak velocities. For the light evaporation particles, if a Maxwell-Boltzmann distribution of $N \propto Ee^{-E/\kappa T}$ represents the particle inclusive singles spectra in the center-of-mass frame, then the peak velocity (or the most probable velocity) should appear at the energy,

$$E' = E_{\mathrm{Coul}} + \kappa T \,, \qquad \text{(III.1)}$$

where E_{Coul} represents the Coulomb potential energy, and κT is the temperature. On the other hand, the average kinetic energy of fragments is expected to be $E_{\mathrm{Coul}}+2\kappa T$ in the center-of-mass frame. In the calculation of the Coulomb potential energy, a temperature of $\kappa T=3$ MeV and the distance between two nuclei in the binary decay,

$$r = 1.2(A_1^{-1/3}+A_2^{-1/3}) + 2 \ (\mathrm{fm})$$

was assumed. As the shape in the kinetic energy spectra evolves from the Maxwellian-like for the very light evaporation particles to the Gaussian-like for the massive complex fragments, it is expected that the peak energies in the center-of-mass frame will appear at slightly higher values than that given by Eq. III.1, or around at the average kinetic energy ($E_{\mathrm{Coul}}+2\kappa T$). The differences between the peak energies and the calculated Coulomb barriers for the complex fragments in the center-of-mass frame are shown in Figure III.2.4. The dashed lines represent the average peak energies for the data at each beam energy after subtracting the calculated Coulomb energies. About 5 MeV is obtained from the data, and this value is closer to $2\kappa T$ than κT of the Fermi gas model temperature for this nuclear reaction, which is about 3 MeV.

Even though the limited data for the backward-scattering fragments made it difficult to observe the entire scattering shape of the fragments, clear evidence can be observed in Figures III.2.3(a-c) regarding the existence of the Coulomb velocities [Ch87a] in the moving source frame. First of all, the decreasing radius of the peak velocity with the increasing fragment mass (as required by the momentum conservation) and its rough agreement with the calculated Coulomb velocity indicate that the fragments are emitted with a velocity determined mainly by the Coulomb repulsion energy between the two decaying nuclei from composite system. This is strongly supported also by the larger velocity for ^{7}Be than that for ^{7}Li in the center-of-mass frame. In addition, some of the intermediate fragments for which both peaks were observed show that the peaks for the same Z species at every available angle lie roughly on a Coulomb circle centered on the origin of the center-of-mass frame. One should note that the existence of the Coulomb velocities for the complex fragments indicates that those fragments were produced mainly in a binary-decay process from a composite system which may have been formed in either complete-fusion reactions or incomplete-fusion reactions.

Additional information concerning the characteristic of the complex-fragments decay was obtained by determining the median velocity between the backward-scattering peak and the forward-scattering peak. This method may be an advantage of the usage of the kinetic energy spectra since, for many cases, the median velocity can be determined even when only part of the kinetic energy spectrum with a saddle shape was observed as shown in Figures III.2.2(a-c) for some of the intermediate fragments. The Lorentz-invariant differential cross section $\frac{1}{v^2}\frac{\partial^2\sigma}{\partial\Omega\partial v}$ (where v is the laboratory velocity of the fragment) should have a minimum value at the median velocity. Under the

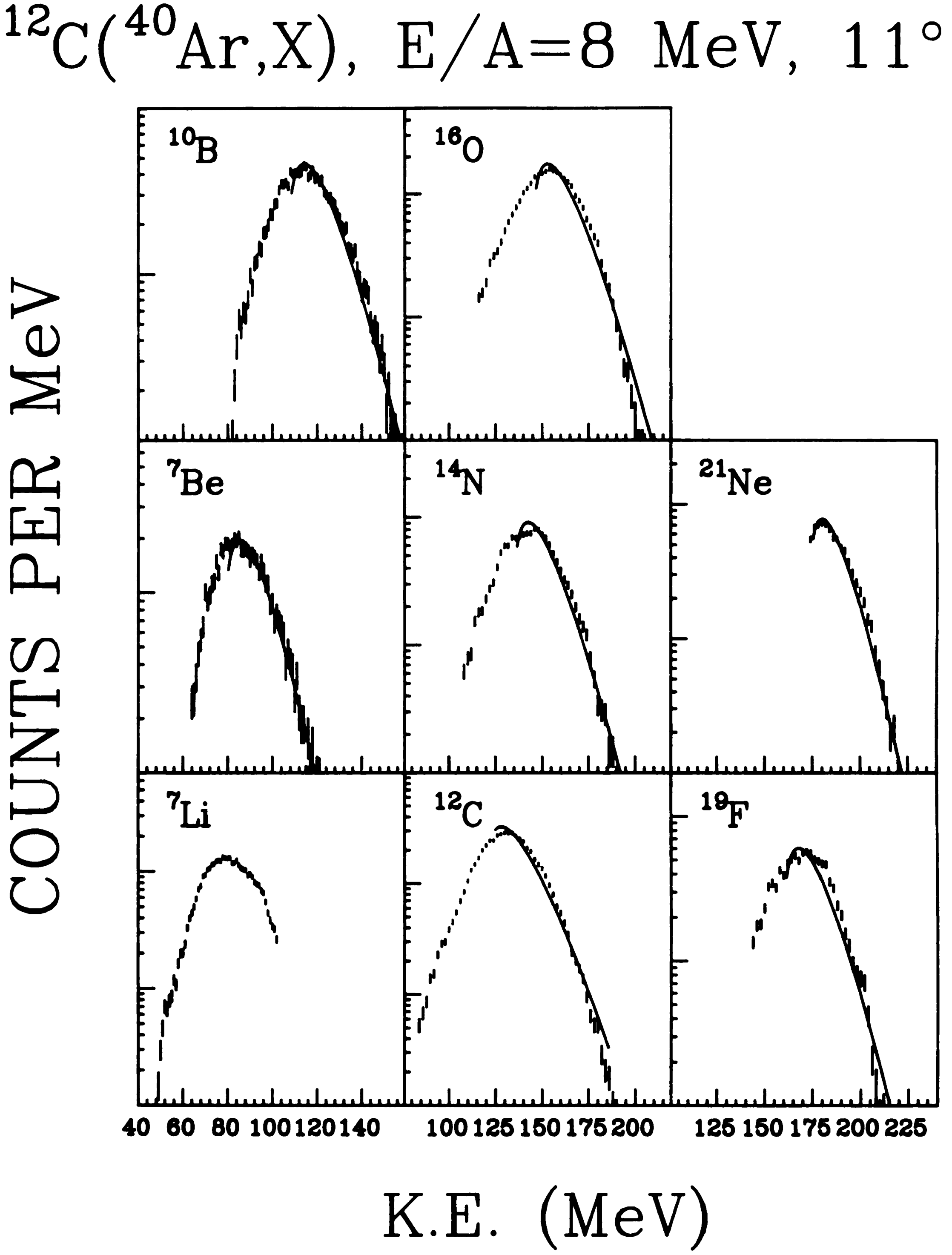

Figure III.2.1 Particle inclusive kinetic energy spectra ($3 \leq Z \leq 11$). a) At E/A=8 MeV.

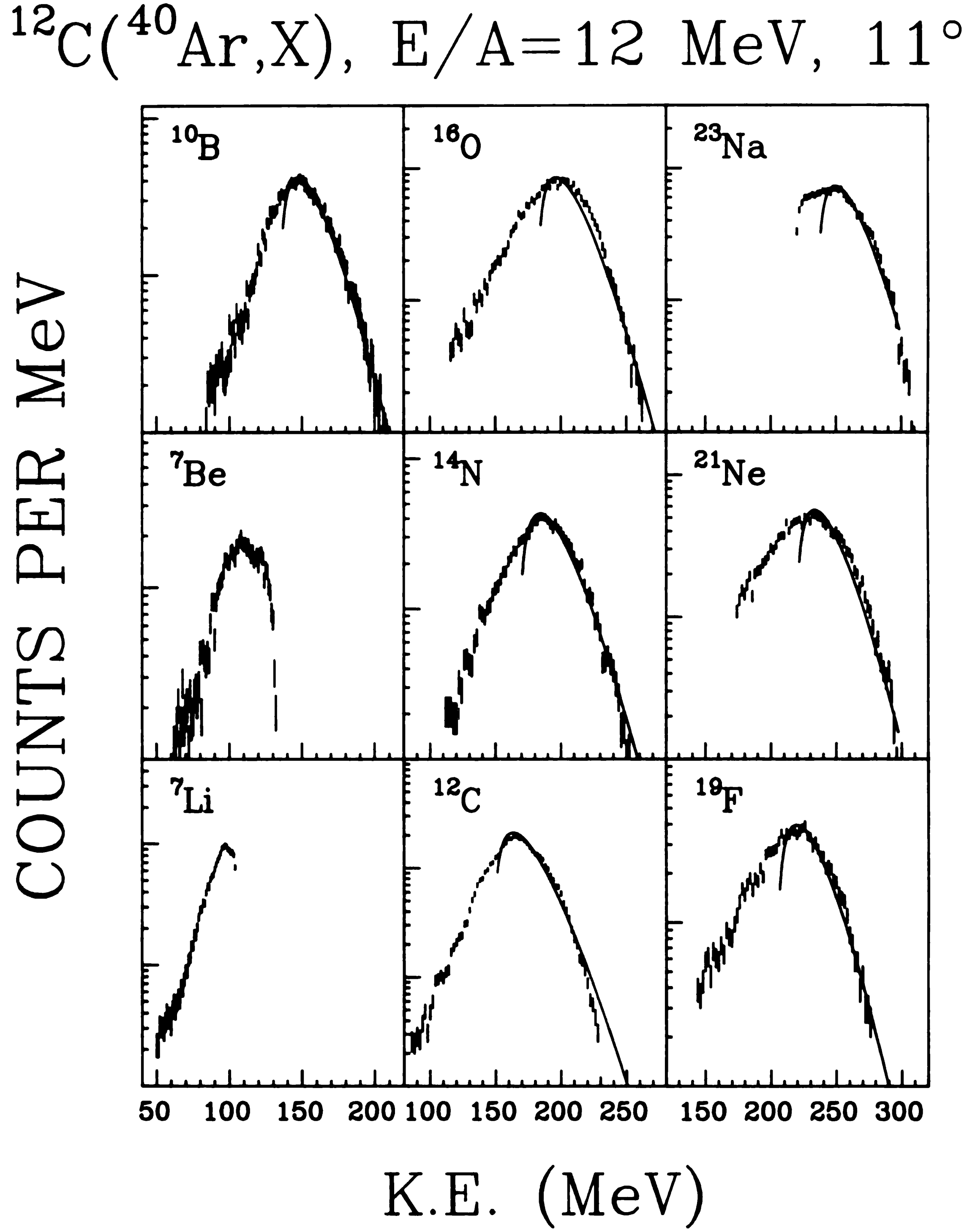

Figure III.2.1 (cont'd.) c) At E/A=12 MeV.

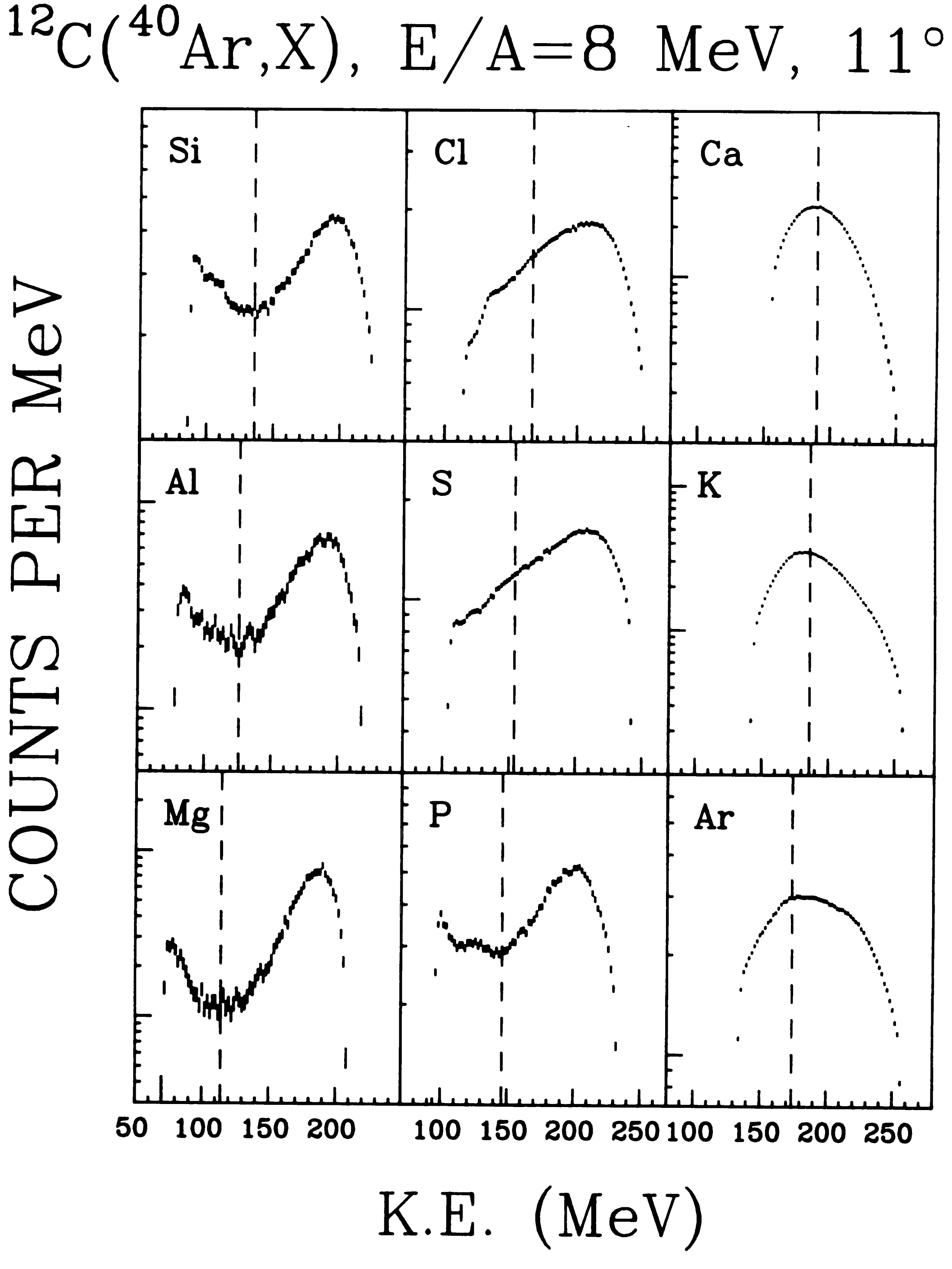

Figure III.2.2 Particle inclusive kinetic energy spectra ($Z \geq 12$). a) At E/A=8 MeV.

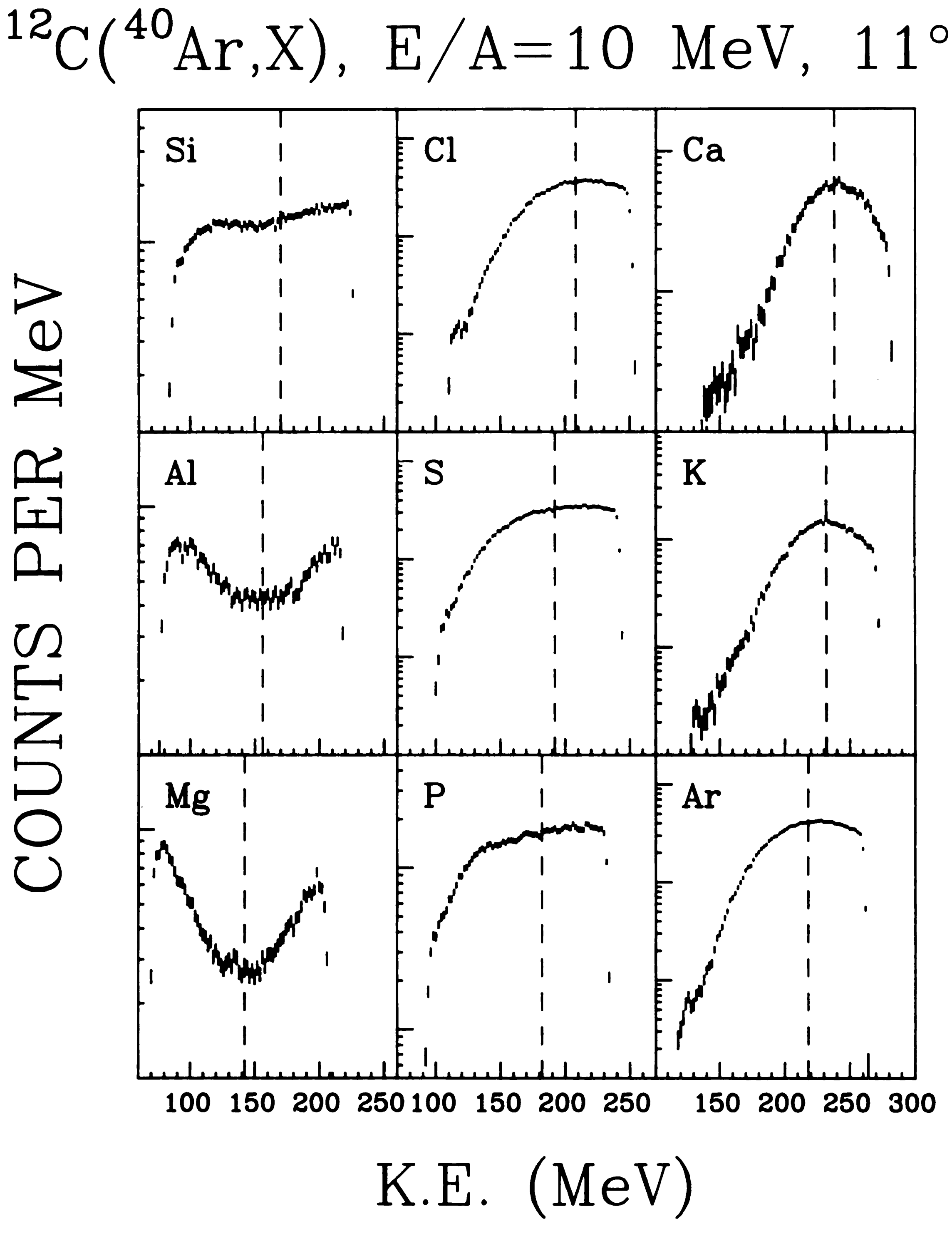

Figure III.2.2 (cont'd.) b) At E/A=10 MeV.

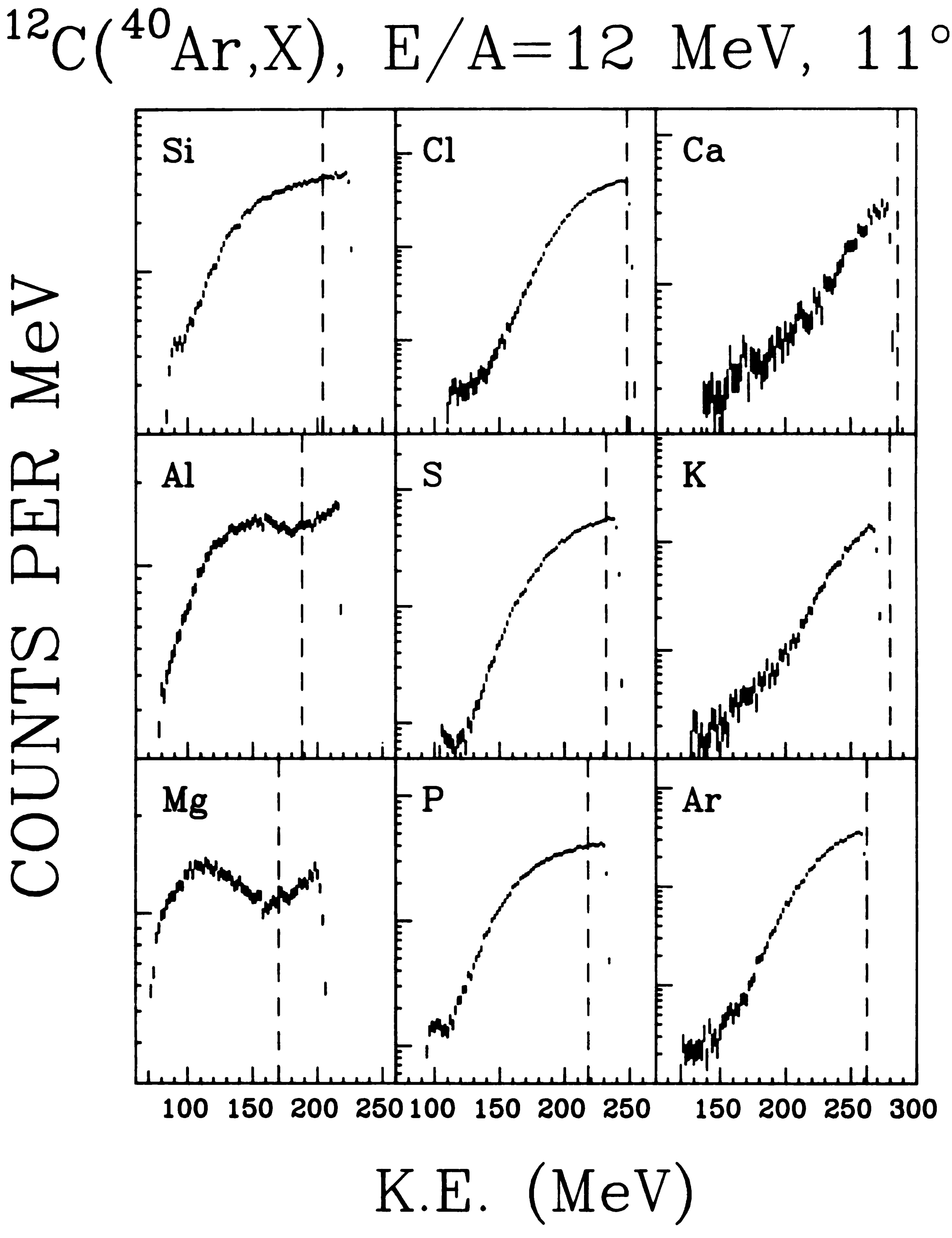

Figure III.2.2 (cont'd.) c) At E/A=12 MeV.

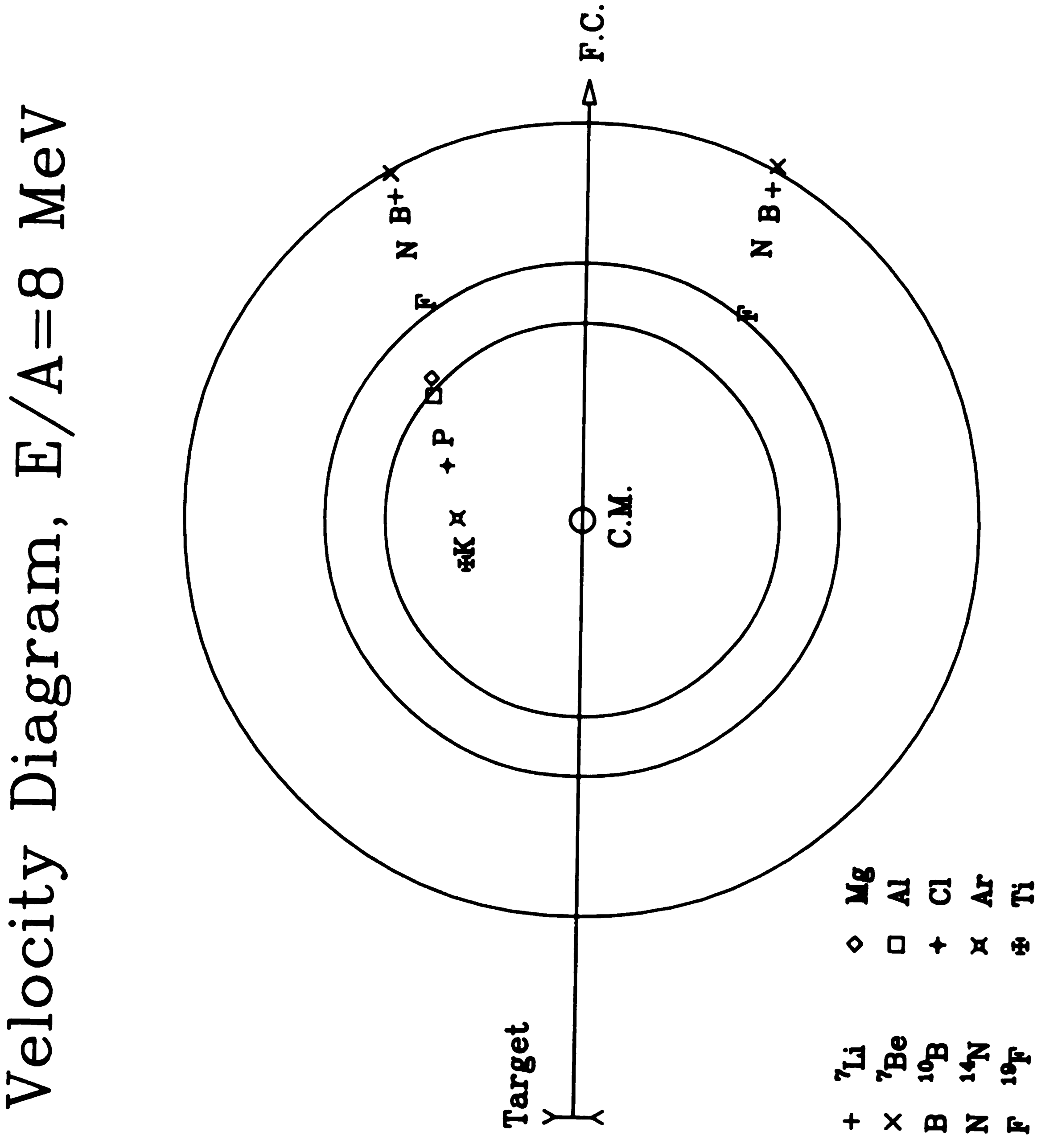

Figure III.2.3 Velocity Diagrams. a) At E/A=8 MeV.

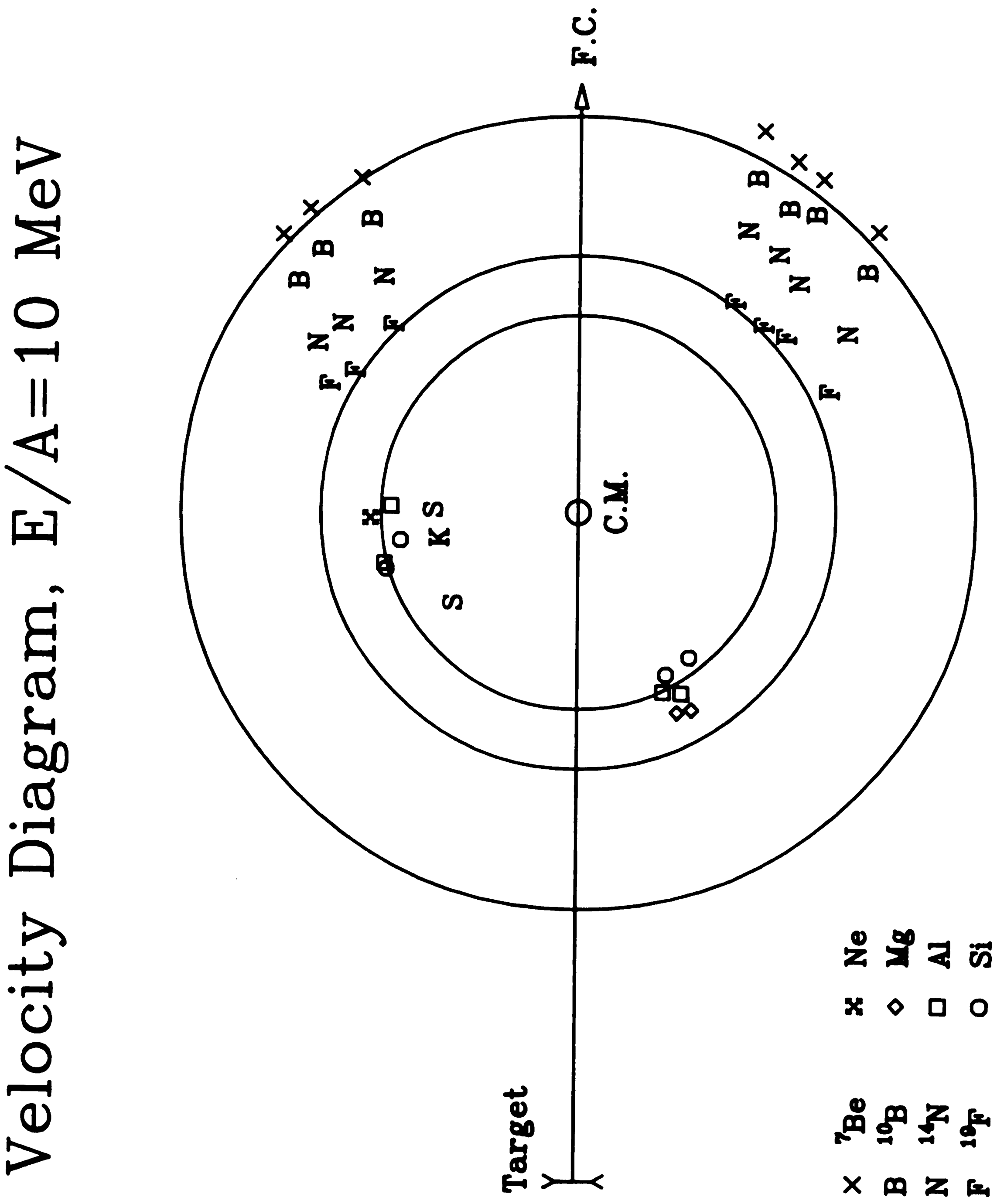

Figure III.2.3 (cont'd.) b) At E/A=10 MeV.

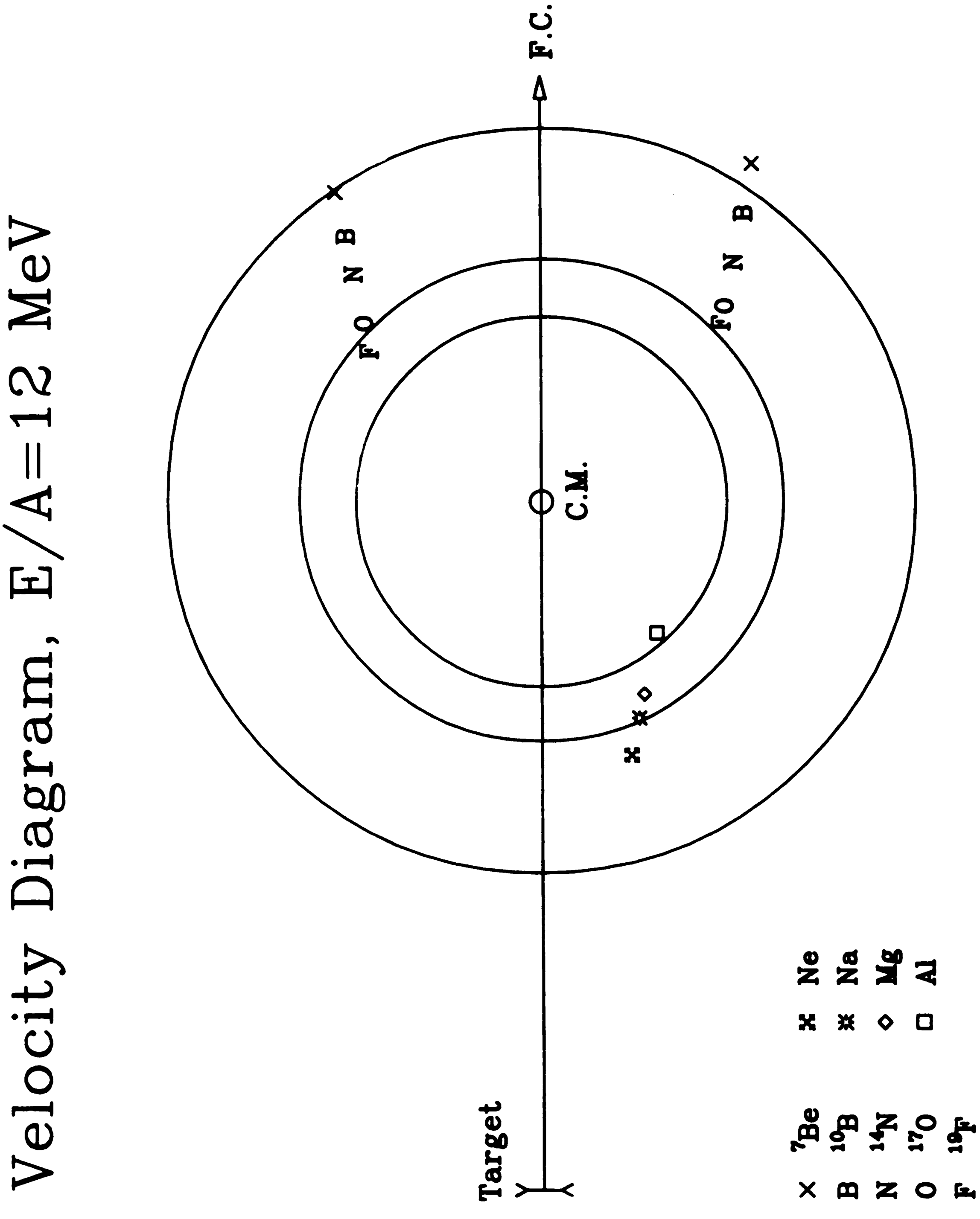

Figure III.2.3 (cont'd.) c) At E/A=12 MeV.

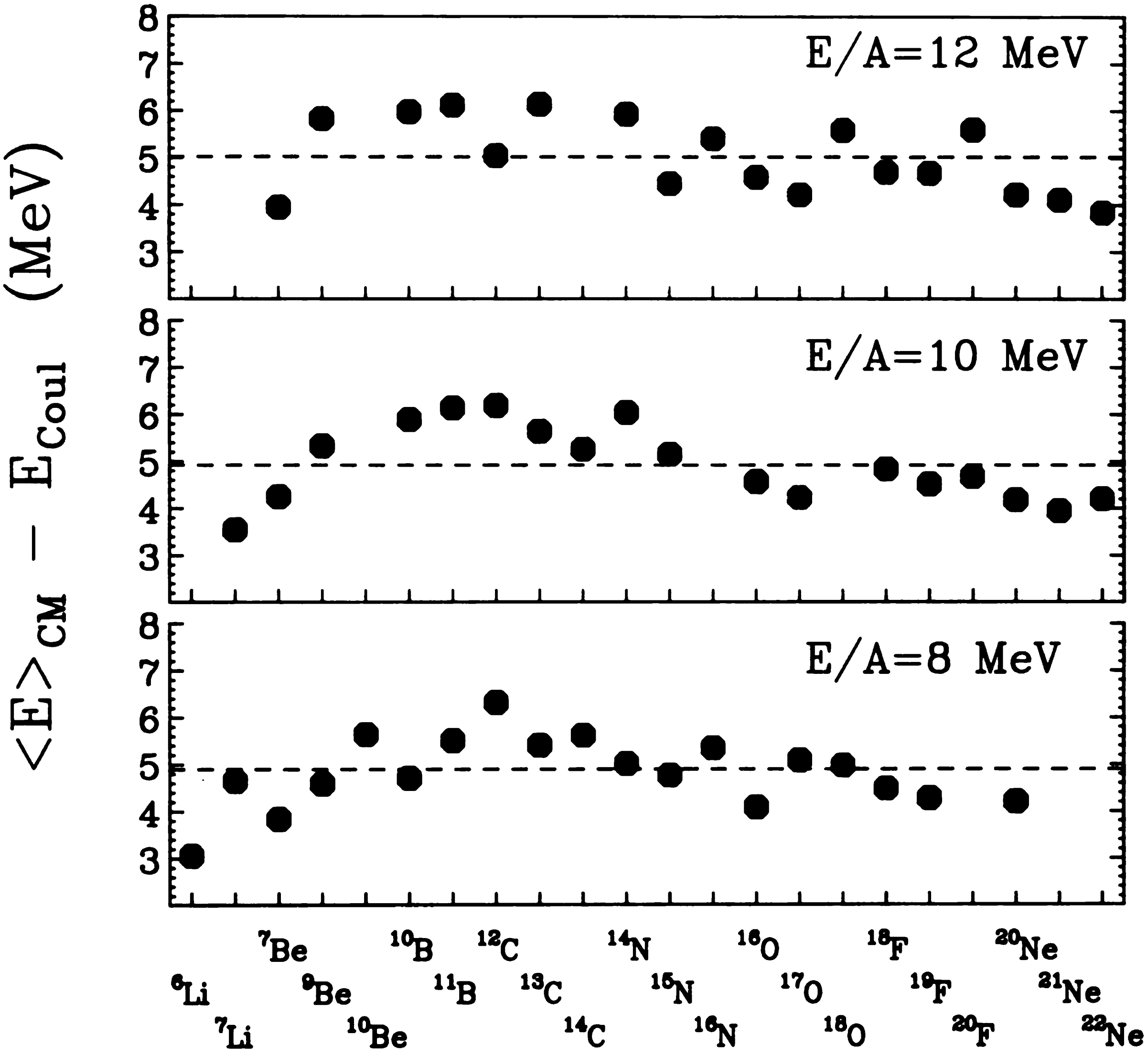

Figure III.2.4 Differences between the peak energies and the calculated Coulomb barriers in the center-of-mass frame.

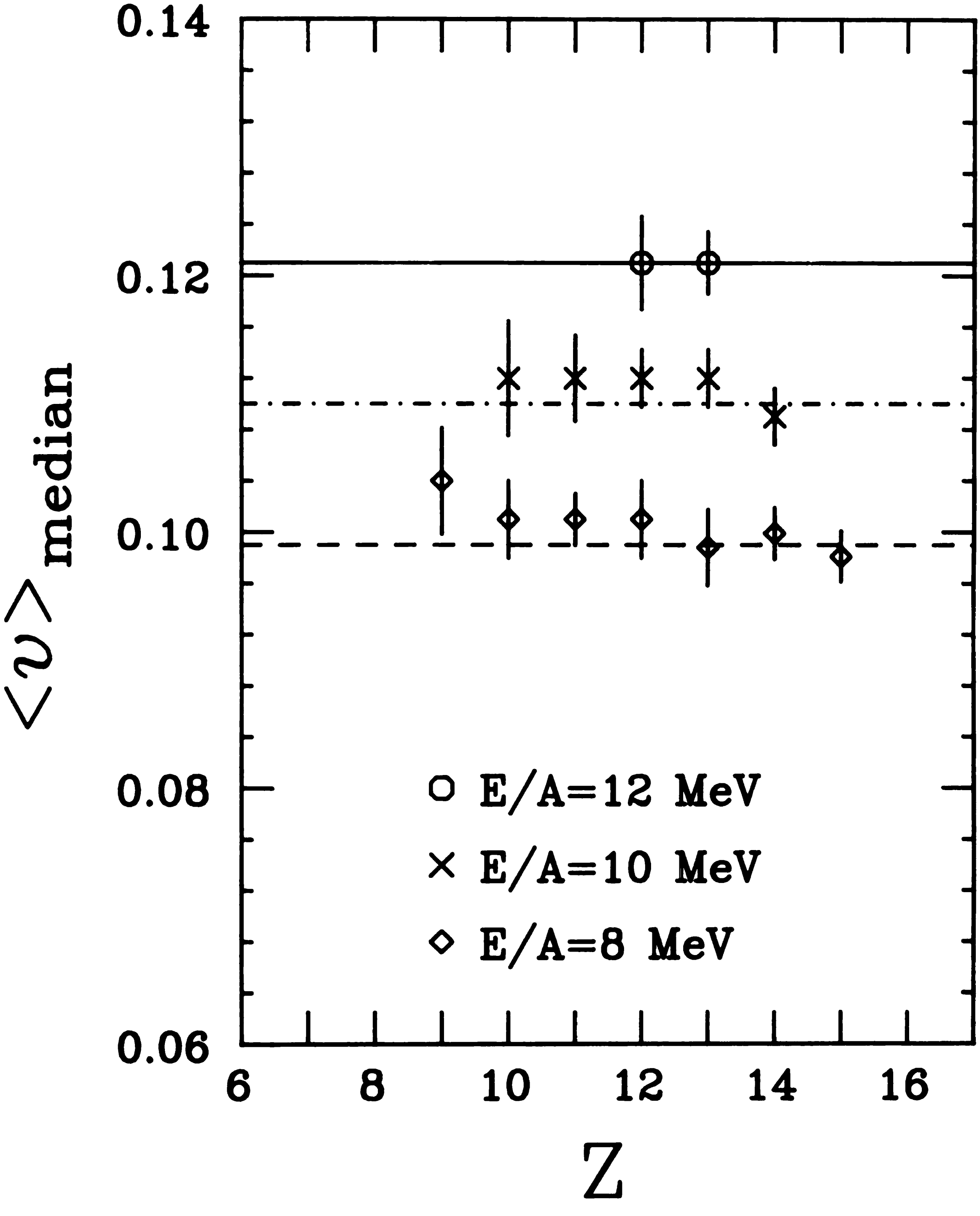

Figure III.2.5 Median velocities of the forward-scattering and the backward-scattering peaks for complex fragments.

assumption of complete fusion the median velocity must be equal to $V_{CM}\cos\theta_{lab}$, and the deviation could come from the incomplete-fusion processes with the preferential break-up of the target or the projectile nucleus [Mo84b]. The determined median velocities for the intermediate fragments are shown in Figure III.2.5 and compared to the velocity $V_{CM}\cos\theta_{lab}$. Masses used for the fragments with only Z-identification ($Z>11$ in the present experiment) were determined from the results of the CASCADE code [Pü77] and the gamma-ray intensities relevant to each nucleus with the same Z (Ch. VI). The possible errors caused in establishing which masses to use were checked by changing the masses by one mass unit in either direction and combined with the experimental uncertainties in all cases. Data at E/A=10 and 12 MeV were limited to only a few of the isotopes, however no major deviation in the median velocities from the predicted velocity $V_{CM}\cos\theta_{lab}$ was observed for the entire range of beam energies, which suggests that the complex fragments with masses intermediate between the target nucleus and the projectile nucleus may be emitted from a moving source which coincides or nearly coincides with the center-of-mass frame.

A reasonable number of simultaneous-multiple events, which means events with more than two telescopes firing at the same time, was recorded during the experiment. Those simultaneous events were mostly between telescope-1 and 4 or between telescope-2 and 3. As described in Ch. II, this combination of telescopes defines two scattering planes which intersect along the beam line, and each telescope lies at polar angle $\theta\approx11°$ with an identical solid angle. Hence fewer simultaneous events between telescopes in the different scattering planes (e.g., between telescope-1 and 3 or between telescope-2 and 4) relative to those between telescopes in the same scattering plane can be taken as evidence of the dominance of the binary-decay process in the exit channel. Note that in a multi-fragmentation event, fragments may not generally decay into the same scattering plane, and this will result in making the chance of simultaneous events between any two telescopes equal except between telescope-1 and 2 and between telescope-3 and 4, the planes of which are obviously too far away from the beam line. A typical example of this is shown in Figure III.2.6 for the case of telescope-2 (Z_2) with telescope-3 (Z_1) with Z_1=7. The solid lines are the events for telescope-2 with telescope-3 and the dotted lines represent those for telescope-2 with telescope-4. No significant number of events for telescope-2 with telescope-1 was obtained as expected. An interesting tendency one can find in Figure III.2.6 is that the number of events for telescope-2 with telescope-4 becomes comparable relative to that with telescope-3 as Z_2 decreases, indicating that the fragments with the smaller value of Z_1+Z_2 than the total charge in the reaction, $Z_1+Z_2=24$, were formed from a composite system which was moving off the beam line. This may be explained in two different directions; (1) incomplete fusion is an important process in the entrance channel, which is supported by the fact that the composite system formed from an incomplete-fusion will not, in general, continue undeviated in the beam direction, and, (2) the composite system is formed from a complete-fusion reaction, and then goes through very light particle emission (such as neutrons, protons, or alpha-particles) before emitting the complex fragments through a binary-decay process.

The Z_1-Z_2 correlation plots of the simultaneous events between two telescopes are shown in Figures III.2.7(a-c) for each beam energy. In the analysis of the simultaneous events, a gate was put on the forward-scattering fragments (Z_1) and it was found that most of the decay partners (Z_2) were observed with low velocities which are in the backward-scattering range, except the case of $Z_1=2$ (although most of the events with $Z<3$ were rejected electronically during the experiment, a large number of events with alpha-particles, which is due to the particle-particle coincidences, was still recorded) wherein the velocities of Z_2 were scattered all over the range. A dramatic change in the velocities of the decay partners at $Z_1=2$ may imply that alpha-particles were formed through many different channels, such as pre-equilibrium evaporation, deep-inelastic scattering, or consecutive statistical emission from a compound nucleus. In Figures III.2.7(a-c) one should note that the data scale is somewhat arbitrary from one Z_1-line to another because the number of forward-scattering Z_1-fragments in the telescope-3 was limited by the energy range as shown in Figures III.1.2 and III.2.1(a-c) especially for $10 \leqq Z \leqq 12$, which reduces the number of events in this intermediate fragment region. Nevertheless, the result shows that most of the events lie in a Z_1+Z_2 band which remains approximately constant with a wider width at E/A=12 MeV and a narrower width at E/A=8 MeV. The average values of Z_1+Z_2 were roughly estimated by considering the data only for $7 \leqq Z_1 \leqq 12$, and those are found to be approximately 23, 22, and 21 at E/A=8 MeV, 10 MeV, and 12 MeV, respectively. In a fission model [Ro84], the excitation energy in the scission configuration (or presumably in the saddle-point configuration) can be written as

$$E_{SD}^{*} = E_{CM} + Q - E_{Coul} - E_{Def} - E_{Rot} ,$$

NUMBER OF EVENTS

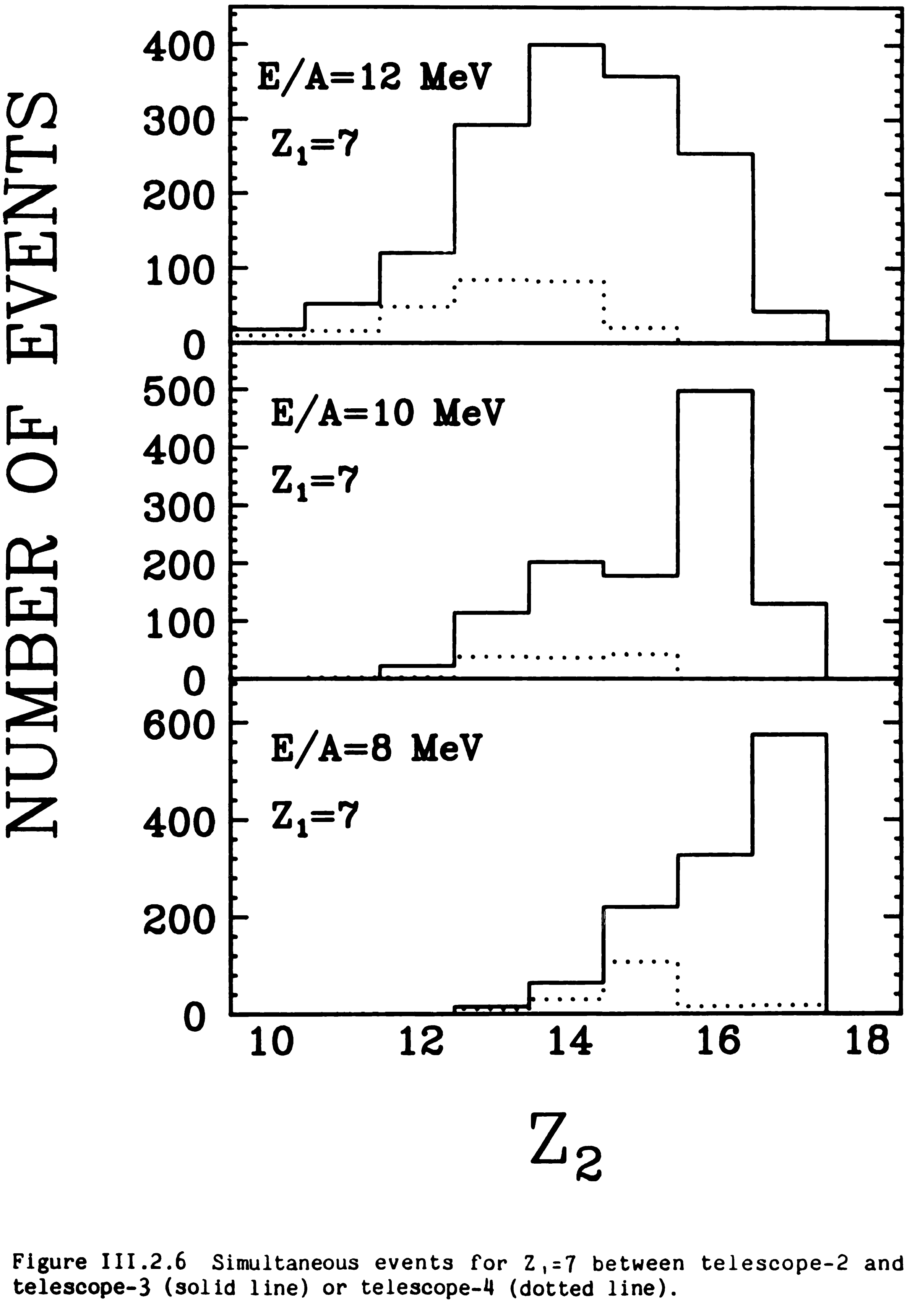

Figure III.2.6 Simultaneous events for Z_1=7 between telescope-2 and telescope-3 (solid line) or telescope-4 (dotted line).

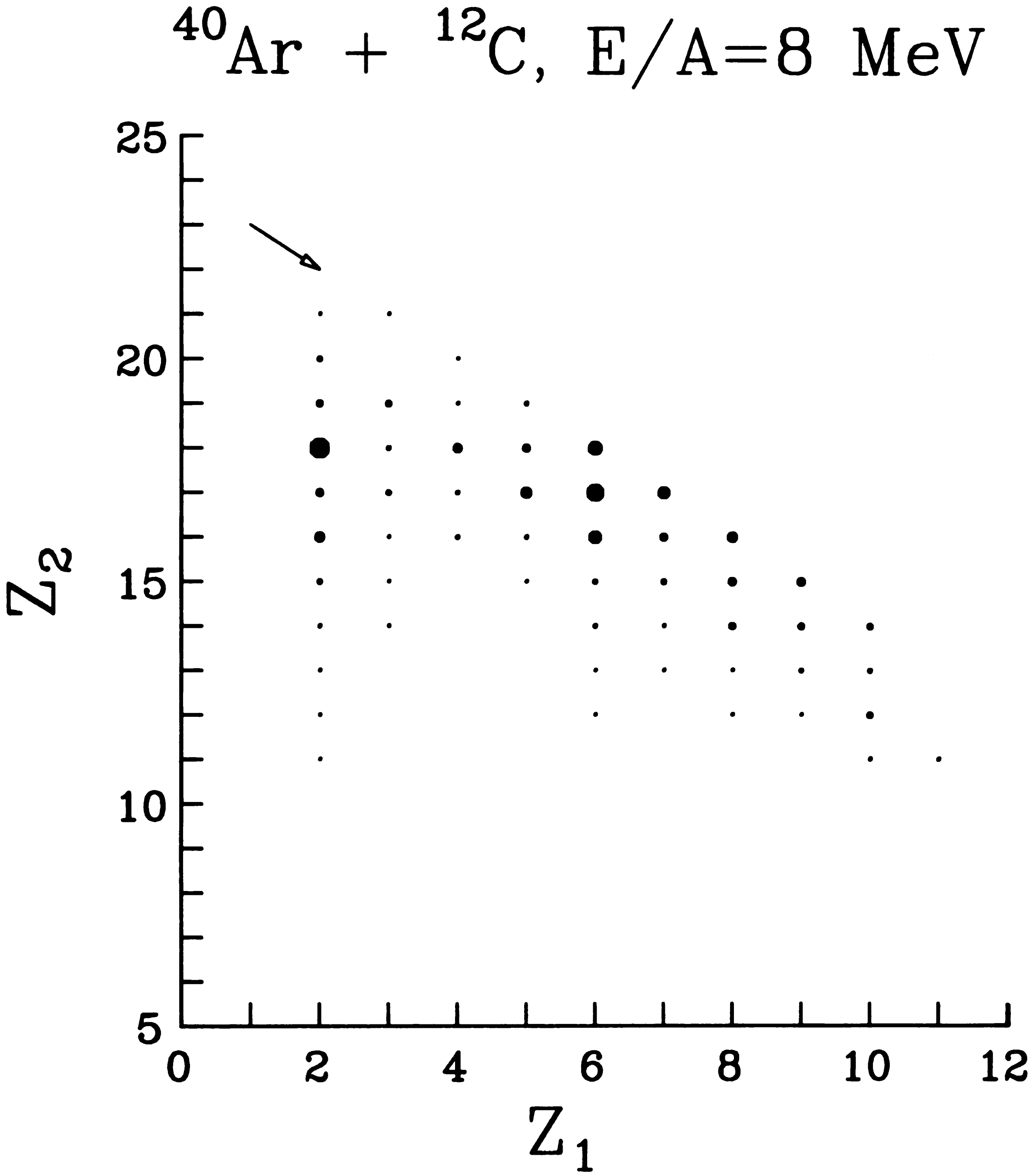

Figure III.2.7 Z_1 - Z_2 correlation plot for simultaneous events between telescope-2 and telescope-3. Arrow drawn indicates the total charge (Z_{tot}) of the system. a) At E/A=8 MeV.

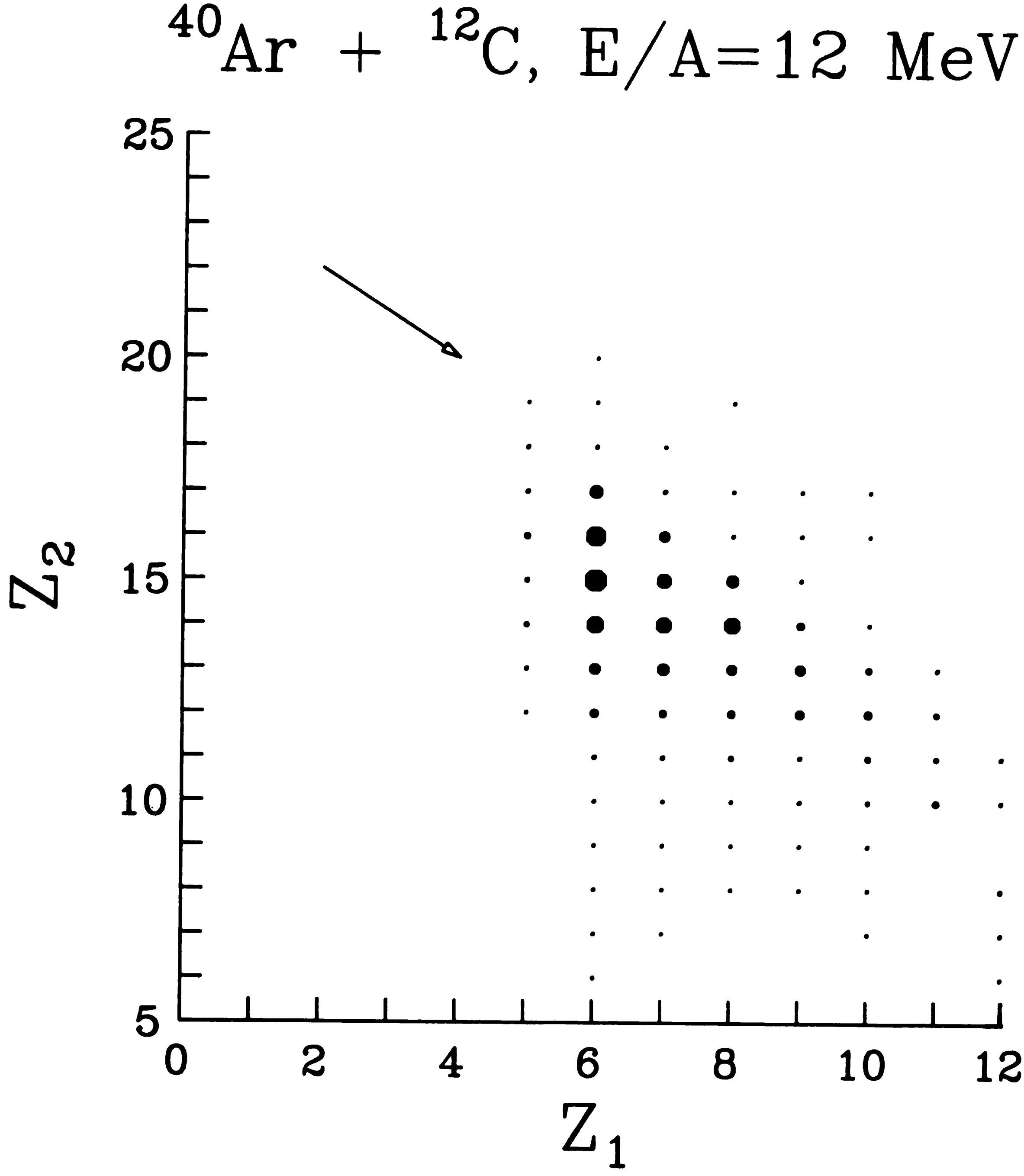

Figure III.2.7 (cont'd.) c) At E/A=12 MeV.

where E_{CM}+Q consists of the excitation energy of the compound nucleus in the full-momentum transfer reaction, and E_{Coul}, E_{Def}, and E_{Rot} represent the Coulomb potential, deformation energy, and rotational energy in the scission configuration, respectively. The typical values of E_{Coul} and $\langle E_{Rot} \rangle$ are 22 and 14 MeV, respectively, for the near-symmetric fissions, and the liquid-drop model predicts the deformation energy to be about 20 MeV [Ro84]. Therefore, the estimated average excitation energies in the scission configuration are about 38, 56, and 74 MeV at E/A=8, 10, and 12 MeV, respectively. If half the excitation energy is taken by each symmetric fission product, the average excitation energy of 19 MeV taken by one fission product at E/A=8 MeV may be large enough to emit a light particle. This would be emission of a nucleon or alpha-particle depending on the excitation energy and the spin of the fission product. The 18 MeV difference in the excitation energies between the neighboring beam energies which were employed in the present experiment may correspond to the elimination of approximately one charge (or about 2 mass-units in this mass region). This prediction is roughly consistent with the data, which implies that the lower average values of Z_1+Z_2 for the higher beam energies does not demonstrate the onset of incomplete fusion.

The events with lighter fragments (smaller Z_1) show a wider range of Z_2 with smaller values of Z_1+Z_2, and the range becomes narrower for heavier fragments (larger Z_1) while the value of Z_1+Z_2 becomes larger. A lot of events with the total charge, Z=24, was observed at E/A=8 MeV, especially for Z_1 close to half of the total charge, however the number of such total charge events decreases dramatically relative to those of less than the total charge at E/A=10 MeV and 12 MeV. Few events with the total charge are observed for $Z_1 < 6$ at any beam energy, and this may be due to either the sequential evaporation decay of more light particles after binary decay from the compound nucleus or the direct binary-decay process after incomplete fusion. The population distribution of nuclear states by measurement of the gamma-ray intensities in coincidence with these complex fragments will be discussed in Chapter IV.

In the case of incomplete-fusion reactions, because the participants from the projectile and the target to form a composite system are, in general, different from those for the complete-fusion reactions, the moving source does not coincide with the center-of-mass frame but deviates from it. This was checked by determining the centroids of the Lorentz-invariant differential cross section $\frac{1}{v^2}\frac{\partial^2\sigma}{\partial\Omega\partial v}$ of the heavy residual fragments and comparing these with the velocity $v_{CM}\cos\theta_{lab}$. Figure III.2.8a shows that at E/A=8 MeV, the centroid velocities for K and Ca are in good agreement with $v_{CM}\cos\theta_{lab}$; however that for Ti is significantly lower than expected while that for Sc remains roughly in agreement. The solid lines represent the predicted velocity ($v_{CM}\cos\theta_{lab}$) and the arrows indicate the centroids of the Lorentz-invariant differential cross sections. A similar result at E/A=10 MeV is shown in Figure III.2.8b. A general tendency one may observe in these two figures is that the centroid velocity decreases as the mass of the fragments increases. This can be considered as a strong indication of the tendency toward projectile break-up in incomplete fusion. A shift in the centroid velocity away from the predicted velocity may be used to estimate the fraction of the complete-fusion cross section to the total reaction cross section [Hi87, Mo84b].

However this becomes less plausible under the circumstance of decreasing centroid velocity with increasing mass in the heavy residual fragments region. The possible errors caused by the use of one less or one more unit of mass could not explain the discrepancy, and this becomes a puzzle if one compares this result with that in Ref. Mo84b. In this reference, Morgenstern et al. showed a preference for the breaking-up the lighter nucleus (target nucleus in this case) rather than the heavier nucleus during the incomplete-fusion process in a dinuclear reaction. This may be supported by an argument in the abrasion model, that the breaking-up of the smaller nucleus, rather than the larger nucleus, involves a smaller surface area in the process of shearing away the occluded volumes [Ch87a]. The centroid velocity of residual fragments with mass A=43 from the reaction ^{40}Ar + ^{12}C at E/A=13 MeV in this reference is higher than the center-of-mass velocity at $\theta_{lab}=6°$, which implies that the incomplete-fusion process is mainly due to the break-up of the target nucleus. Similar but more specific results are presented in Ref. Mo86b. The higher centroid velocities obtained in the the particle inclusive spectra for the heavy residual fragments from the reaction ^{40}Ar + ^{12}C at E/A=7 MeV have been regarded as being due to the massive cluster transfer in the entrance channel. Those heavy residual fragments were detected at $\Theta=2.5°$, and this angle is much smaller than that employed in the present experiment. Nevertheless, disagreement between the data from Refs. Mo84b and Mo86b and the present experiment may not be explained without further information on the cross sections of evaporation residues with a wider mass range at the various angles.

One of the most interesting features one can notice in the Figures from III.I.3a to III.I.3c is the change in the detected yield of heavy

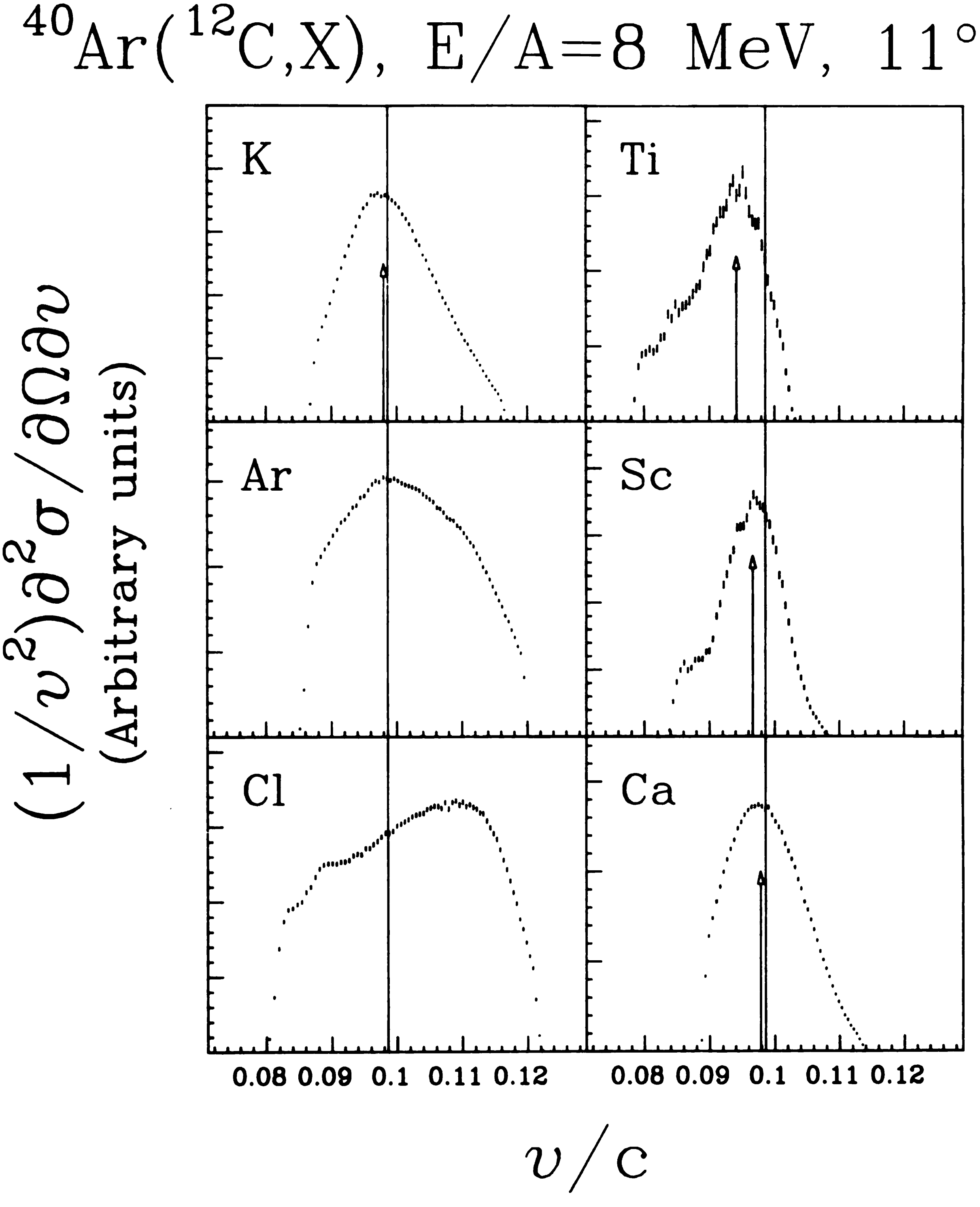

Figure III.2.8 The Lorentz-invariant differential cross sections for heavy residual fragments. a) At E/A=8 MeV.

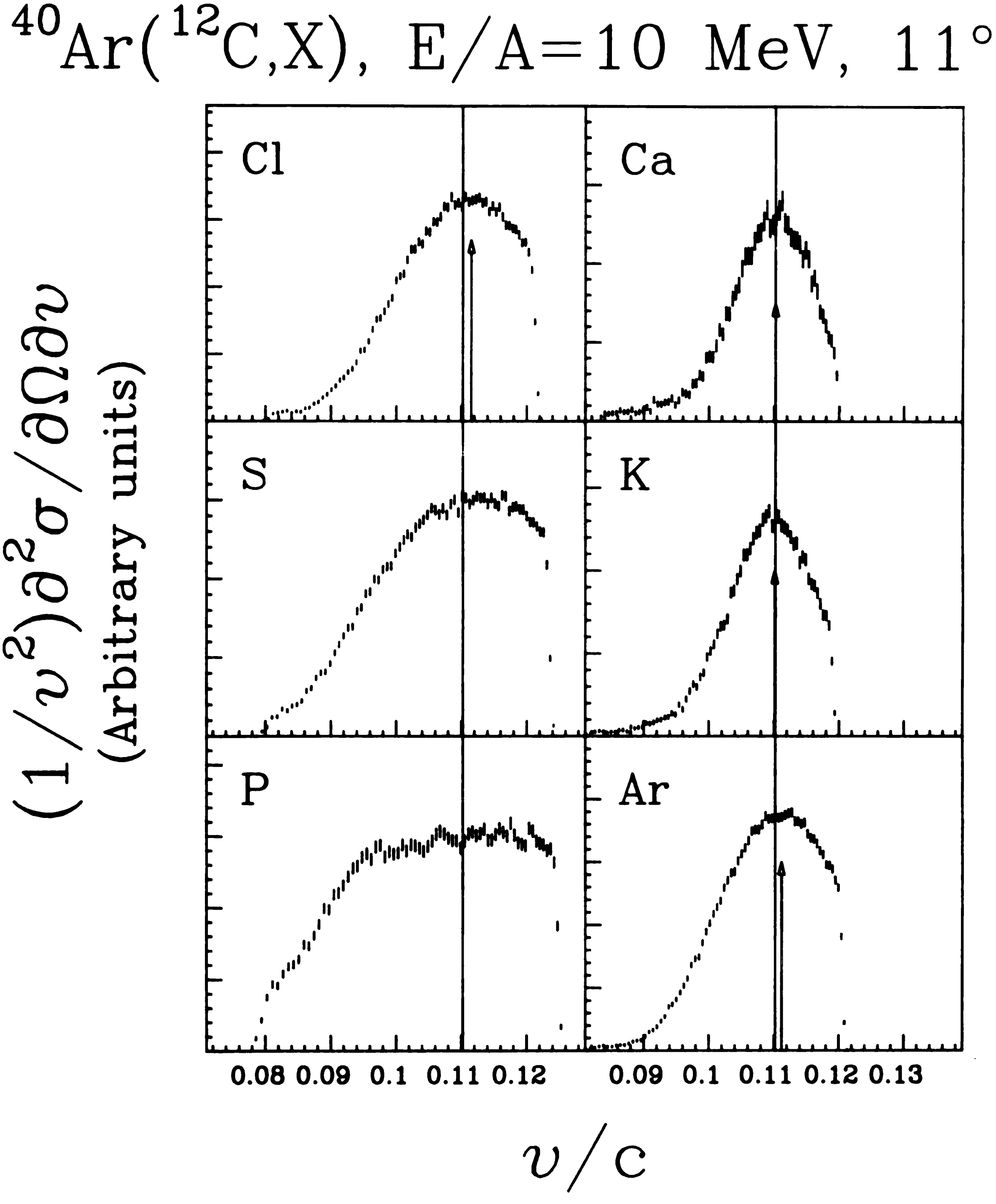

Figure III.2.8 (cont'd.) b) At E/A=10 MeV.

residual fragments close to the compound nucleus (^{52}Cr), such as V, Ti, Sc, etc., which may indicate the increasing role of incomplete fusion with increasing beam energy. Further discussion of this may be obtained by comparing the data with the predicted kinetic energy spectra for the heavy residual fragments by a statistical model, for example, LILITA [Go81]. We omit this discussion in this thesis because of the lack of the full-ranged spectra for the heavy residual fragments.

III.3 Slope Parameters

Moving source fits [We82, Ja83] for the complex fragments were not carried out for the current data because of the limited information about the angular distributions (measurements were carried out at angles only from $\theta_{lab} \approx 10°$ to $\theta_{lab} \approx 17°$). Instead, the results from the velocity diagrams [Figures III.2.3(a-c)] and the median velocities shown in Figure III.2.4 provided information on the relation between the moving source of complex fragments and the center-of-mass frame, i.e., they may coincide with each other, or they are very close to each other at least. Possible contributions in the emission of complex fragments from other sources, such as a target-like moving source or a projectile-like moving source, must be taken into consideration as the beam energy increases far above E/A=12 MeV. The kinetic energy spectra in the center-of-mass frame were fitted by a chi-squared minimization procedure using a Maxwell-Boltzmann function

$$N(E') \propto (E'-C)\, e^{-\frac{(E'-C)}{T}} , \qquad \text{(III.2)}$$

where T is a slope parameter, and the parameter C is a Coulomb barrier correction. In order to fit the spectra with Eq.(III.2), the low kinetic energy part of the spectrum was cut off. This made the effect of the Coulomb barrier penetration on the slope parameter negligible.

A transformation of the double differential cross section from one frame to the other was carried out according to the equation [Jo75],

$$\frac{\partial^2\sigma'(E',\Omega')}{\partial E'\partial\Omega'} = \frac{\partial^2\sigma(E,\Omega)}{\partial E\partial\Omega}\,\frac{\sin\Theta}{\sin\Theta'}\ , \qquad \text{(III.3)}$$

and the angle correlation was calculated classically as

$$\frac{\sin\Theta}{\sin\Theta'} = \zeta = \frac{\beta'}{\beta} = \mathrm{SQRT}\left[1 + \left(\frac{\beta_{CM}}{\beta}\right)^2 - \frac{2\beta_{CM}}{\beta}\cos\Theta\right]\ , \qquad \text{(III.4)}$$

where the primed and unprimed notations represent the center-of-mass and the laboratory frame, respectively. The velocity of the center-of-mass frame, β_{CM}, was given as 0.101c, 0.113c, and 0.124c for E/A=8 MeV, 10 MeV, 12 MeV, respectively. The velocity of the fragment, β, was classically given by

$$\beta = \left[\frac{2E}{931.5\ A}\right]^{1/2}\ , \qquad \text{(III.5)}$$

where E is the kinetic energy of the fragment in the laboratory frame and A is the mass number of the fragment. Under the assumption of an isotropic emission in the center-of-mass frame, the corresponding equation to Eq. III.2 can be obtained for the kinetic energy spectra in the laboratory frame according to the above transformation as

$$N(E) \propto \frac{1}{\zeta}(E\zeta^2 - C)\, e^{-\frac{E\zeta^2 - C}{T}} , \qquad \text{(III.6)}$$

where ζ is the function of the laboratory kinetic energy E as defined in Eq. III.4.

Curves obtained by fitting Eq. III.6 to the data are shown in Figures III.2.1(a-c). The fitting parameters for complex fragments with $3 \leq Z \leq 11$ are shown in Figure III.3.1 and are tabulated in Table III.3.1. In this table, E_{Coul} refers to the calculated Coulomb barrier in the center-of-mass frame, and the values of E_{Coul} are presented to compare with the fitted value C. A notable feature in Figure III.3.1 is the decreasing slope parameter as the mass of the fragments increases. Target-like fragments, which may have been produced via quasi-elastic scattering, inelastic scattering, or direct nuclear reactions in this reverse-kinematics reaction, are generally backward-scattering fragments in the center-of-mass frame, hence implying no significant role of these fragments on the larger slope parameters for the lighter fragments. One can note that this behavior is consistent with the time evolution of the temperature in a hot-equilibrated nuclear system studied by Boal et al. [Bo86]. Boal et al. predicts a rapid change in temperature at the early stage. If most of light particles were emitted at the very early stage of the thermal equilibrium while massive fragments were emitted from the expanded nuclear system at a later stage, then the variation of the slope parameters as a function of mass (i.e., a smaller slope parameter for the lighter complex fragments and vise versa as shown in Figure III.3.1) becomes plausible.

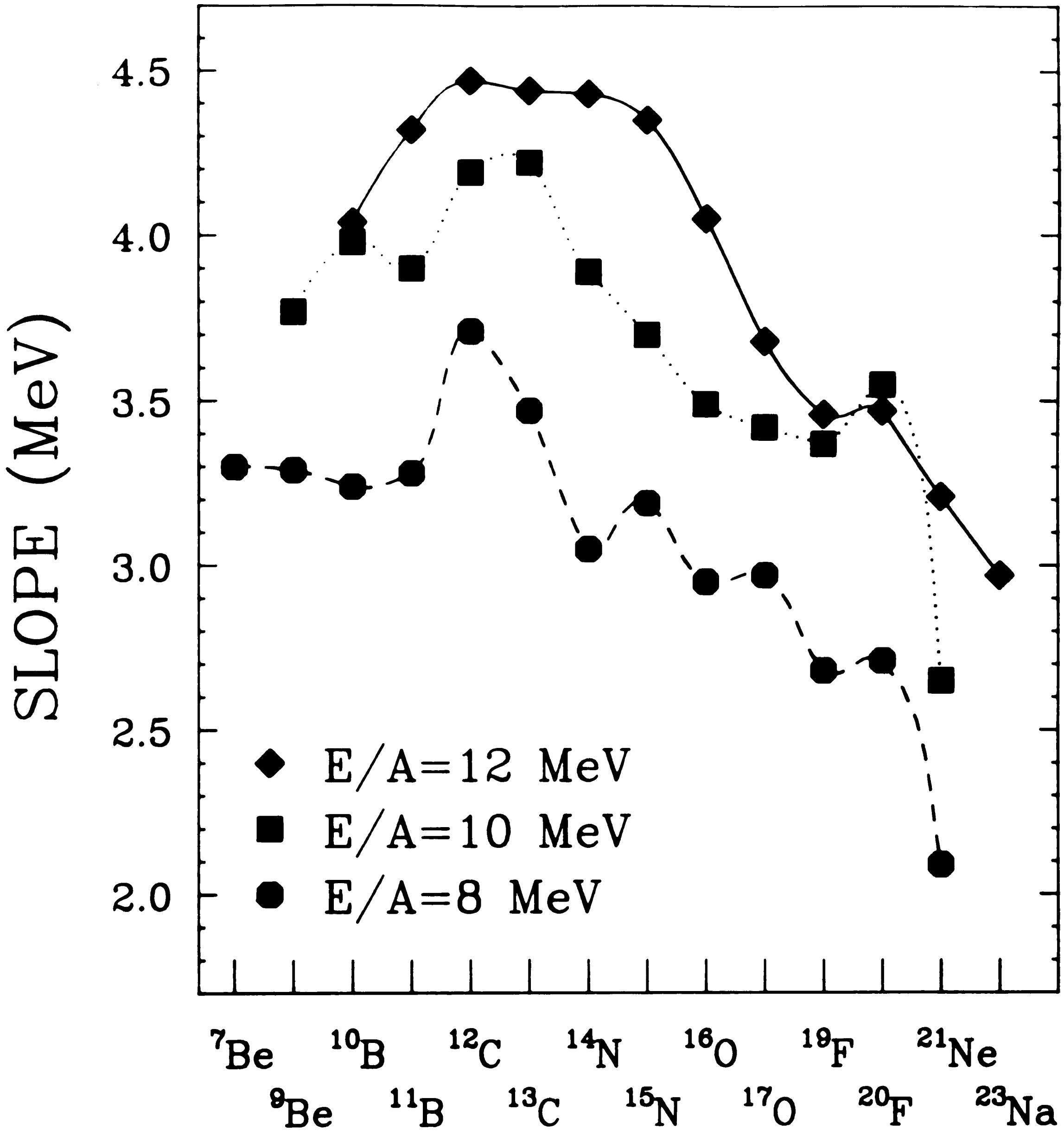

Figure III.3.1 Slope parameters for complex fragments. Lines are drawn for the eye-guide.

Table III.3.1 Kinetic energy spectra fitting parameters for complex fragments.

E/A (MeV)	Isotope	E_{Coul} (MeV)	C (MeV)	Slope (MeV)
8	^{7}Be	11.6	11.5	3.30±0.15
	^{9}Be	10.9	12.2	3.29±0.20
	^{10}Be	10.6	11.5	3.54±0.20
	^{10}B	12.6	14.0	3.24±0.18
	^{11}B	12.2	14.0	3.28±0.16
	^{12}C	13.5	14.1	3.71±0.32
	^{13}C	13.1	13.8	3.47±0.29
	^{14}N	14.0	15.3	3.05±0.10
	^{15}N	13.6	14.3	3.19±0.39
	^{16}O	14.2	14.8	2.95±0.08
	^{17}O	13.8	14.5	2.97±0.15
	^{19}F	13.6	14.3	2.68±0.14
	^{20}F	13.2	13.7	2.71±0.18
	^{21}Ne	13.2	14.9	2.09±0.31
10	^{9}Be	10.9	11.4	3.77±0.47
	^{10}B	12.6	13.3	3.98±0.28
	^{11}B	12.2	13.5	3.90±0.19
	^{12}C	13.5	13.7	4.19±0.37
	^{13}C	13.1	13.4	4.22±0.53
	^{14}N	14.0	14.6	3.89±0.63
	^{15}N	13.6	14.0	3.70±0.57
	^{16}O	14.2	14.1	3.49±0.35
	^{17}O	13.8	14.1	3.42±0.40
	^{19}F	13.6	13.9	3.37±0.50
	^{20}F	13.2	13.4	3.55±0.75
	^{21}Ne	13.2	14.4	2.65±0.39

Table III.3.1 (cont'd.)

E/A (MeV)	Isotope	E_{Coul} (MeV)	C (MeV)	Slope (MeV)
12	^{10}B	12.6	13.5	4.04±0.18
	^{11}B	12.2	13.1	4.32±0.58
	^{12}C	13.5	13.2	4.47±0.41
	^{13}C	13.1	13.2	4.44±0.38
	^{14}N	14.0	14.1	4.43±0.35
	^{15}N	13.6	13.2	4.35±0.52
	^{16}O	14.2	12.9	4.05±0.57
	^{17}O	13.8	14.0	3.68±0.54
	^{19}F	13.6	13.9	3.46±0.93
	^{20}F	13.2	13.2	3.47±0.51
	^{21}Ne	13.2	13.9	3.21±0.45
	^{23}Na	12.6	14.4	2.97±0.48

Table III.4.1 Nuclear temperatures in the Fermi gas model (units in MeV).

E/A	E^*	κT	E_R	E^*-E_R	$\langle\kappa T\rangle^{a)}$
8	94.2	3.44	33.4	60.8	2.76
10	112.7	3.76	36.1	76.6	3.10
12	131.1	4.06	36.1	95.0	3.46

a) Average temperature with rotational energy taken into account.

III.4 Fermi Gas Model

The slope parameters obtained from the Maxwell-Boltzmann function in the center-of-mass frame were compared with the temperatures predicted by the Fermi gas model for this reaction. The relationship between the excitation energy, E*, and the temperature, κT, is given by

$$E^* = a(\kappa T)^2 , \tag{III.7}$$

where a is the level density parameter. The level density parameter has been defined by Tōke et al. [Tō81] as

$$a = \frac{A}{14.61}\left(1+3.114A^{-1/3}F_2+5.626A^{-2/3}F_3+\ldots\right)\ (\mathrm{MeV}^{-1}) , \tag{III.8}$$

where A is the mass number of the compound nucleus and the quantities F_2 and F_3 are set to be unity under the assumption of a spherical shape. The calculated value of the level density for ^{52}Cr from Eq. (III.8) was 6.53 (MeV^{-1}).

The average thermal excitation energy of the equilibrated compound nucleus with an average angular momentum, $\langle \ell \rangle$, is given in Ref. Mo86a as

$$\langle E_{th} \rangle = E^* - \langle E_R \rangle , \tag{III.9}$$

hence the average nuclear temperature becomes

$$\langle \kappa T \rangle = \left(\langle E_{th} \rangle / a \right)^{1/2}, \tag{III.10}$$

where $\langle E_R \rangle$ is the average rotational energy of the rotating compound nucleus. The calculated average rotational energies and the average nuclear temperatures are given in Table III.4.1. The predicted temperatures here are comparable to the slope parameters given in Table III.3.1, and these will be discussed further in Ch. IV in comparison with temperatures obtained from the population distribution of nuclear states.

In order to calculate the average rotational energy in Eq. III.9, the average angular momentum for the compound nucleus was calculated from the predicted critical angular momentum by means of the sharp cutoff approximation. In this approximation, a partial-wave cross section with an angular momentum ℓ is given by $\sigma_\ell \propto (2\ell+1)$. The maximum angular momentum of the compound nucleus was calculated by assuming a maximum impact parameter of $1.2(A_1^{1/3} + A_2^{1/3})$. The result for ^{52}Cr shows that ℓ_{max}=39, 44, and 49$\hbar$ at E/A=8, 10, and 12 MeV, respectively. On the other hand, a critical angular momentum for the same nucleus, at which the shape loses stability against the tri-axial deformation mode, is predicted to be ℓ_I=32 $\hbar$ [Si86, Co74]. Another critical angular momentum, at which the system loses stability to fission and beyond which no equilibrium shape exists, is predicted to be ℓ_{II}=43 $\hbar$ [Si86]. In Ref. Si86, inclusion of finite-range effects in the nuclear surface energy lowers the predicted ℓ_{II} for the light systems as compared to the rotating liquid-drop model predictions [Co74]. A value of ℓ_{II}=52 $\hbar$ is predicted for ^{52}Cr in the rotating liquid-drop model [Co74]. In this thesis, ℓ_{cr}=43 $\hbar$ is adopted [Pü77] as the critical angular momentum for complete fusion to form ^{52}Cr, and the maximum angular momenta calculated in Table III.4.1 are limited by this value.

Fusion reactions have been predicted to occur at distances well outside the point of contact between two colliding nuclei [Ba74, Wi73], where the nuclear densities in the overlap region add up to saturation density of nuclear matter. This implies that the critical angular momentum for complete fusion of ^{52}Cr may be larger than 43 ħ. Also, the use of a distance parameter of $r=1.2(A_1^{1/3}+A_2^{1/3})+2$ (fm) increases the maximum angular momentum far above the adopted critical angular momentum, 43 ħ. On the other hand, some authors [Mo86b, Wi80] suggested that the critical angular momentum for complete fusion to form ^{52}Cr be as low as 32 ħ. From any point of view, the underlying physics is that the onset of incomplete fusion, therefore, may occur at beam energies much below E/A=8 MeV. Incomplete fusion will compete more strongly with complete fusion in peripheral collisions than central collisions. One should note that the maximum angular momentum of the compound nucleus calculated with the sharp cut-off radii of the nuclei is somewhat artificial. Also which maximum angular momentum to use in the calculation of the corrected Fermi gas model temperatures is not very significant as the rotational energy in the heavier system changes little with the increasing or decreasing maximum angular momentum.

CHAPTER IV: POPULATION DISTRIBUTION I
(COMPLEX FRAGMENTS)

IV.1 Introduction

The primary population of a nuclear state in thermal equilibrium should depend only on the temperature of the system, the excitation energy of the state, and the spin of the state. The ratio R of the primary populations of two states in thermal equilibrium is written as

$$R = \frac{(2j_2+1)}{(2j_1+1)} e^{-\frac{(E_2-E_1)}{\kappa T}} , \qquad (IV.1)$$

where j_i and E_i represent the spin and excitation energy of the state i, respectively, and kT is the nuclear temperature. The fraction of the total population f_n in a given state can be deduced from Eq. (IV.1) as

$$f_n = \frac{(2j_n+1)\ e^{-E_n/\kappa T}}{\sum\limits_i (2j_i+1)\ e^{-E_i/\kappa T}} , \qquad (IV.2)$$

where the denominator is a partition function, and the summation over i includes all the states of the nuclear system.

In general, the half-lives of the gamma-ray emitting excited states are so short that the nucleus is in its ground state when it reaches a particle detector. The population of the excited states can be measured with a new technique employed by Morrissey et al. [Mo84a, Mo85a, Mo86a]. In this new temperature measurement, the relative populations of excited states were measured by observing gamma-ray intensities in coincidence with light fragments, such as ^{6}Li, ^{7}Li, ^{8}Li, ^{7}Be, and ^{10}B. The gamma-ray detectors measure the excited state populations which include the feedings from the higher-lying states, while the particle telescopes detect both the ground and excited states of nuclei. A gamma-fraction, the fraction of the fragments that emit a specific gamma-ray by a transition from one state to the other in a nuclear system, can be determined experimentally in a particle-gamma coincidence run as

$$F_\gamma = \frac{N_\gamma}{\varepsilon_\gamma\, N_P} \frac{\text{BIC.LIVE(singles)}}{\text{BIC.LIVE(coincidences)}} , \qquad \text{(IV.3)}$$

where N_γ is the total number of counts in a specific gamma-ray, ε_γ is the efficiency of the gamma-ray detector, N_P is the number of inclusive fragments detected during the particle-singles runs, and the term "BIC.LIVE" refers the integrated beam current during the measurement runs.

In the limit that feeding from particle unstable states in higher-A nuclei is unimportant, then the fraction of nuclei that emit the specific gamma-rays by a transition from a state m to another state ℓ can be formulated as

$$F_{m,\ell} = \alpha_{m,\ell} \frac{[(2j_m+1)e^{-E_m/\kappa T} + M_m]}{\sum_i (2j_i+1)e^{-E_i/\kappa T}} , \qquad (IV.4)$$

and the feeding from the higher-lying states to the state m, M_m, in the same nucleus is defined by

$$M_m = \sum_{q=m+1}^{\infty} \alpha_{q,m}[(2j_q+1)e^{-E_q/\kappa T} + M_q] , \qquad (IV.5)$$

where $\alpha_{i,j}$ is the branching ratio of the gamma-ray transition from the state i to the state j, and the feeding M_q must be repeated up to the highest lying state that decays through gamma-ray emission. The effects of feedings by sequential decay of higher-A nuclei is discussed later. Eq. IV.4 may contain somewhat large uncertainties if the information regarding energy and spin of the levels and the gamma-branching ratios is incomplete or ambiguous. Nevertheless, by simply equating Eqs. IV.4 to IV.3 one can determine the temperature κT, which is the only unknown parameter in those two equations. In the simplest case of a nucleus which has only one bound excited state, for example, ^{7}Li and ^{7}Be, Eq. IV.4 can be simplified as

$$F_{1,0} = \frac{(2j_1+1)e^{-E_1/\kappa T}}{[(2j_0+1) + (2j_1+1)e^{-E_1/\kappa T}]} \qquad (IV.6)$$

where j_0 and j_1 are the spin of the ground and the excited state, and E_1 is the energy of the only bound excited state.

IV.2 Data Analysis

The essential key to this measurement is a clear identification of the individual nucleus in the complex fragment region. Doppler shift corrected histograms of gamma-ray energy spectra were generated for each particle-gamma coincidence combination. The Doppler shift corrections are in the range of 3 ~ 13%, depending on which pair of particle telescopes and gamma-ray detectors was chosen. The estimated geometrical error due to the finite solid angle of the Ge counter, which is based on the average kinetic energy $\langle v \rangle = 0.19$ c of the light fragments, was roughly 2.4 ~ 4.2%, depending on the angle between the Ge counter and the particle telescope. Since this value is much larger than the resolution of the Ge counter, the gamma-ray energy spectra of the NaI(Tl) scintillation detectors were much more useful for light fragments and intermediate fragments (the geometrical shape of the NaI(Tl) detector was not an important factor due to the large distance from the target and its large resolution). A random coincidence histogram of the gamma-rays was subtracted from a real coincidence histogram of the gamma-rays for the same combination of the particle telescope and the gamma-ray detector, however the gamma-ray count in the random coincidence histogram is very small as compared to that in the real coincidence histogram (typically less than 5%), as mentioned in Ch. II. To improve statistics in obtaining the number of counts of the specified gamma-rays for further calculations, all the histograms from the NaI(Tl) detectors were summed together after having been corrected for random coincidences.

IV.3 Light Fragments

Doppler shift corrected gamma-ray energy spectra in coincidence with light fragments are shown in Figures IV.3.1(a-c) for the respective beam energies. The peaks of E_γ=478 KeV for ^{7}Li, E_γ=429 KeV for ^{7}Be, and E_γ=718 KeV for ^{10}B are clearly seen at all the beam energies. The 414 KeV and 1022 KeV gamma-rays from ^{10}B are relatively weak gamma-lines, and are not clearly observed in the present experiment. No prominent gamma-ray peaks for ^{6}Li, ^{9}Be, and ^{11}B were observed in the present detection range as expected from the level structure [Aj84, Aj85]. The 511 KeV positron annihilation gamma-rays were widely spread after the Doppler shift corrections and were negligible quantitatively in most cases. The majority of the coincidence gamma-rays observed in the present experiment consisted of continuum gamma-rays with an exponential tail at the high energy region. This was interpreted as being due to one broadly defined moving source of the continuum gamma-rays, and the underlying statistical transitions are extended over the entire range of the data.

The gamma-ray peaks under consideration were fitted with a Gaussian function to obtain the number of counts in each peak. The gamma-fractions determined by Eq. IV.3 are compared with those calculated with Eq. IV.4 with temperatures predicted by the Fermi gas model, and the results are shown in Figures IV.3.2(a-c) for ^{7}Li, ^{7}Be, ^{10}B, respectively. The solid curves drawn in Figures IV.3.2(a-c) represent the gamma-fractions predicted by the Fermi gas model. The decay schemes of the particle bound states for each nucleus are drawn in these figures. As discussed in Sec. II.4, the contamination of the ^{7}Li

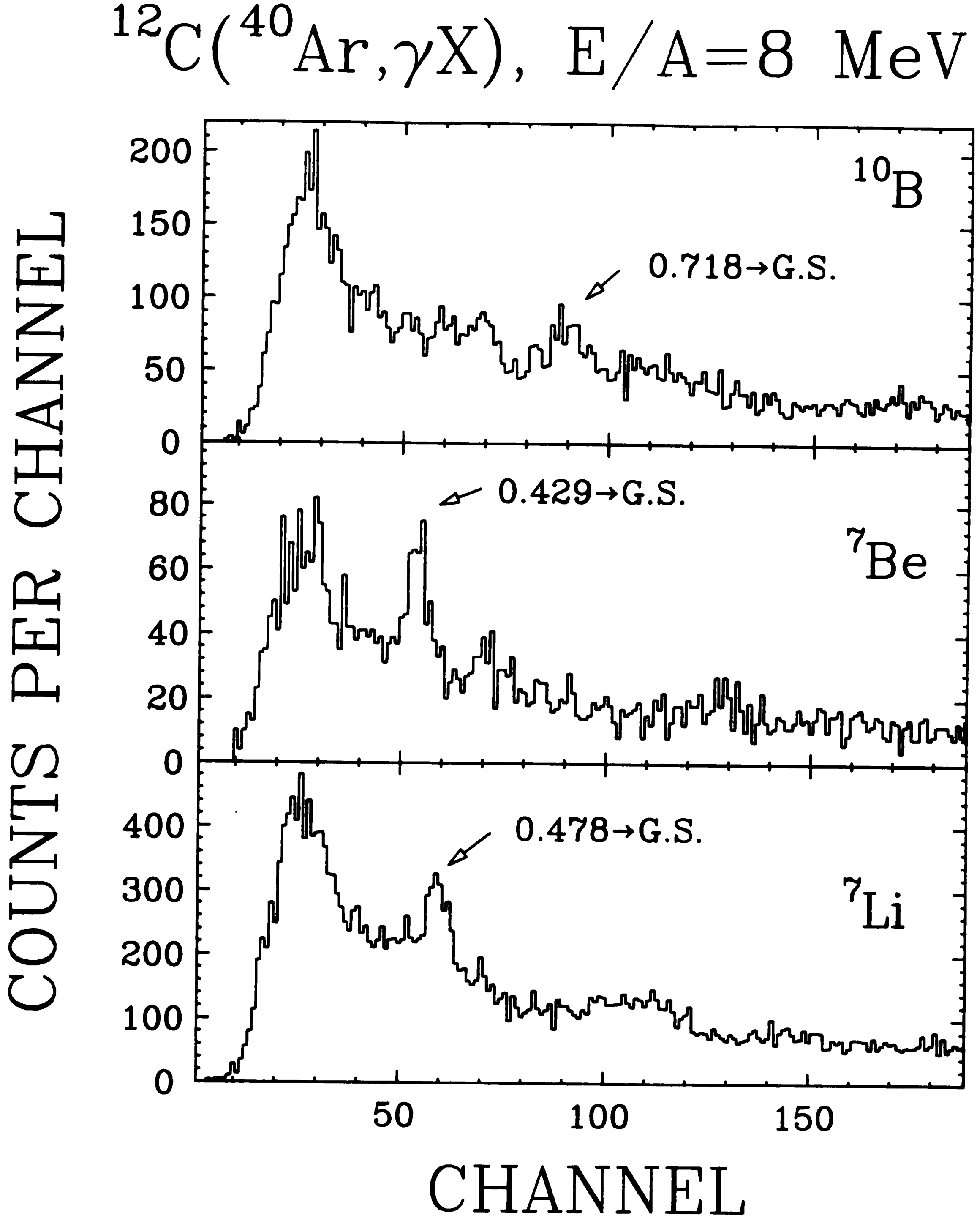

Figure IV.3.1 Doppler-shift corrected γ-ray energy spectra (NaI) in coincidence with light fragments. a) At E/A=8 MeV.

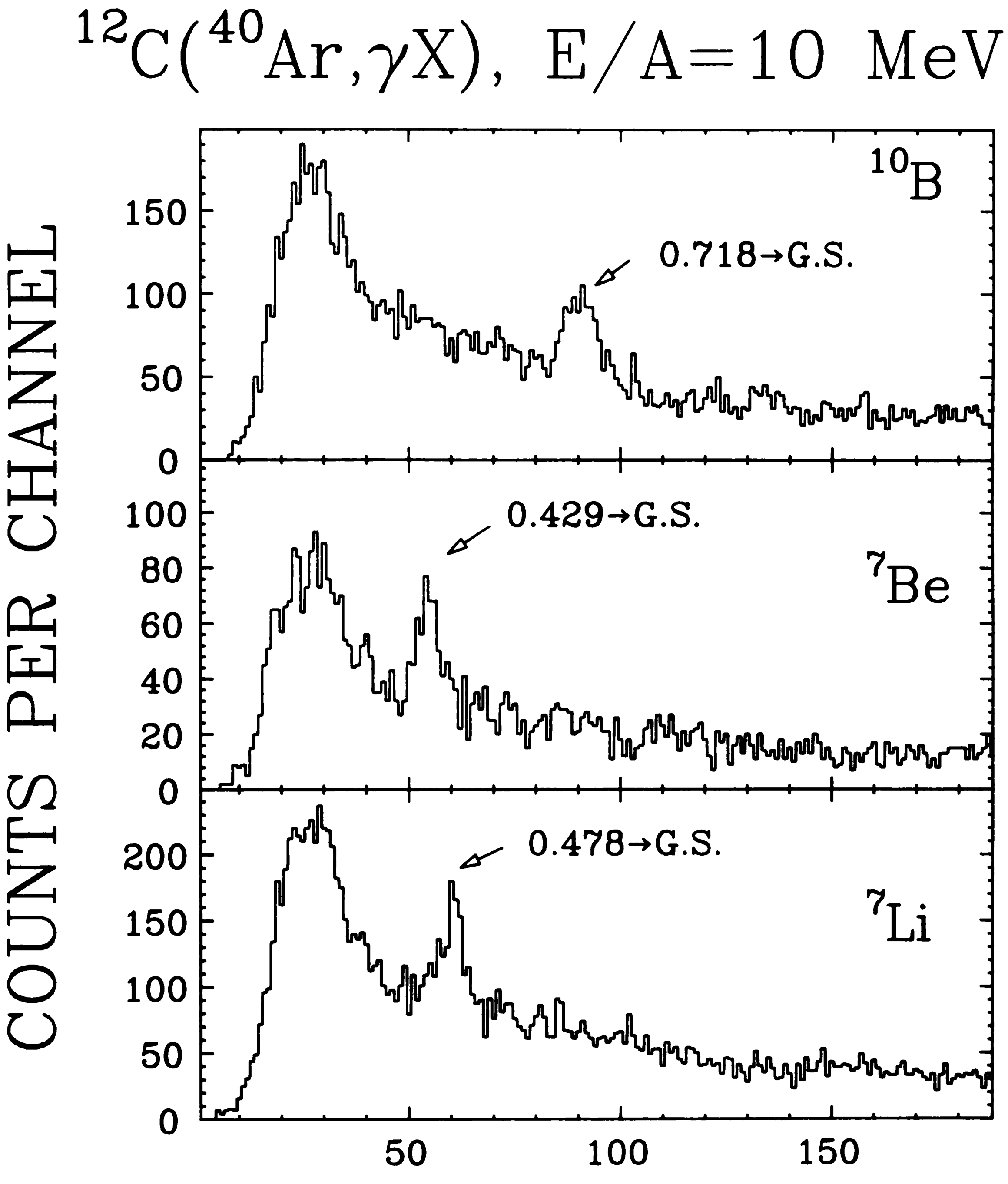

Figure IV.3.1 (cont'd.) b) At E/A=10 MeV.

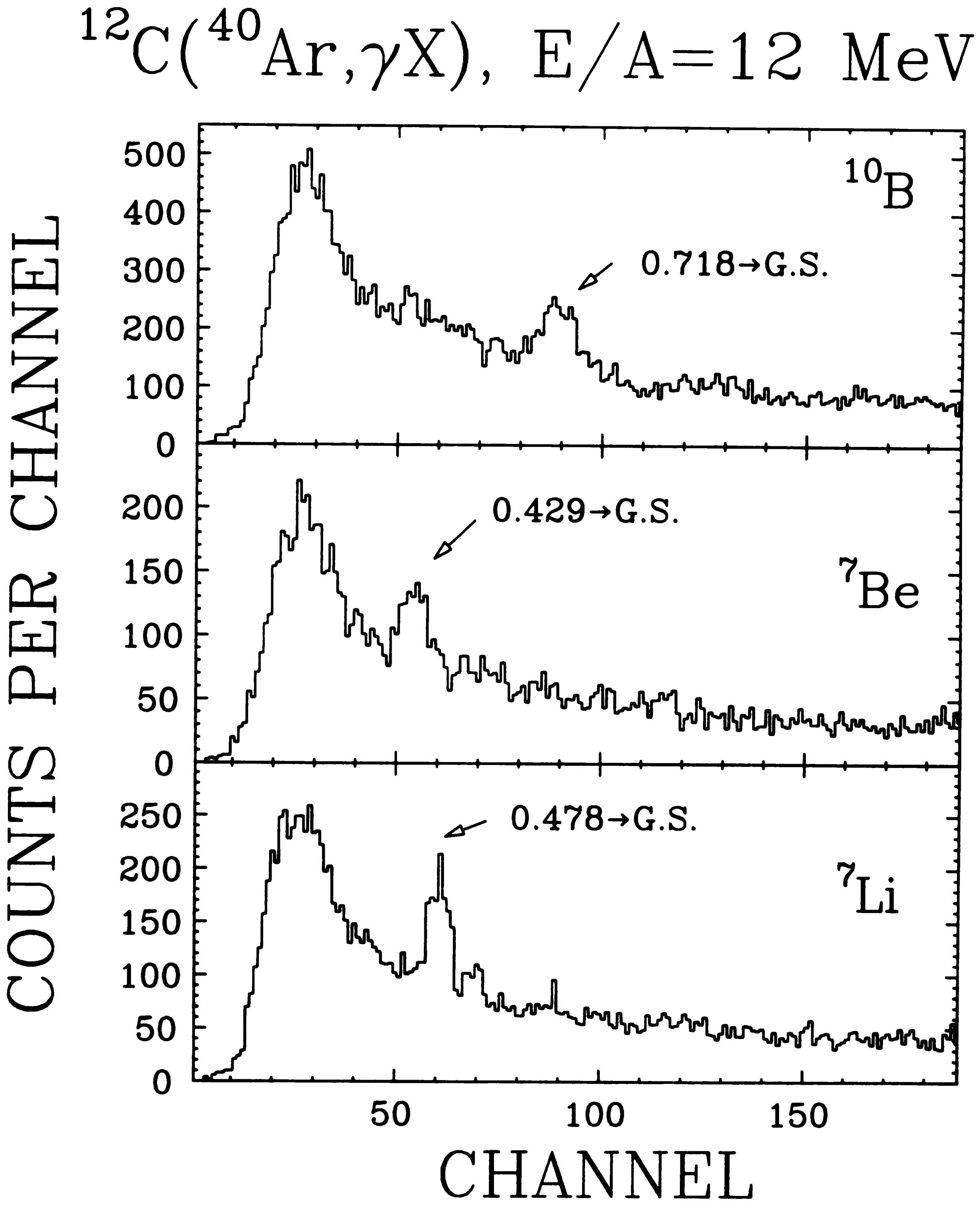

Figure IV.3.1 (cont'd.) c) At E/A=12 MeV.

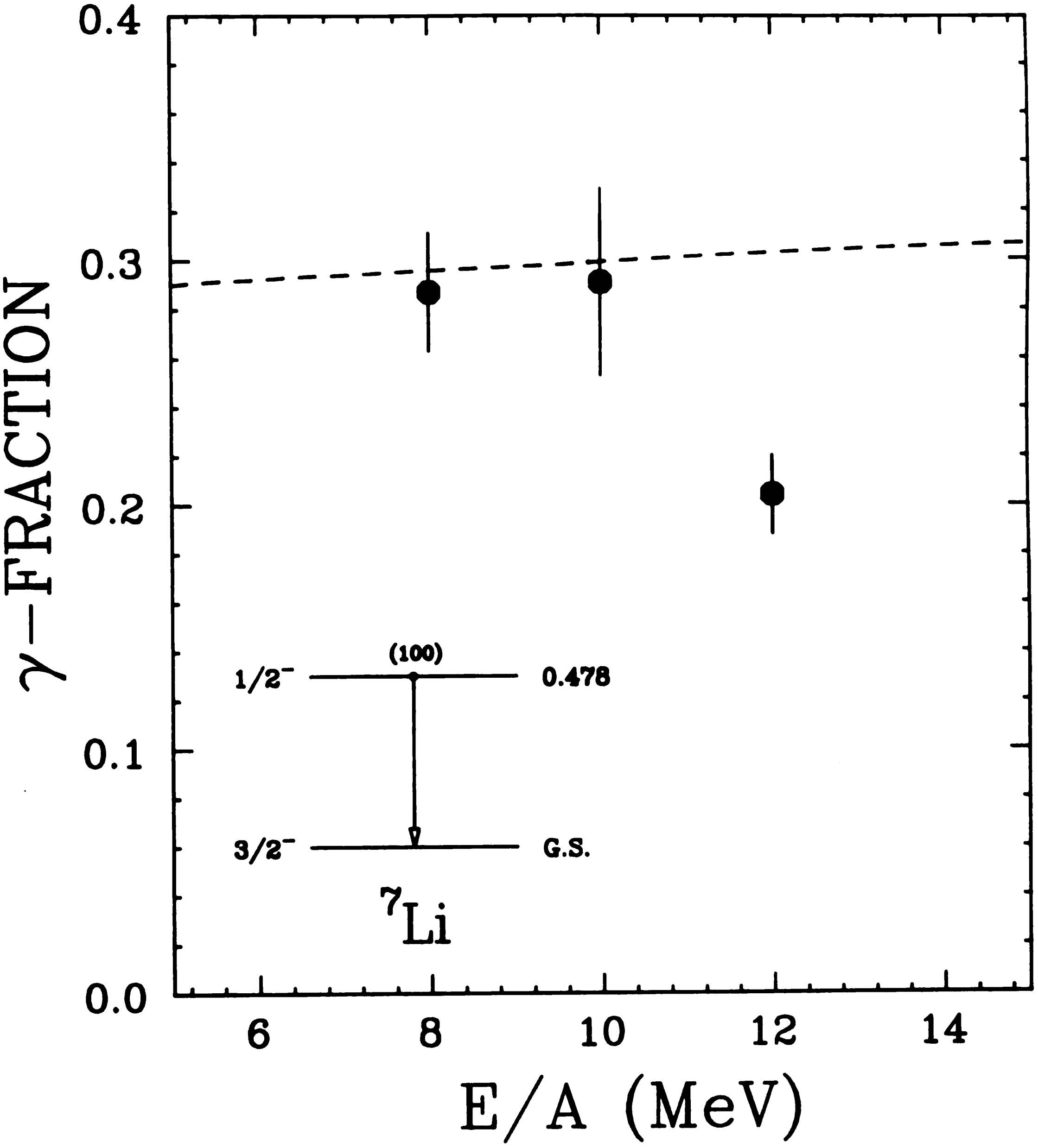

Figure IV.3.2 Y-fractions. Dashed line represents the predicted Y-fractions with the Fermi gas model temperatures. Decay schemes are from Refs. Aj84 and Aj85. a) For ^{7}Li.

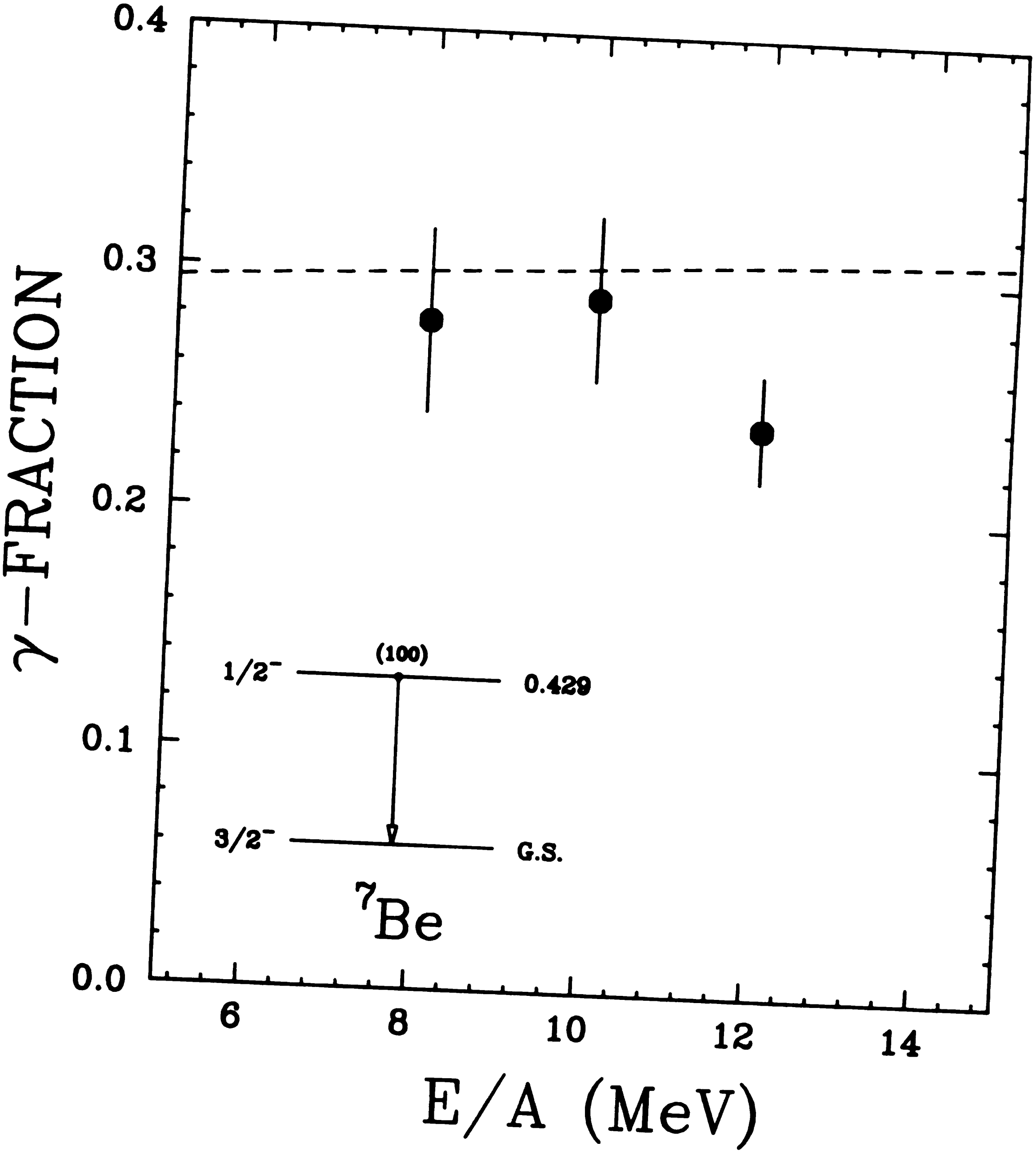

Figure IV.3.2 (cont'd.) b) For ^{7}Be.

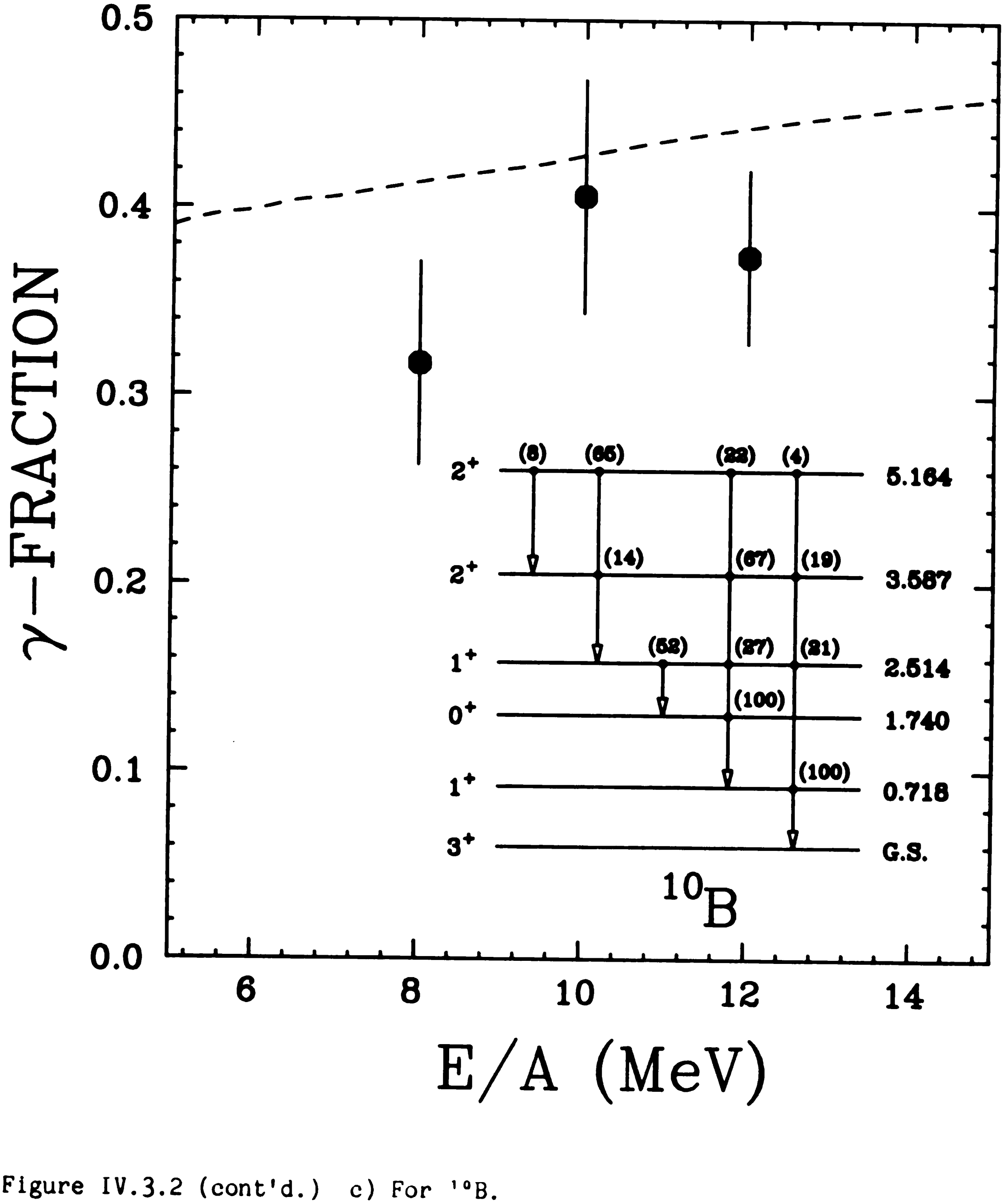

Figure IV.3.2 (cont'd.) c) For ^{10}B.

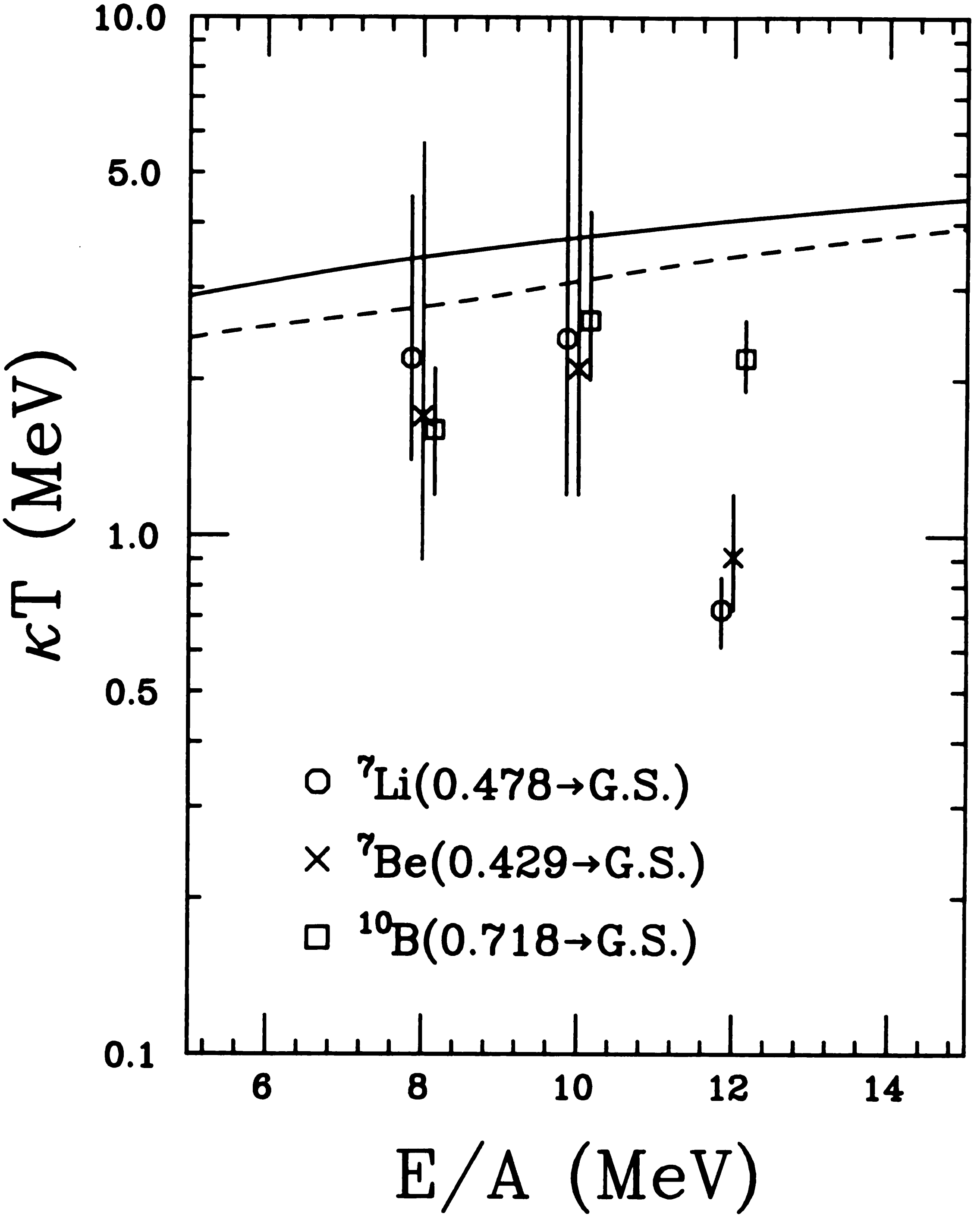

Figure IV.3.3 The observed temperatures from the γ-ray transitions in the light fragments. See the text for the lines.

Table IV.3.1 Deduced nuclear temperatures from ^{7}Li, ^{7}Be, and ^{10}B.

E/A (MeV)	Isotope	E_γ (KeV)	Decay	f_C a)	N_γ	f	κT (MeV)
8	^{7}Li	478	0.48→g.s.	0.296	1220±100	0.287±0.024	$2.2^{+2.3}_{-0.8}$
	^{7}Be	429	0.43→g.s.	0.300	220±30	0.279±0.038	$1.7^{+4.0}_{-0.8}$
	^{10}B	718	0.72→g.s.	0.397	473±80	0.317±0.054	$1.6^{+0.5}_{-0.4}$
10	^{7}Li	478	0.48→g.s.	0.300	230±30	0.291±0.038	$2.4^{+20}_{-1.2}$
	^{7}Be	429	0.43→g.s.	0.303	260±30	0.290±0.034	$2.1^{+7.9}_{-0.9}$
	^{10}B	718	0.72→g.s.	0.412	594±90	0.406±0.062	$2.6^{+1.6}_{-0.6}$
12	^{7}Li	478	0.48→g.s.	0.303	670±50	0.204±0.016	$0.72^{+0.11}_{-0.10}$
	^{7}Be	429	0.43→g.s.	0.306	550±50	0.238±0.022	$0.91^{+0.29}_{-0.19}$
	^{10}B	718	0.72→g.s.	0.424	1572±190	0.374±0.046	$2.2^{+0.4}_{-0.3}$

a) Predicted gamma-fraction. See the text for detail.

singles inclusive spectra by the ground state of ^{8}Be [Wo72, Bl86] is taken into account in determining the gamma-fraction for ^{7}Li. For the nucleus ^{10}B, there are a few unbound states above the particle threshold energy (4.46 MeV) which decay partially by gamma-ray emission [Fo66, Ne70, Re72, Aj84]. However, only the 5.164 MeV state has a comparable gamma-width relative to the total decay-width (Γ_γ/Γ=87% for the 5.164 MeV while Γ_γ/Γ<1% for the other unbound states in ^{10}B [Aj84]). Since the half-life of the 0.718 MeV state in ^{10}B is about 1.02 ns, which corresponds to a 5 cm flight distance on the average at E/A=10 MeV, errors which may be caused from the change in geometrical efficiencies of the gamma-ray detectors and also from the wrong Doppler shift corrections must be included. Although the estimation of the change in the geometrical efficiency of the gamma-ray detector becomes a formidable calculation because of the cylindrical shape of the crystal, a rough estimate gave a possible error of 10% from these sources, and this was combined with the statistical uncertainties for ^{10}B. As one may see in Figures IV.3.2(a-c) and as Morrissey et al. pointed out [Mo84a, Mo85a], the small energy level spacings of these nuclei limit the sensitivity of their population distributions to temperatures of a few MeV or less, especially for ^{7}Li and ^{7}Be. This indicates that a few percent change due to statistical fluctuations in the gamma-fraction at a few MeV temperature, for example, κT=3 MeV, can make the upper limit of the deduced temperature infinity. In terms of this sensitivity problem, ^{10}B is a better probe of statistical equilibrium than the other two nuclei under consideration because it has a wider level spacing, and also feeding from the higher-lying bound states to 0.72 MeV state improve the sensitivity of the gamma-fraction to temperatures.

Deduced temperatures for light fragments are plotted as a function of the beam energy in Figure IV.3.3. The solid curve drawn in Figure IV.3.3 represents the predicted temperatures in the Fermi gas model without correction for the rotational energy, and the dashed curve represents those in the Fermi gas model with subtracting the rotational energy from the excitation energy (as described in Section III.4). The overall results, which are tabulated in Table IV.3.1, include the gamma-ray counts (N_γ), the gamma-fractions (f), and the deduced temperatures (κT) for light fragments. Errors in the temperature are asymmetric due to the logarithmic form of the gamma-fraction. The statistical errors and systematic errors in evaluating the gamma-ray counts dominated the other sources of error. This will be discussed further in Sec. IV.5.

Temperatures at E/A=8 MeV and 10 MeV agree well with those predicted, and this is consistent with the result in Ref. Mo86a. In this reference, where the population distribution of states in light nuclei was studied in a reaction of ^{12}C + ^{14}N at beam energies including E/A=8 MeV and 12 MeV, the deduced temperatures at up to E/A=8 MeV, but not above E/A=12 MeV, agree with the calculated temperatures with the rotational energy taken into consideration in the Fermi gas model, hence indicating consistency with the simple thermal equilibrium at beam energies below E/A=8 MeV. Measurements at E/A=10 MeV are not included in this reference; however data in the present experiment indicate that simple thermal equilibrium may prevail at this energy, too. As shown in Figure 3 in Ref. Mo86a, subtraction of the average rotational energy from the excitation energy lowers the calculated temperatures significantly especially at bombarding energies below E/A=12 MeV. In contrast, since the bigger compound nuclear system in the present experiment has a larger moment of inertia than the smaller system in Ref. Mo86a, this reduces the fraction of the average rotational energy in the excitation energy [e.g., in Ref. Mo86a, the calculated temperatures with and without subtracting the rotational energy at E/A=8 MeV are 3.0 and 1.4 MeV, respectively, while in the present reaction they are 3.4 and 2.8 MeV]. Figure 3 in Ref. Mo86a and Figure IV.3.3 show a fair agreement with this argument, except that the temperature of 2.3 MeV from ^{10}B at E/A=12 MeV in this measurement roughly agrees with the prediction while those from nuclei of A=7 are significantly lower than that predicted under the assumption of simple thermal equilibrium (in ref. Mo86a, it is shown that the temperatures are independent of the nucleus at the same energy; this argument agrees with our data at E/A=8 and 10 MeV, however it is not true at E/A=12 MeV). This discrepancy may be due, among other reasons, to the effect of preferential feeding from higher-A nuclear system on the population distribution of complex fragments, rather than being due to the non-equilibrium effects at E/A=12 MeV, and this will be discussed further in the following section (Sec. IV.4) after considering the population distribution of intermediate fragments. Nevertheless, it was indicated that the population distribution of nuclear states in light fragments is dominated by the excitation energy (or temperature) of the equilibrated composite system in low energy reactions. However the results also show that the correction made by subtraction of the average rotational energy from the excitation energy must be taken into account.

On the other hand, the temperatures given in Figure IV.3.3 show a self-consistency between a pair of mirror nuclei, ^{7}Li and ^{7}Be. As shown in Figures IV.3.2(a-b), both the nuclei have only one bound-excited state each with the same spin of $\frac{1}{2}^+$, very close excitation energies of 0.478 MeV and 0.429 MeV, respectively, and the ground state with the same spin of $\frac{3}{2}^+$. Should the preferential feeding of any level by the decay of unbound higher mass nuclei [Ha87, Mo85a, Mo84a, St83] play an important role in populating the light nuclei, it appears to be negligible at E/A=8 and 10 MeV at least for ^{7}Li and ^{7}Be in the present reaction. However, one should not exclude the possibility that the amount of feeding to the excited states and the ground state were accidentally proportional to the original populations in each state, although this is not expected from the energetics and penetrability of these decays.

IV.4 Intermediate Fragments

By virtue of the individual particle identification for intermediate fragments (up to ^{23}Na) and relatively well known information for the spin, the excitation energy, and the gamma-branching ratio of each bound state in this mass region, the temperature measurement [Mo86a, Mo85a, Mo84a] based on the population distribution of nuclear states was applied in the intermediate fragment regime for the first time. Gamma-rays in coincidence with these fragments were detected in the NaI(Tl) detectors. Analysis of these data followed a similar track as that for light fragments. Figures IV.4.1(a-h) show the Doppler shift corrected gamma-rays in coincidence with ^{16}N, ^{17}O, ^{18}O, ^{19}F, ^{20}Ne, ^{21}Ne. ^{22}Ne, and ^{23}Na, respectively. The gamma-fraction for each peak was determined according to Eq. IV.3, and is shown in Figures

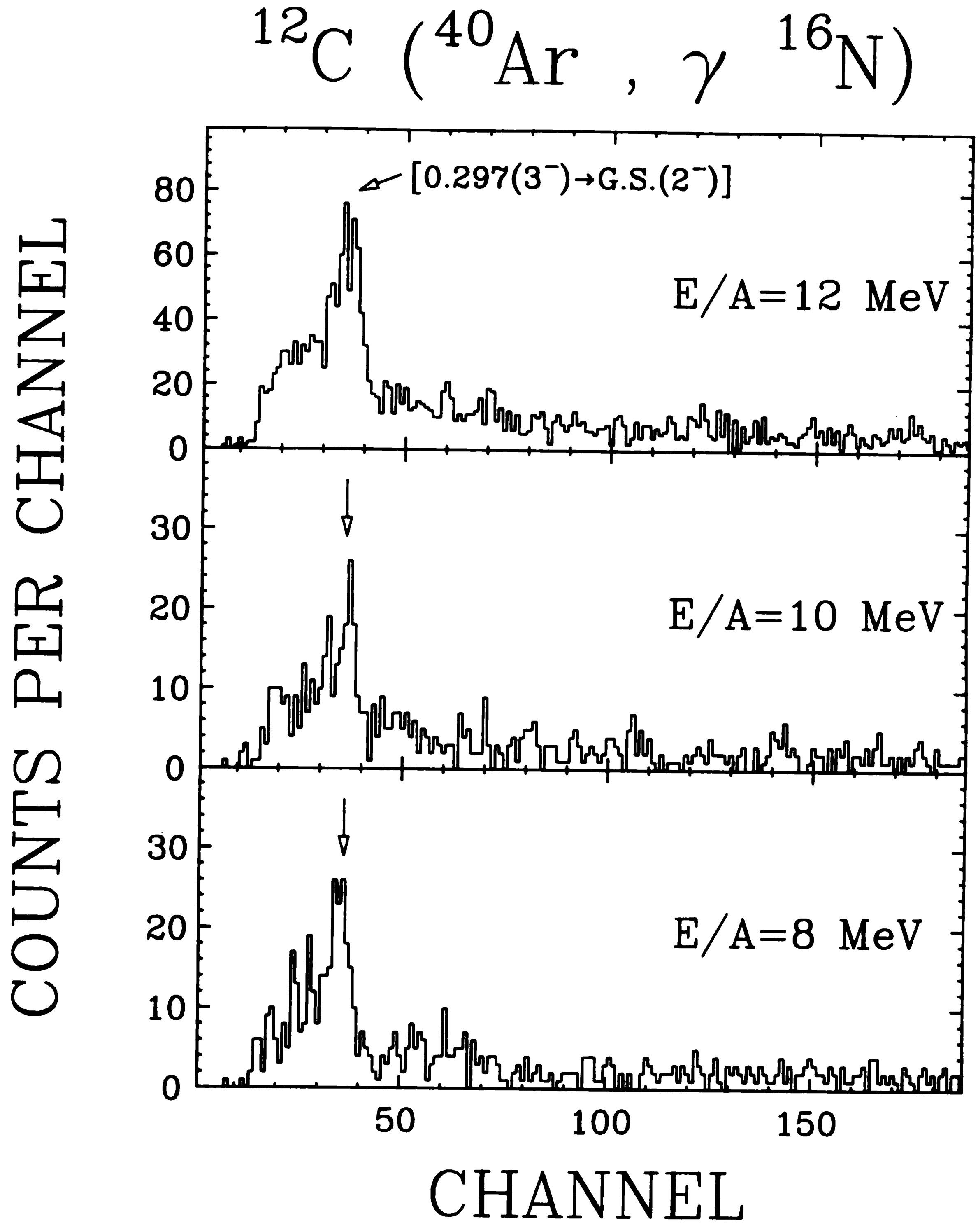

Figure IV.4.1 Doppler-shift corrected γ-ray energy spectra (NaI) in coincidence with intermediate fragments. a) With ^{16}N.

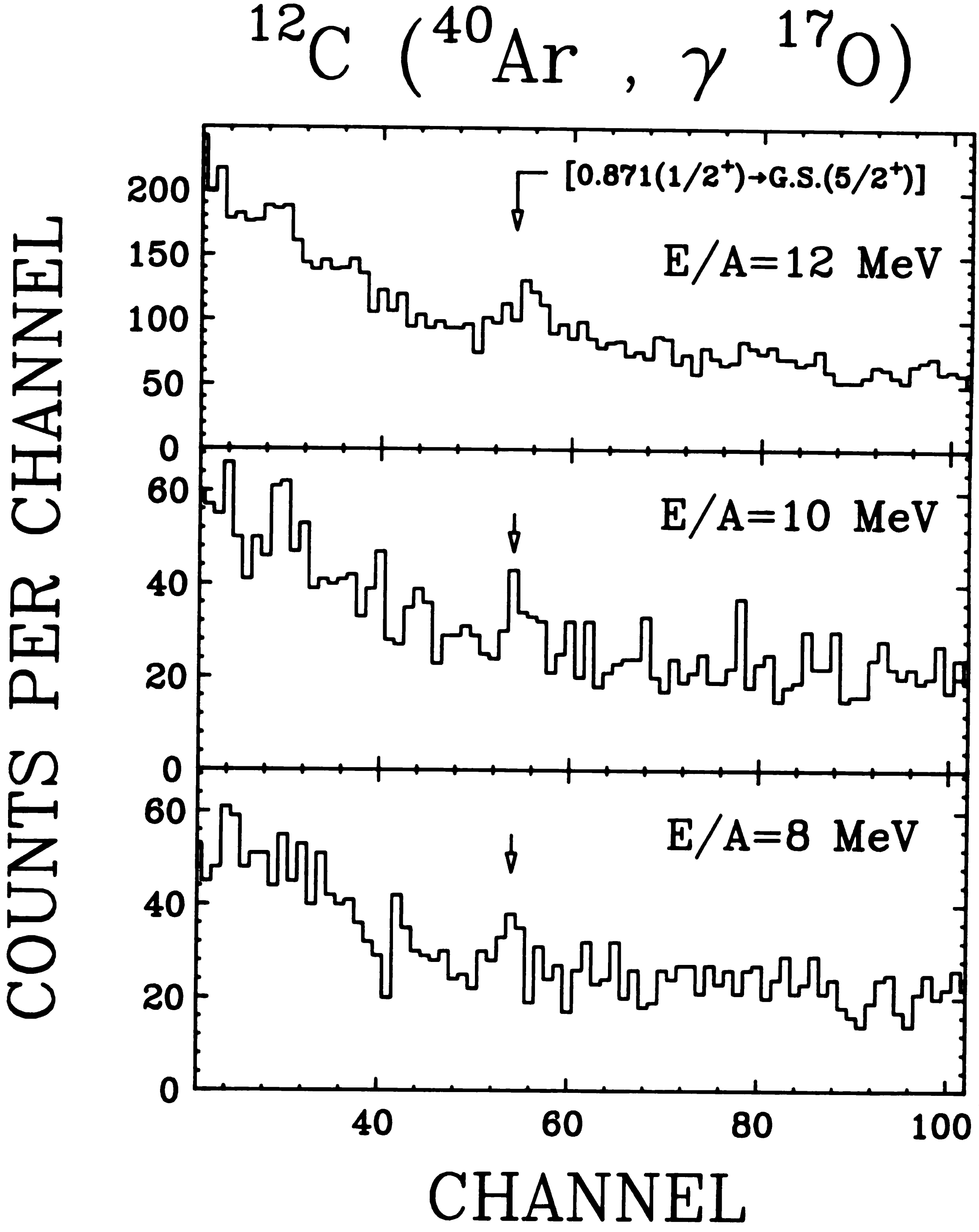

Figure IV.4.1 (cont'd.) b) With ^{17}O.

COUNTS PER CHANNEL

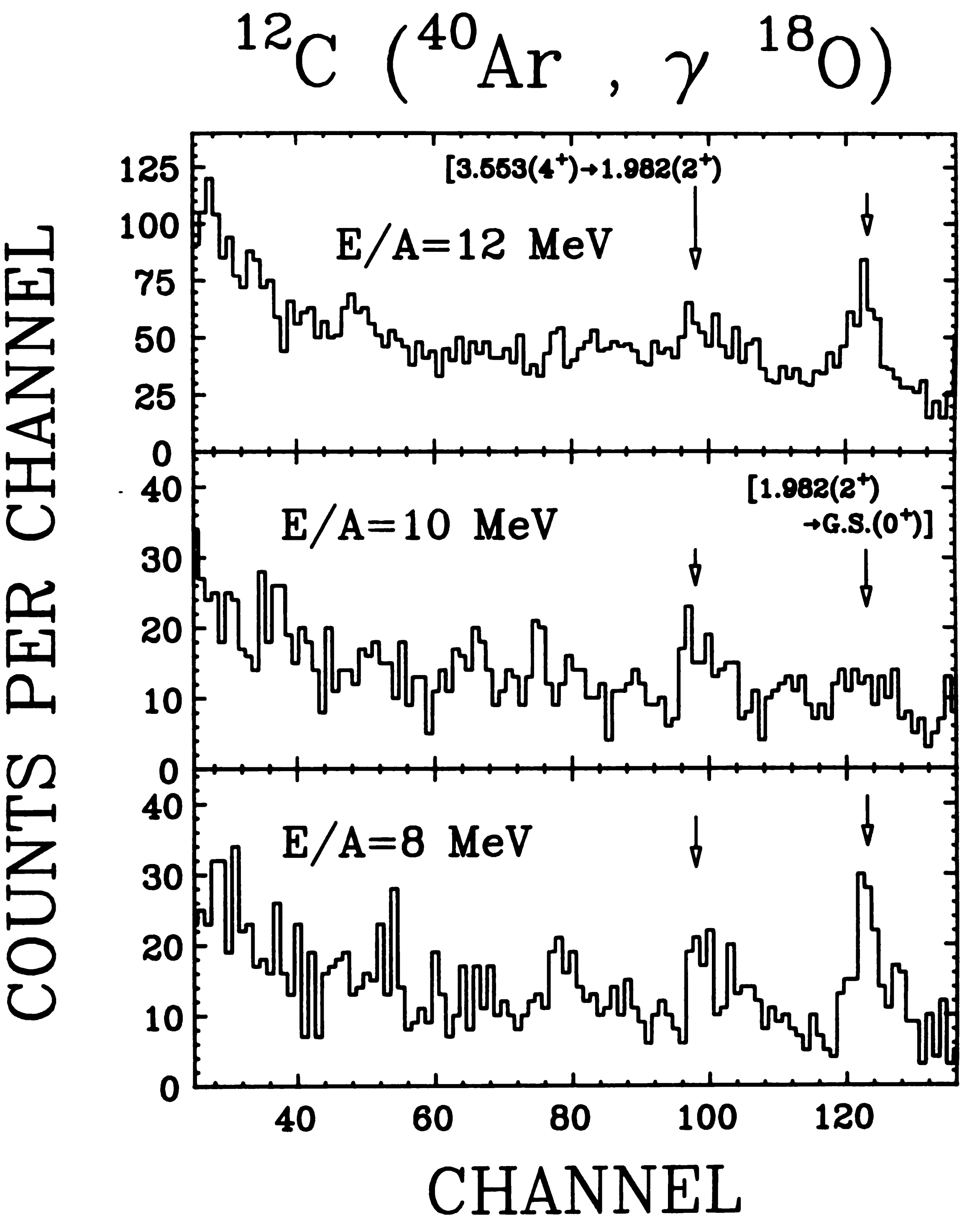

Figure IV.4.1 (cont'd.) c) With ^{18}O.

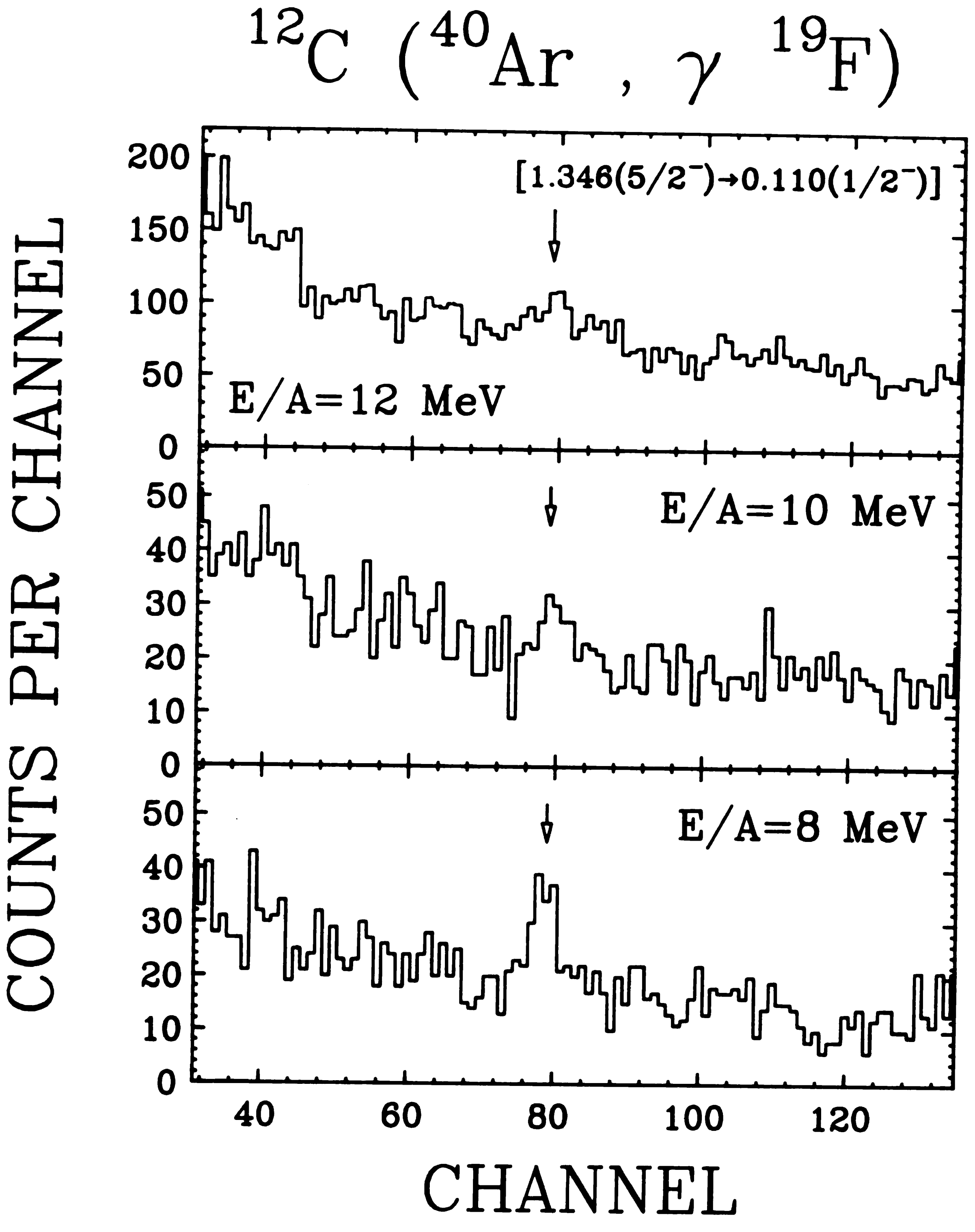

Figure IV.4.1 (cont'd.) d) With ^{19}F.

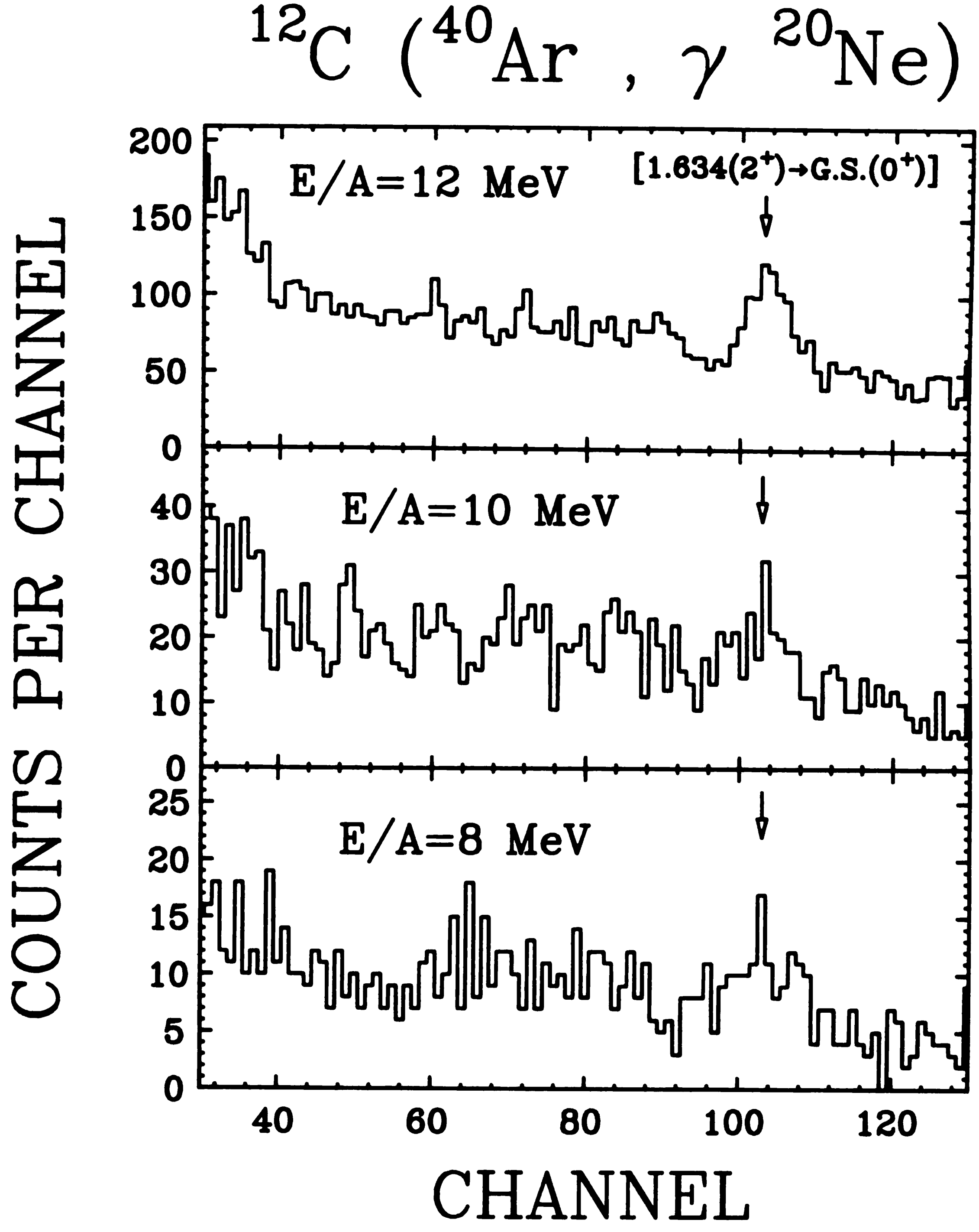

Figure IV.4.1 (cont'd.) e) With ^{20}Ne.

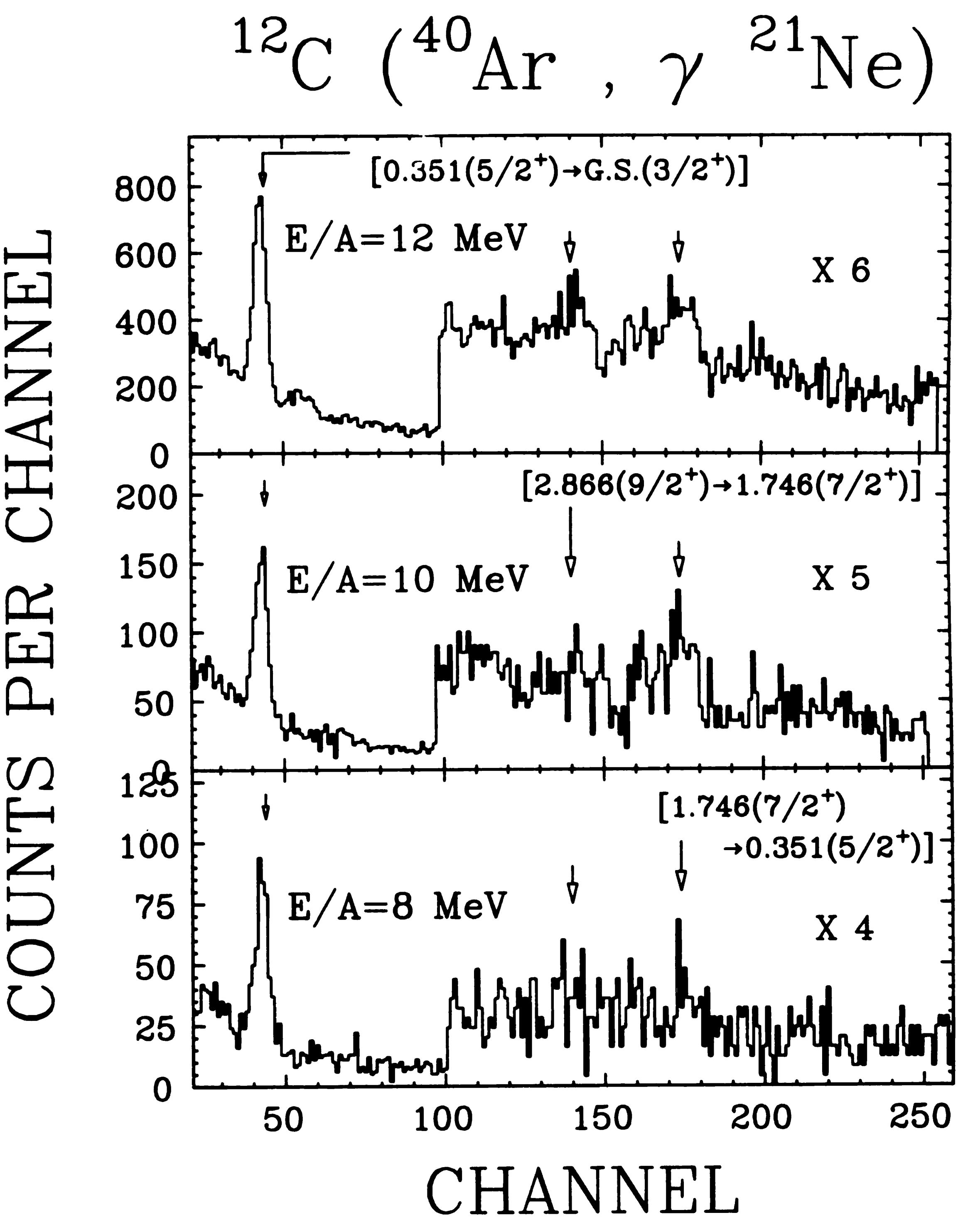

Figure IV.4.1 (cont'd.) f) With ^{21}Ne.

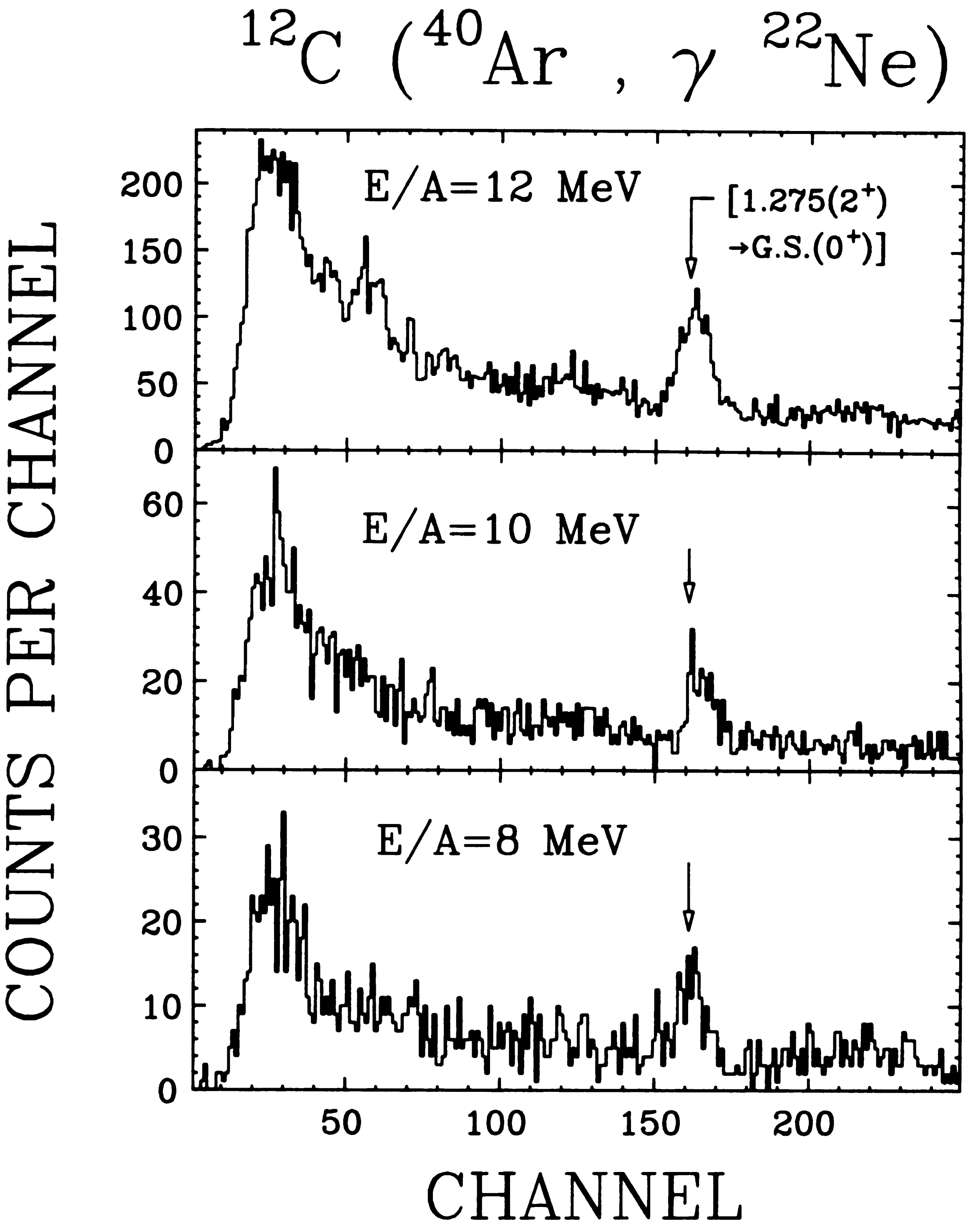

Figure IV.4.1 (cont'd.) g) With ^{22}Ne.

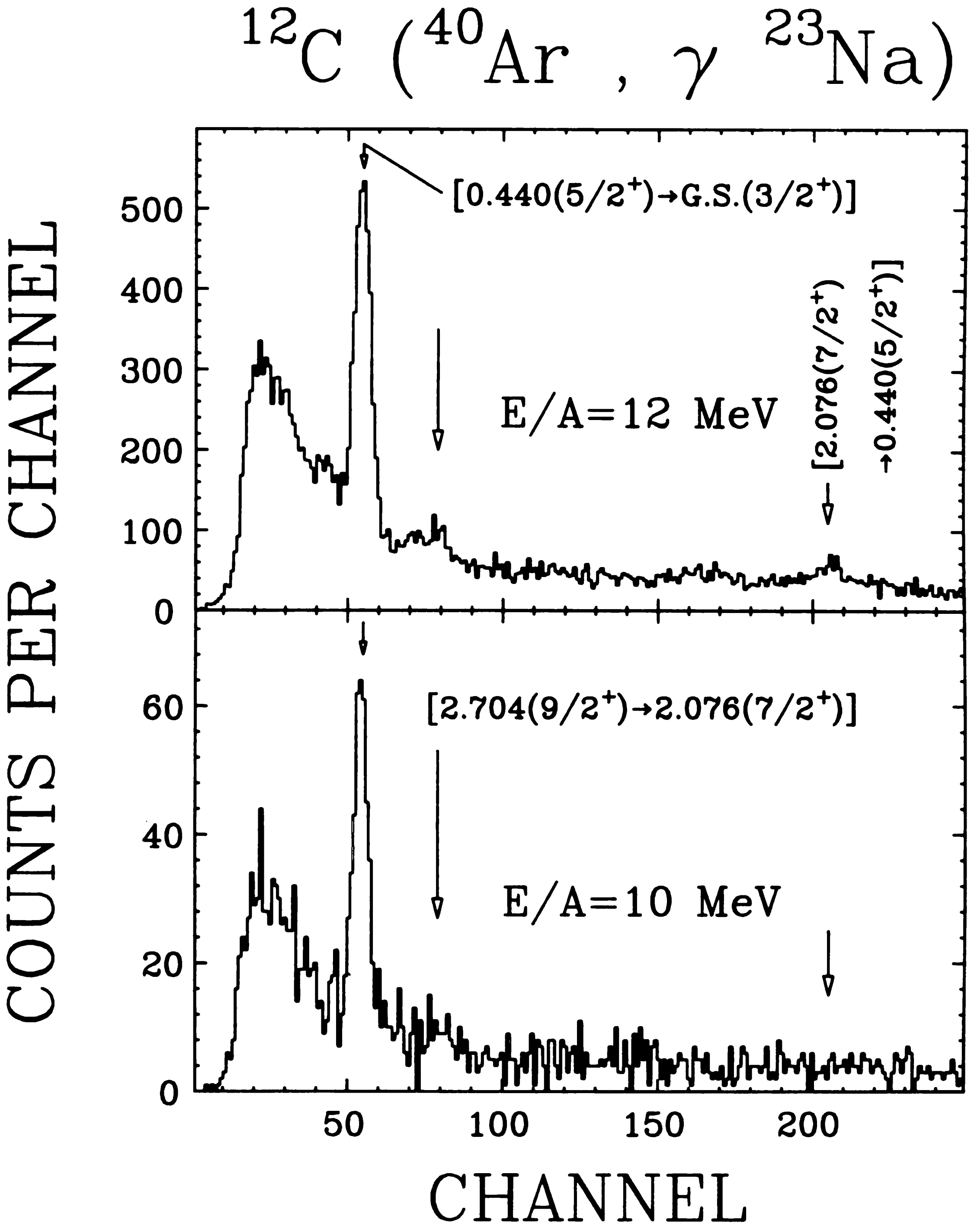

Figure IV.4.1 (cont'd.) h) With ^{23}Na.

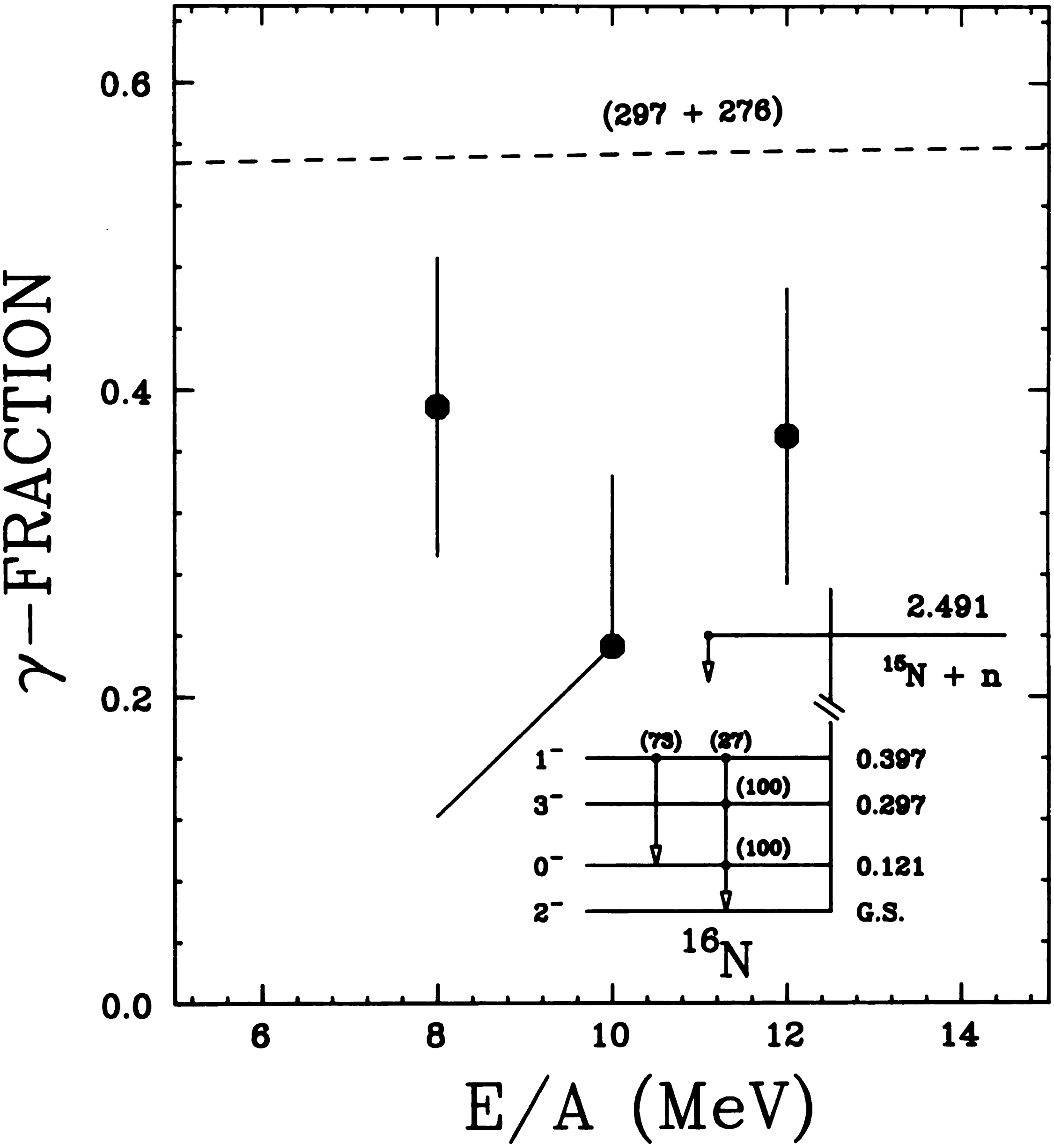

Figure IV.4.2 Y-fractions. Lines are the predicted Y-fractions with the Fermi gas model temperatures. Decay schemes are from Refs. Aj83 and Aj86. a) For ^{16}N.

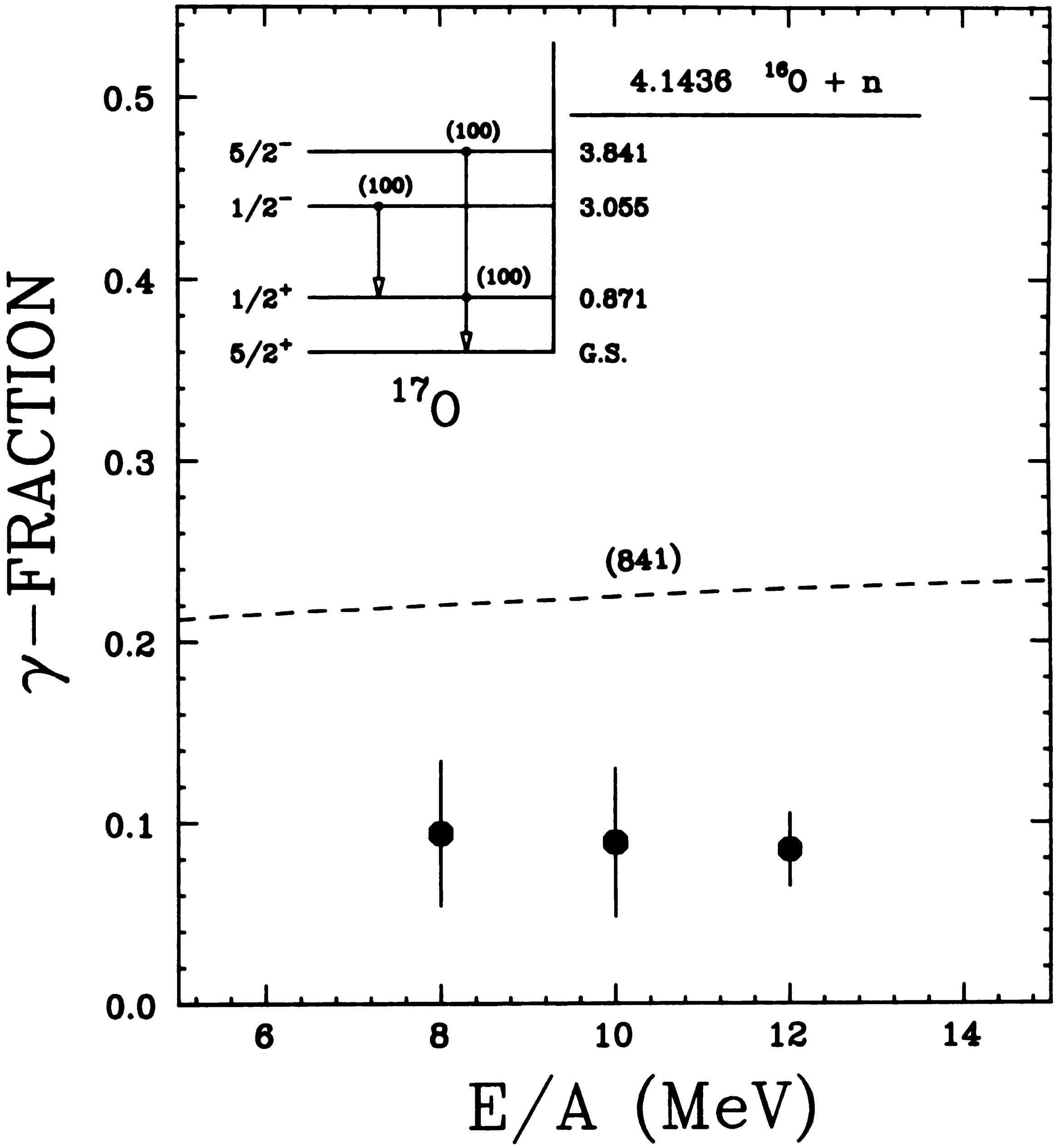

Figure IV.4.2 (cont'd.) b) For ^{17}O.

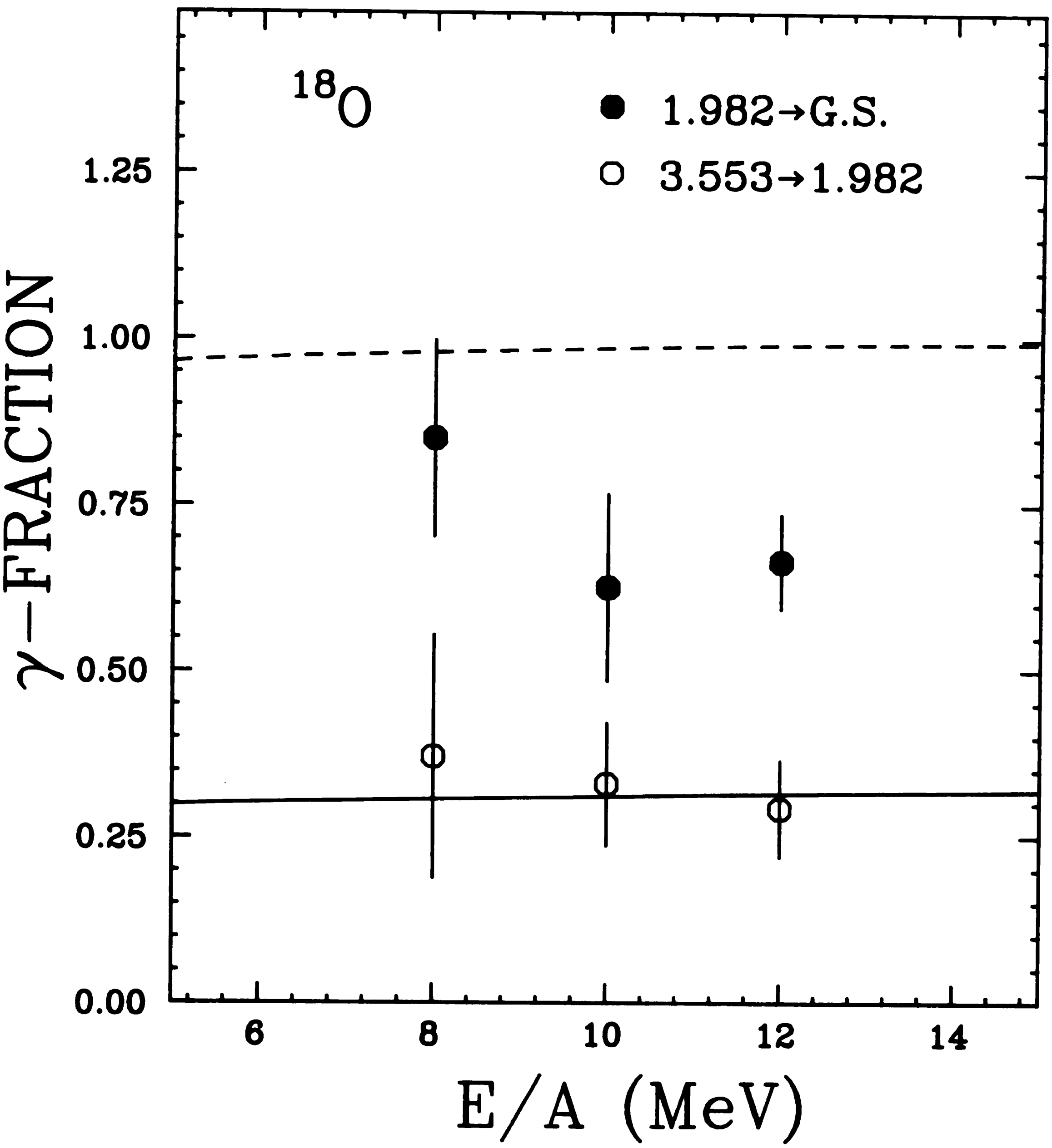

Figure IV.4.2 (cont'd.) c) For ^{18}O.

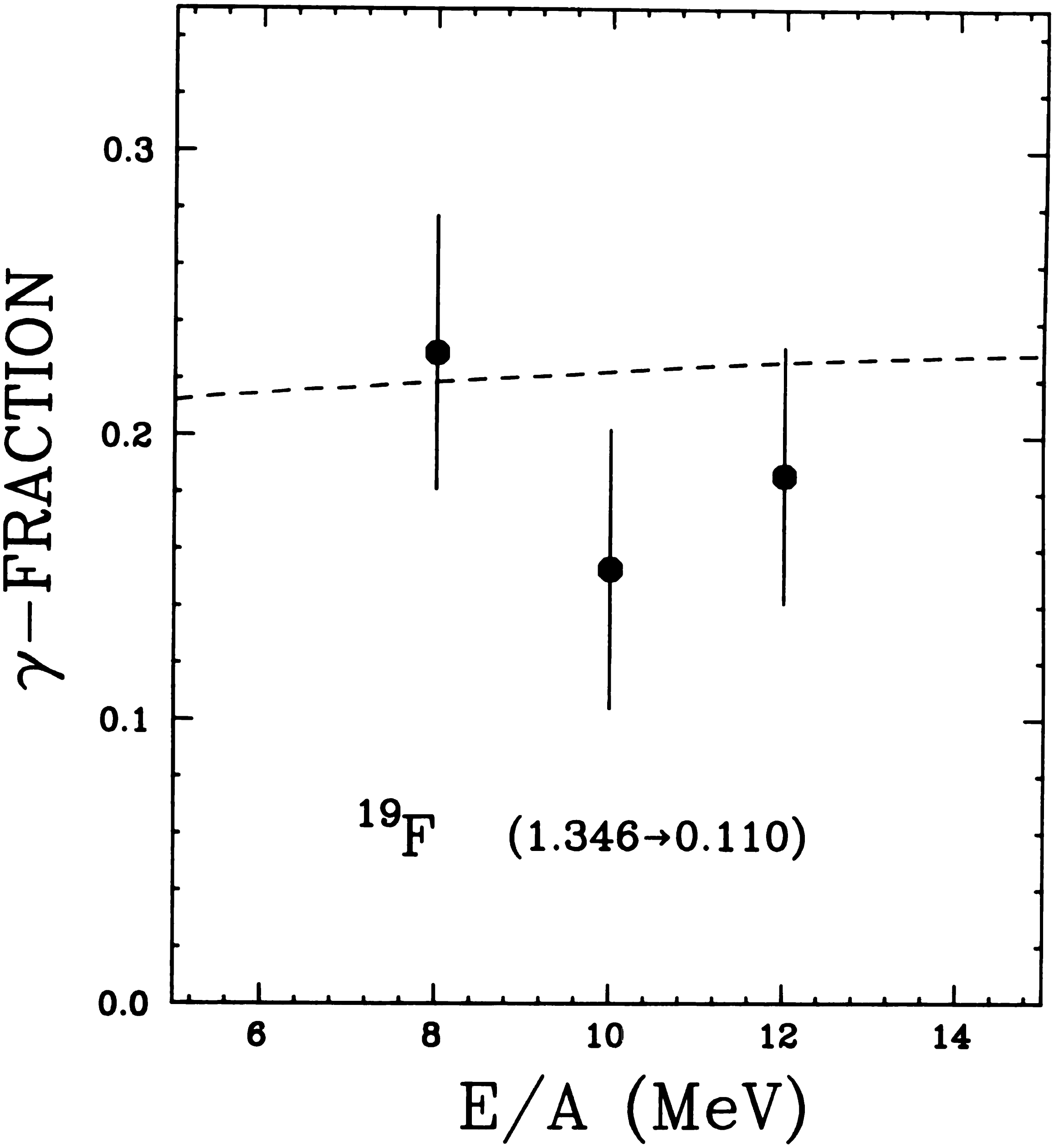

Figure IV.4.2 (cont'd.) d) For ^{19}F.

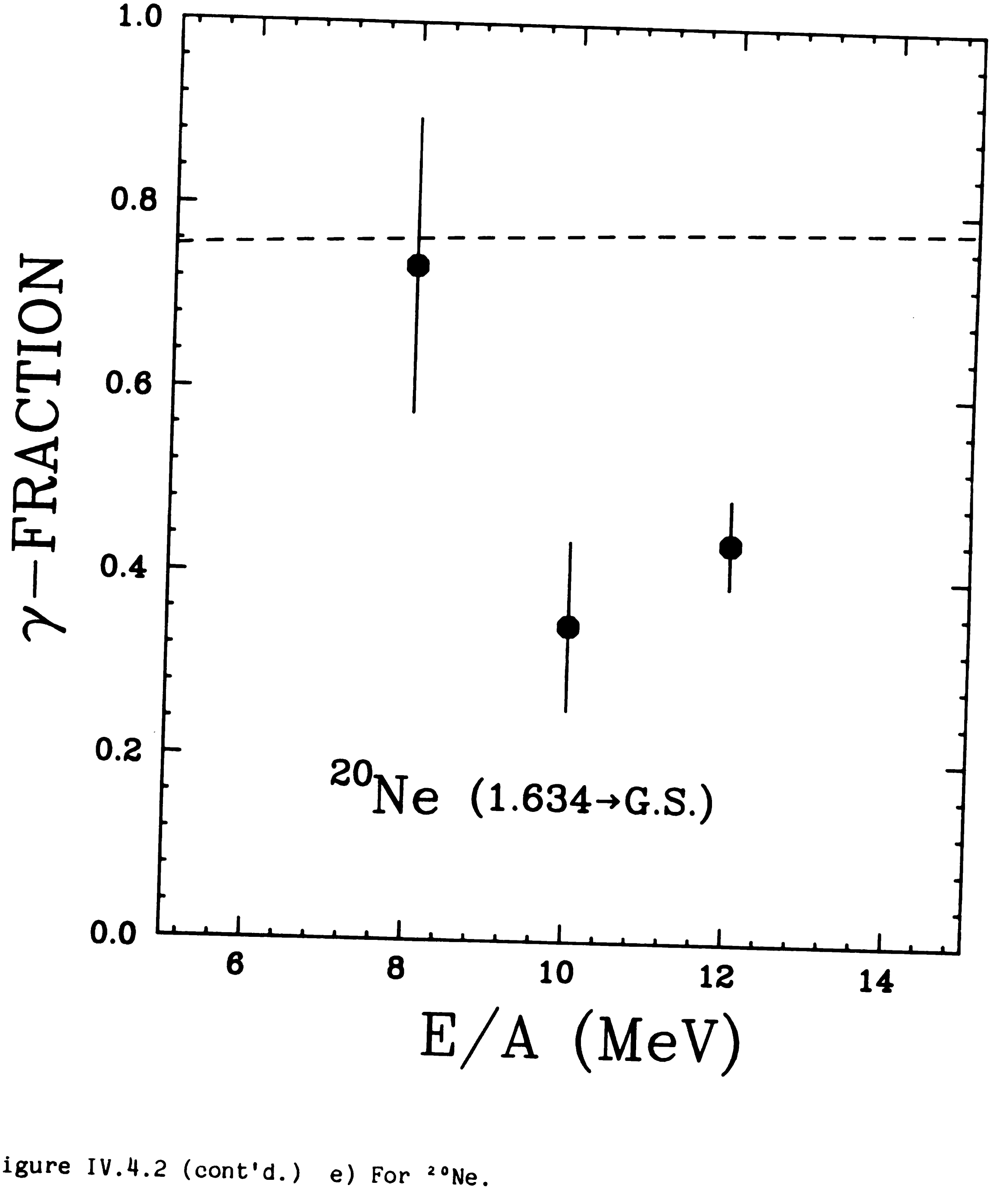

Figure IV.4.2 (cont'd.) e) For ^{20}Ne.

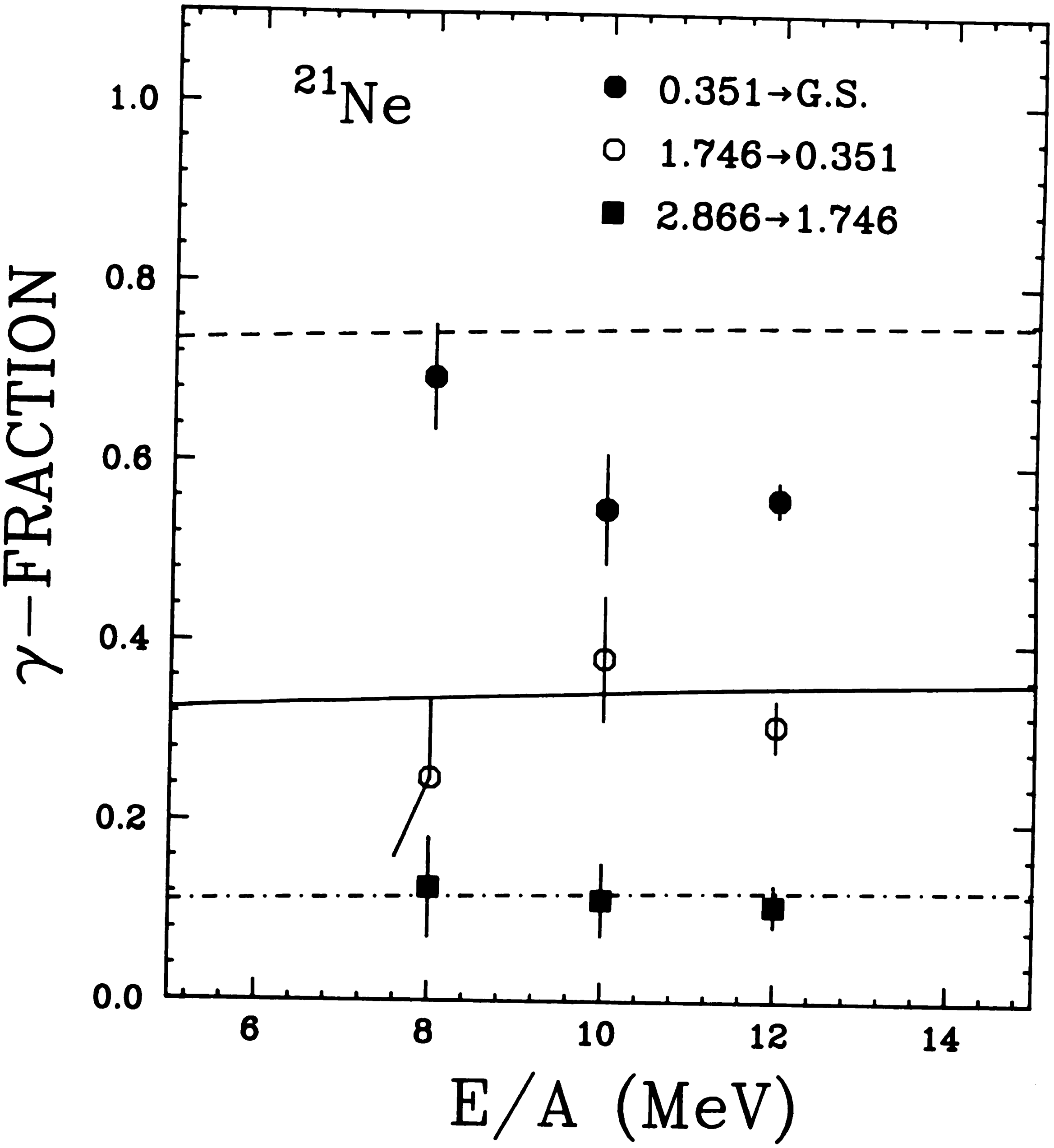

Figure IV.4.2 (cont'd.) f) For ^{21}Ne.

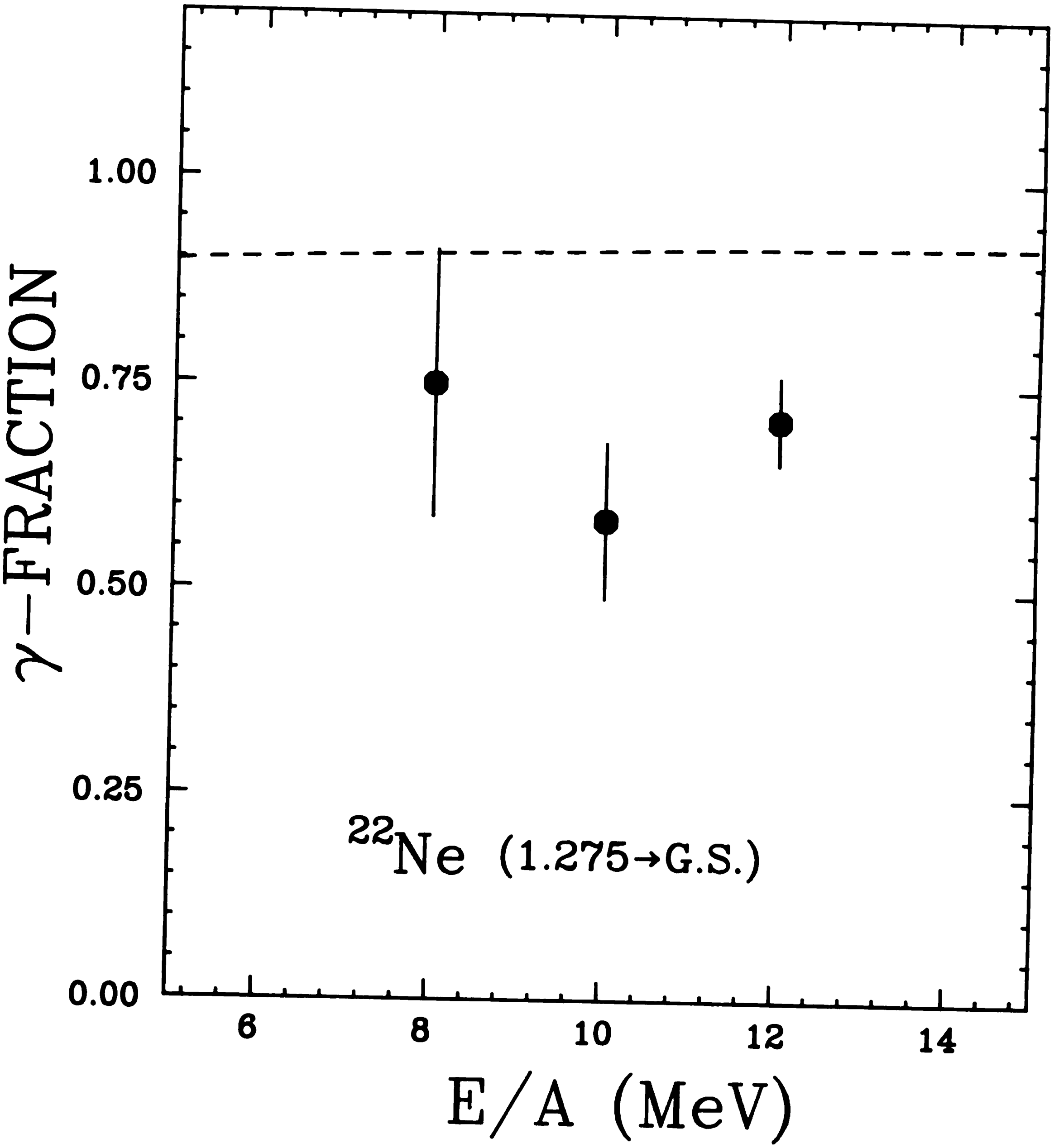

Figure IV.4.2 (cont'd.) g) For ^{22}Ne.

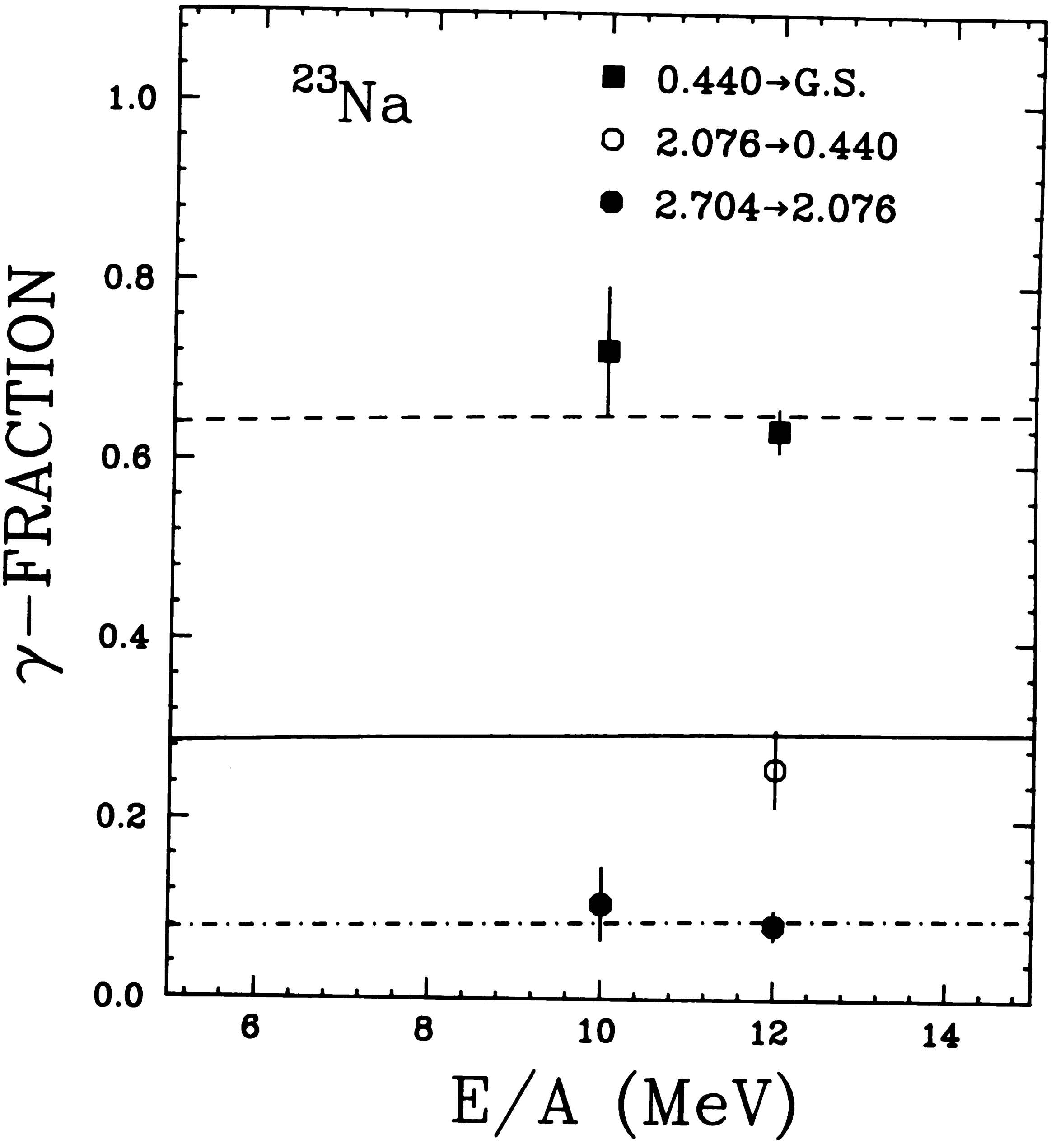

Figure IV.4.2 (cont'd.) h) For ^{23}Na.

IV.4.2(a-h). The superimposed curves drawn in Figures IV.4.2(a-h) are the predicted gamma-fractions for the observed gamma-lines by means of Eq. IV.4 with temperatures predicted in the Fermi gas model. Errors included in these figures are mainly due to the statistical uncertainties and the systematic uncertainties, which will be discussed in Sec. IV.5. The possible errors in the level information were ignored. The characteristic of each nucleus regarding the information about the level and gamma-branching ratios and the observed gamma-rays is as follows:

a) ^{16}N. There are 3 excited states below the neutron-threshold energy, 2.491 MeV, as shown in Figure IV.4.2a. No state above this threshold decays through the emission of gamma-rays [Aj86]. A gamma-ray peak of E_γ=297 KeV [0.297(3^-) → 0(2^-)] in Figure IV.4.1a was not separated from E_γ=276 KeV [0.398(1^-) → 0.120(0^-)], and the contribution from E_γ=276 KeV was taken into account in the gamma-fraction of E_γ=297 KeV.

b) ^{17}O. As shown in Figure IV.4.2b, 3 bound excited states decay by the emission of gamma-rays. There are a number of excited states above the neutron-threshold energy, 4.1436 MeV, which decay partially by gamma-ray emission; however the gamma-widths of those states were much smaller than the decay-widths (smaller than 1%) [Aj86, Sm86]. Only E_γ=871 KeV was in the detection range of the NaI(Tl) detectors.

c) ^{18}O. A number of levels above the alpha-particle threshold energy, 6.2279 MeV, still decay in full by gamma emission [Aj83]. Only the state of 7.117 MeV (4^+) among those which decay partially through gamma-ray emission has a comparable gamma-width to the particle decay-width ($\Gamma_\gamma/\Gamma_\alpha$=0.9±0.1) [Aj83]. Contamination from E_γ=1650 KeV [3.632(0^+) → 1.982(2^+)] to E_γ=1571 KeV [3.553(4^+) → 1.982(2^+)] and that from E_γ=1937 KeV [3.919(2^+) → 1.982(2^+)] to E_γ=1982 KeV [1.982(2^+) → 0(0^+)] was taken into account in the determination of the gamma-fractions.

d) ^{19}F. Excited states up to E=4.648 MeV decay in full by the emission of gamma-rays. The alpha-particle threshold energy is 4.0138 MeV [Aj83]. Gamma-decays from the states above 4.648 MeV are negligible, and a gamma-fraction for E_γ=1236 keV [1.346($\frac{5}{2}^-$) → 0.110($\frac{1}{2}^-$)] was determined in this nucleus.

e) ^{20}Ne. A number of excited states above the alpha-particle threshold energy, 4.7309 MeV [Aj83], decay in full via gamma-ray emission. There are also a number of unbound excited states which decay partially into lower states through gamma-ray emission, however only the state of 5.621(3^-) has a comparable ratio of $\Gamma_\gamma/\Gamma \approx 7$ %. The transition from 1.634(2^+) to 0(0^+) is the most prominent one in this nucleus. The uncertainty in the spin assignments for those states which decay through gamma-ray emission becomes a problem for this nucleus and the heavier ones. However for this nucleus the only states with uncertain spin assignments are 10.69, 11.53, and 11.56 MeV [Aj83], and therefore the error caused from the uncertain spin assignments would be negligible as compared to the statistical uncertainty.

f) <u>^{21}Ne</u>. Gamma-rays of E_γ=351 KeV [$0.351(\frac{5}{2}^+) \rightarrow 0(\frac{3}{2}^+)$], 1120 KeV [$2.866(\frac{9}{2}^+) \rightarrow 1.746(\frac{7}{2}^+)$], and 1395 KeV [$1.746(\frac{7}{2}^+) \rightarrow 0.351(\frac{5}{2}^+)$] are detected in coincidence with fragments of this nucleus. Gamma-branching ratios of excited states below the neutron-threshold energy, 6.76 MeV, are relatively well known, however the spin assignment for many of those states is given as a range of possibilities [En78, Wa81]. In such a case, a median value of the spins was used in the calculation of the predicted gamma-fraction.

g) <u>^{22}Ne</u>. The spin of each state below 7.4 MeV is well known experimentally, while the alpha-particle threshold energy is 9.67 MeV [En78]. For the states, for which the spins are completely unknown, a spin assignment for each state was made by assuming an E1 or M1 transition. Although the application of the new temperature measurement to this nucleus and the heavier ones is less plausible because of the limited information about the spin assignments for the high-excited states, one must note that the feeding from those highly excited states would not be as important as that from relatively low-lying excited states if the population of each state was distributed according to Eq. IV.1, and the temperature is close to the predicted value (~3 MeV). This means that the uncertainty arising from the poorly known spin assignments for the high-lying states may not bring a major shift in the predicted gamma-fraction. Hence the comparison of gamma-fractions between the measured and the predicted still remains an interesting topic. A prominent peak of E_γ=1275 KeV [$1.275(2^+) \rightarrow 0(0^+)$] was observed in this case.

h) <u>^{23}Na</u>. Each gamma-fraction for E_γ=440 KeV [0.440($\frac{5}{2}^+$) → 0($\frac{3}{2}^+$)], 628 KeV [2.704($\frac{9}{2}^+$) → 2.076($\frac{7}{2}^+$)], and 1636 KeV [2.076($\frac{7}{2}^+$) → 0.440($\frac{5}{2}^+$)] was compared to that predicted by the Fermi gas model. Contamination of E_γ=1774 KeV [3.850($\frac{5}{2}^-$) → 2.076($\frac{7}{2}^+$)] was taken into consideration. The proton-threshold energy is 8.79 MeV [En78], and even though the gamma-branching ratio of each bound state is reasonably well known, the situation in the level information regarding the spin assignments is no better than that for ^{22}Ne [Vo84, En78], which may imply a larger uncertainty in the determination of the predicted gamma-fraction and the temperature. Statistics at E/A=8 MeV were not sufficient, and those at E/A=10 MeV were limited to only two peaks.

Gamma-rays in ^{20}F (656, 823, and 1001 KeV) were not included in this analysis because of the small amount of information known about the states [Fo85, Aj83, Bi75]. The temperatures deduced from the intermediate fragments are displayed in Figures IV.4.3(a-c) for each beam energy. For a nucleus with more than one gamma-ray peak, the temperature from the lowest energy gamma-line is drawn in the left side, that from the highest one is in right side, and so on. Since the gamma-fraction for this mass region is, in general, not very sensitive to the change in temperature as shown Figures IV.4.2(a-h), the statistical uncertainty due to the number of counts for each peak becomes exaggerated when the temperature is around one MeV. This leads to un upper limit of the temperature for some nuclei extending to infinity. Table IV.4.1 shows the tabulated values for Figures IV.4.2(a-h) and IV.4.3(a-c).

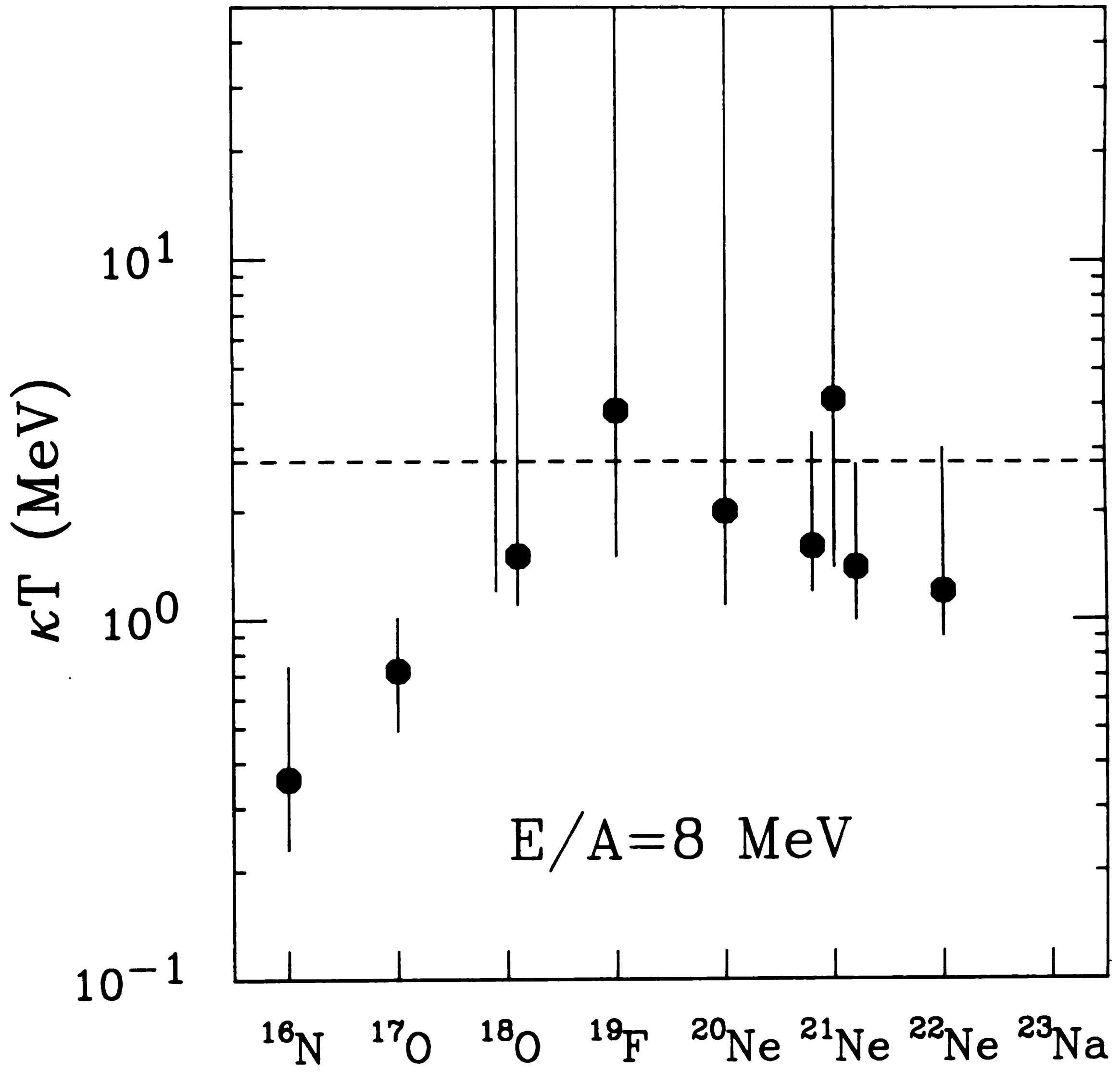

Figure IV.4.3 The observed temperatures from the γ-ray transitions of the intermediate fragments. Dashed line represents the predicted temperature in the Fermi gas model. a) At E/A=8 MeV.

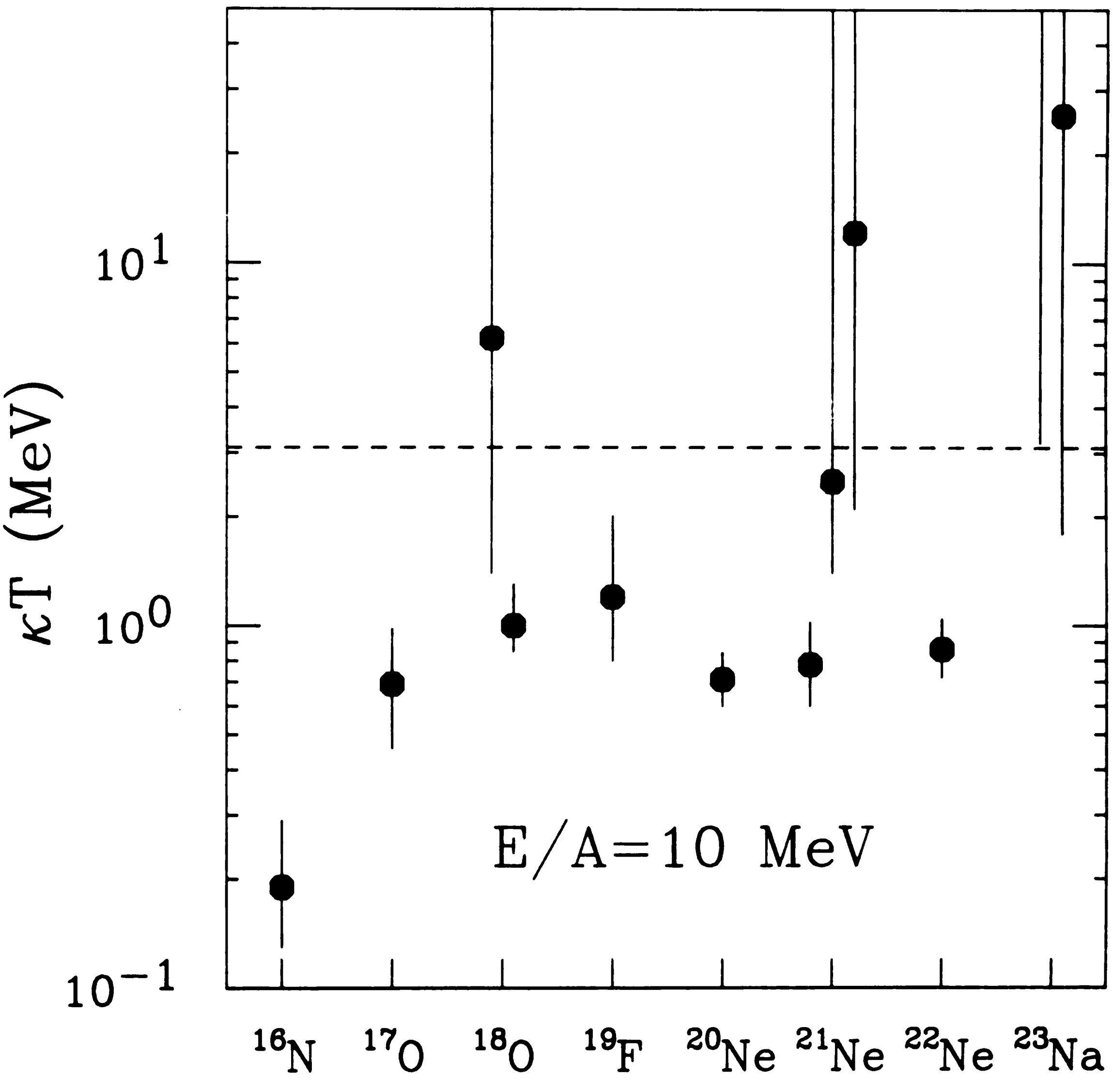

Figure IV.4.3 (cont'd.) b) At E/A=10 MeV.

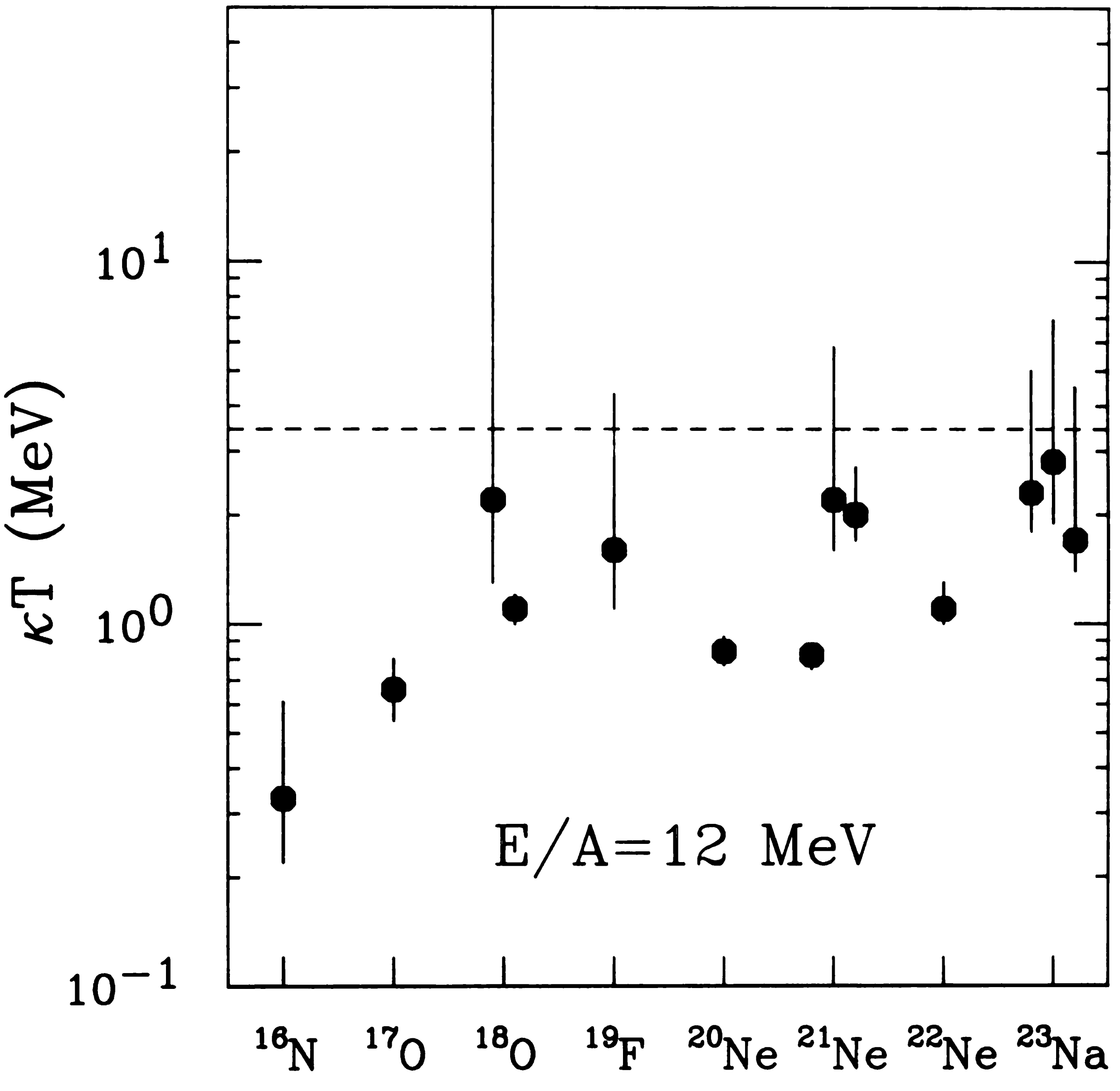

Figure IV.4.3 (cont'd.) c) At E/A=12 MeV.

Table IV.4.1 Deduced nuclear temperatures from intermediate fragments.
a) At E/A=8 MeV.

E/A (MeV)	Isotope	E_γ (KeV)	Decay	f_C a)	N_γ	f	κT (MeV)
8	^{16}N	276	0.40→0.12				
		+297	0.30→g.s.	0.551	92±23	0.389±0.097	$0.36^{+0.38}_{-0.13}$
	^{17}O	871	0.87→g.s.	0.221	61±26	0.094±0.040	$0.72^{+0.29}_{-0.23}$
	^{18}O	1650	3.63→1.98				
		+1571	3.55→1.98	0.307	63±31	0.371±0.183	$1.2<\kappa T<\infty$
		1937	3.92→1.98				
		+1982	1.98→g.s.	0.979	115±20	0.850±0.148	$1.5^{+\infty}_{-0.4}$
	^{19}F	1236	1.35→0.11	0.218	85±18	0.229±0.048	$3.8^{+\infty}_{-2.3}$
	^{20}Ne	1634	1.63→g.s.	0.765	78±17	0.735±0.160	$2.0^{+\infty}_{-0.9}$
	^{21}Ne	351	0.35→g.s.	0.744	420±35	0.694±0.058	$1.6^{+1.7}_{-0.4}$
		1120	2.87→1.75	0.116	32±14	0.126±0.055	$4.1^{+\infty}_{-2.7}$
		1395	1.75→0.35	0.337	51±18	0.248±0.088	$1.4^{+1.3}_{-0.4}$
	^{22}Ne	1275	1.28→g.s.	0.908	116±25	0.750±0.162	$1.2^{+1.8}_{-0.3}$

a. Predicted gamma-fraction. See the text for the detail.

Table IV.4.1 (cont'd.) b) At E/A=10 MeV.

E/A (MeV)	Isotope	E_γ (KeV)	Decay	f_C a)	N_γ	f	κT (MeV)
10	^{16}N	276	0.40→0.12				
		+297	0.30→g.s.	0.554	55±26	0.233±0.111	$0.19^{+0.10}_{-0.06}$
	^{17}O	871	0.87→g.s.	0.226	57±26	0.089±0.041	$0.69^{+0.29}_{-0.23}$
	^{18}O	1650	3.63→1.98				
		+1571	3.55→1.98	0.311	53±15	0.330±0.093	$6.2^{+\infty}_{-4.8}$
		1937	3.92→1.98				
		+1982	1.98→g.s.	0.986	80±18	0.626±0.141	$1.0^{+0.3}_{-0.1}$
	^{19}F	1236	1.35→0.11	0.222	63±20	0.153±0.049	$1.2^{+0.8}_{-0.4}$
	^{20}Ne	1634	1.63→g.s.	0.771	82±22	0.345±0.092	$0.71^{+0.13}_{-0.11}$
	^{21}Ne	351	0.35→g.s.	0.748	656±73	0.549±0.061	$0.78^{+0.24}_{-0.18}$
		1120	2.87→1.75	0.119	57±20	0.113±0.040	$2.5^{+\infty}_{-1.1}$
		1395	1.75→0.35	0.344	155±28	0.382±0.069	$12.1^{+\infty}_{-10.0}$
	^{22}Ne	1275	1.28→g.s.	0.913	185±30	0.585±0.095	$0.86^{+0.18}_{-0.14}$
	^{23}Na	440	0.44→g.s.	0.651	295±29	0.724±0.071	$3.2<\kappa T<\infty$
		628	2.70→2.08	0.086	34±13	0.106±0.040	$25.5^{+\infty}_{-23.7}$

a) Predicted gamma-fraction. See the text for the detail.

Table IV.4.1 (cont'd.) c) At E/A=12 MeV.

E/A (MeV)	Isotope	E_γ (KeV)	Decay	f_C a)	N_γ	f	κT (MeV)
12	^{16}N	276	0.40→0.12				
		+297	0.30→g.s.	0.556	268±70	0.370±0.096	$0.33^{+0.28}_{-0.11}$
	^{17}O	871	0.87→g.s.	0.230	175±43	0.085±0.020	$0.66^{+0.14}_{-0.12}$
	^{18}O	1650	3.63→1.98				
		+1571	3.55→1.98	0.316	172±43	0.293±0.073	$2.2^{+\infty}_{-0.9}$
		1937	3.92→1.98				
		1937	3.92→1.98				
		+1982	1.98→g.s.	0.991	311±33	0.665±0.071	1.1±0.1
	^{19}F	1236	1.35→0.11	0.226	277±68	0.186±0.045	$1.6^{+2.7}_{-0.5}$
	^{20}Ne	1634	1.63→g.s.	0.776	422±46	0.437±0.048	$0.84^{+0.08}_{-0.07}$
	^{21}Ne	351	0.35→g.s.	0.753	2917±99	0.561±0.019	0.82±0.07
		1120	2.87→1.75	0.122	234±50	0.107±0.023	$2.2^{+3.6}_{-0.6}$
		1395	1.75→0.35	0.350	543±50	0.308±0.028	$2.0^{+0.7}_{-0.3}$
	^{22}Ne	1275	1.28→g.s.	0.918	980±73	0.709±0.053	$1.1^{+0.2}_{-0.1}$
	^{23}Na	440	0.44→g.s.	0.654	2430±90	0.637±0.024	$2.3^{+2.7}_{-0.5}$
		628	2.70→2.08	0.088	249±47	0.083±0.016	$2.8^{+4.1}_{-0.9}$
		1774	3.85→2.08				
		+1636	2.08→0.44	0.297	337±55	0.258±0.42	$1.7^{+2.8}_{-0.3}$

a) Predicted gamma-fraction. See the text for the detail.

The overall result shows that the observed gamma-fractions at E/A=8 MeV are, in most cases, larger than those at E/A=10 and 12 MeV. The low gamma-fractions observed at E/A=10 MeV are somewhat contradictory to the result from light fragments, while the lower values at E/A=12 MeV show a consistency with the results in the preceding section. ^{16}N and ^{17}O may be regarded as two of the best probes among those under consideration in a study of the population distribution of intermediate fragments since these have only three bound excited states, and the feedings from the unbound states are experimentally well known to be negligible. However the temperatures observed from these two nuclei are surprisingly lower than those from the other nuclei at all the beam energies. If one assumes that these fragments are produced from a thermally equilibrated composite system, the lower temperature for ^{16}N and ^{17}O can be explained either by the possibility that there exist a number of experimentally unknown high-spin states which exclusively decay into the ground state through the gamma-ray emission, or by the preferential feeding to the ground state from the particle unbound states in higher-A nuclei system [Ha88, Ha87, Mo85a, Mo84a, St83].

Feedings to the bound states by particle decay of higher-A nuclear unbound states are calculated by the quantum statistical model [St83, Ha87, Ha88] as modified by Fields et al. [Fi87]. In the modified quantum statistical model, it is assumed that the primary populations depend on the temperature, binding energies, spins, and Coulomb barriers. Figures IV.4.4(a-b) show the comparisons between the data and the calculated values for some of complex fragments. Solid lines represent the gamma-fractions calculated from the primary population distribution, dashed lines show those from the modified quantum statistical model [Fi87]. It is shown by this model that an appreciable effect due to the feeding from the unbound states in the higher-A nuclear systems on the gamma-fractions exists at the temperatures expected for the present beam energies. Especially, the much lower gamma-fractions measured for ^{7}Li and ^{7}Be at E/A=12 MeV may be significantly due to this effect, as shown in Figure IV.4.4a. According to the model employed here, at temperatures above 2-3 MeV the gamma-fractions for the gamma-ray transitions in ^{7}Li and ^{7}Be will decrease as the temperature gets higher because of the preferential feeding to the ground states. The lower temperatures observed in the reaction of ^{14}N + ^{12}C with E/A≥12 MeV [Mo86a] may have been due to this effect, too. For ^{14}N, a preferential feeding to the isomeric high-spin state, 0.297(3^-), is predicted by the quantum statistical model [St83, Fi87], hence leading to overall lower temperatures for this nucleus which are as yet unexplained. For ^{17}O, feedings to the high-spin states, 3.841($\frac{5}{2}^-$) and 0($\frac{5}{2}^-$), are predicted to be much larger than those to the low spin states, 3.055($\frac{1}{2}^-$) and 0.871($\frac{1}{2}^-$), which means that the gamma-fraction of E_γ=871 KeV transition after the preferential decays to the high-spin states will differ significantly from that calculated from the primary populations. This prediction agrees well with the data, which is shown in Figure IV.4.4b for ^{17}O. As many more excited states get involved in the measured and calculated gamma-fractions for fragments heavier than ^{17}O, the preferential feedings to certain states may not play an important role for the gamma-fraction; in other words, the gamma-fraction predicted after the preferential decays may not be significantly different from that calculated from the primary population distributions only. An example is shown in Figure IV.4.4b for ^{18}O. The calculated gamma-fractions before and after the preferential feedings are only slightly different from each other for both E_γ=1982 KeV and 1571 KeV transitions in ^{18}O.

The quantitative discussion of the preferential-decay effect on the final population distributions may not be feasible without more detailed knowledge of the primary population distributions. However, since direct measurements of the primary populations are not available, the underlying physics of this discussion must be confined to the qualitative predictions. The final population distributions predicted by the modified quantum statistical model [Fi87] are compared with the experimental data in Figure IV.4.5. The solid lines in this figure represent the predicted cross sections at each beam energy, and these are normalized to ^{10}B. The results of the model are presented only up to the oxygen isotopes, but isotopes up to A=21 were included in the code. Since angular distributions were not obtained in the experiment, they were calculated according to Ref. Mo75. The angle for the peak velocity in the center-of-mass frame (ranging from 29° to 48°), which was calculated by transformation of the laboratory angle with the peak velocity, has been used in the calculation of the total cross section for each nucleus. In Figure IV.4.5, it is shown that the prediction reproduces the relative cross sections reasonably well over the mass range under consideration. Lower observed cross sections for the lithium isotopes (obtained only for E/A=8 MeV) may be due to the uncertainty arising from punch-through problems in the detection of the fast-moving light fragments. The agreement of the cross sections between the experimental and that predicted for ^{12}C implies that the

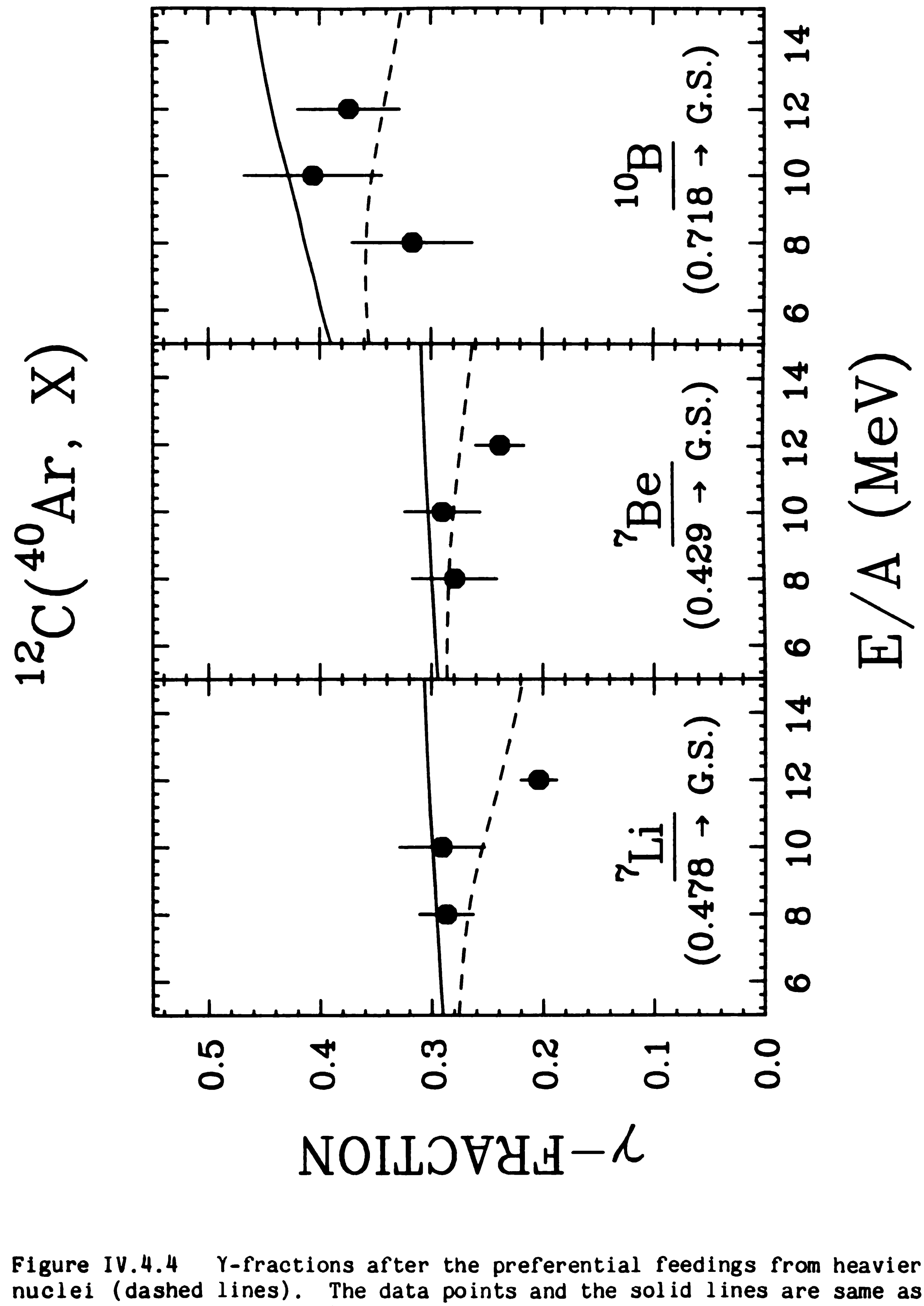

Figure IV.4.4 Y-fractions after the preferential feedings from heavier nuclei (dashed lines). The data points and the solid lines are same as in Figures IV.3.2 and IV.4.2. a) For light fragments.

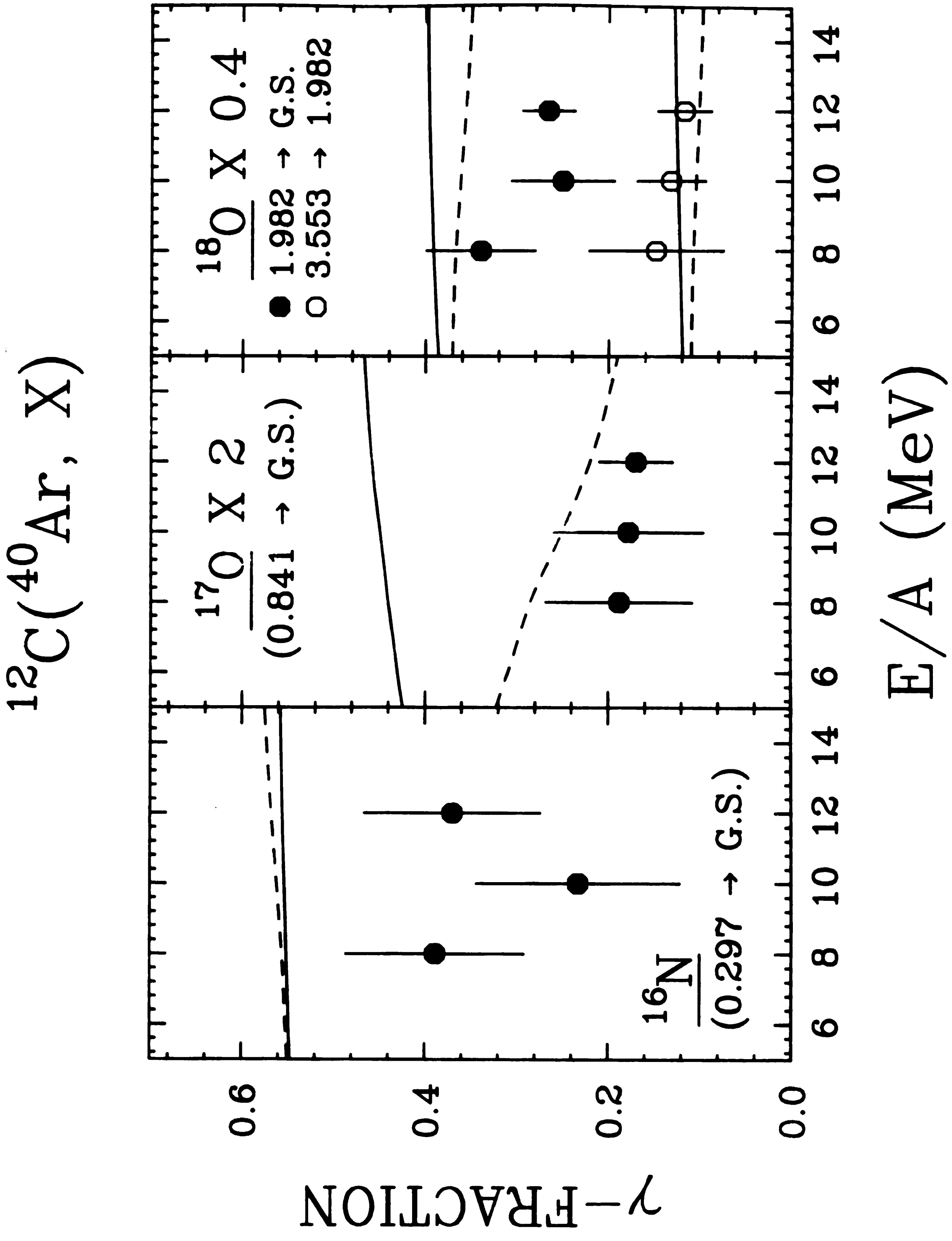

Figure IV.4.4 (cont'd.) b) For intermediate fragments.

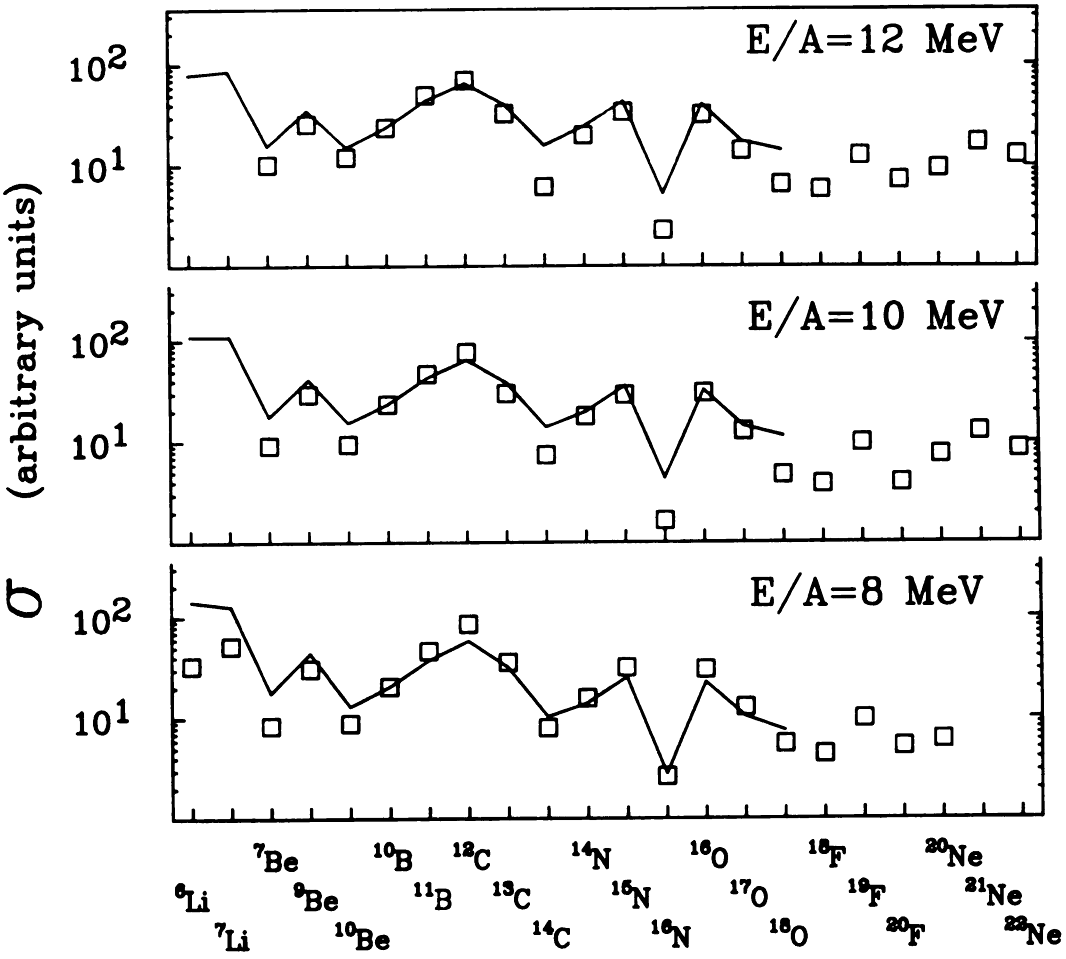

Figure IV.4.5 Cross sections for complex fragments. Solid lines represent the predicted cross sections by the quantum statistical model [St83, Fi86].

contribution from the target-like moving source [Ch86a, Ch87a, Ch87b] is not important in the formation of fragments in this mass region for the present reaction.

In conclusion, the observed population distributions of the nuclear states in the light fragmentation region (Li, Be, and B) at E/A=8 and 10 MeV are in a rough agreement with the predicted values under the assumption of the simple thermal equilibrium, which indicates little effect of the preferential feedings from the higher-A nuclear unbound states on the population distributions at these low bombarding energies. However, the data for the light fragments at E/A=12 MeV and those for the intermediate fragments at all the energies show fluctuations in the observed temperatures. This can be interpreted to mean that the variable feedings from the higher-A nuclear systems play an important role in the formation of the nuclear states along with the primary population of each nuclear state, however the data shows also that the quantum statistical model may have overestimated the the feedings for certain states in certain nuclei. The variation in the feeding from one type of fragment to another must depend on the nuclear structure characteristic of the higher-A nuclei especially for the very high-lying unbound states. This ought to be also associated with the temperature and the decay channel of the composite system [So83, St83, So84, Mc85, Fi87, Ha87, Ha88]. Hence this leads to the idea that the low temperatures observed for ^{7}Li and ^{7}Be at E/A=12 MeV may not imply the failure of equilibrium at this beam energy. A calculation with the quantum statistical model [Ha88, Ha87, Fi87, St83] supports this statement qualitatively by explaining that the lower temperatures than those predicted for some nuclei, for example, ^{17}O, may be due to the significant amount of preferential feeding to the ground state. In no beam energy for this mass region, there was any indication of the yrast-line dominant gamma-ray emission, which is most common in the residual heavy fragments. An indication of consistency with thermal equilibration at E/A=12 MeV is somewhat different from the result in Ref. Mo86a, however this may be studied further by increasing the bombarding energy and also observing the gamma-transitions from the higher-lying states. As a reliable prediction of the primary population is an essential factor in the quantum statistical model [St83, Fi87], a more realistic formulation is required in the calculation of the primary population distributions, for example, the inclusion of the fission-fragment yield dependence on the maximum angular momentum of the compound nucleus [So84].

IV.5 Errors

The errors involved in the evaluation of the gamma-fractions (or temperatures) are due to statistical uncertainties and systematic errors. The systematic errors are primarily due to the uncertainty in determining the gamma-ray detector efficiency, which are estimated in total to be about 5% for NaI(Tl) scintillation detectors and 2% for Ge counters. The statistical uncertainties are due to the least-square fitting procedure of a Gaussian function plus background. A typical example of the fitting is shown in Figure IV.5.1 for the case of ^{20}Ne. The solid lines represent the Gaussian-function fittings with the backgrounds, which were fitted by a second order polynomial function. Errors evaluated by this procedure turned out to be larger than, or comparable to, those calculated by the standard way according to $\Delta N_\gamma = \sqrt{N_\gamma + 2N_B}$, where N_γ is the number of counts in the peak area with the background subtracted and N_B is the summed area of the background (area between the dashed lines in Figure IV.5.1). Possible errors for gamma-rays emitted from the long-lived states must be taken into account because of the effect on the geometrical efficiency and the Doppler broadening. For example, an error of 10% was estimated for the gamma-ray of 718 KeV for ^{10}B.

The net error in determining the number of counts for each gamma-ray peak was obtained by taking the square-root of the sum of the squares of the individual errors. This gives the results shown in Tables IV.3.1 and IV.4.1. As the statistics are limited substantially at E/A=8 and 10 MeV for the intermediate fragments, the statistical errors dominate the net errors in those cases.

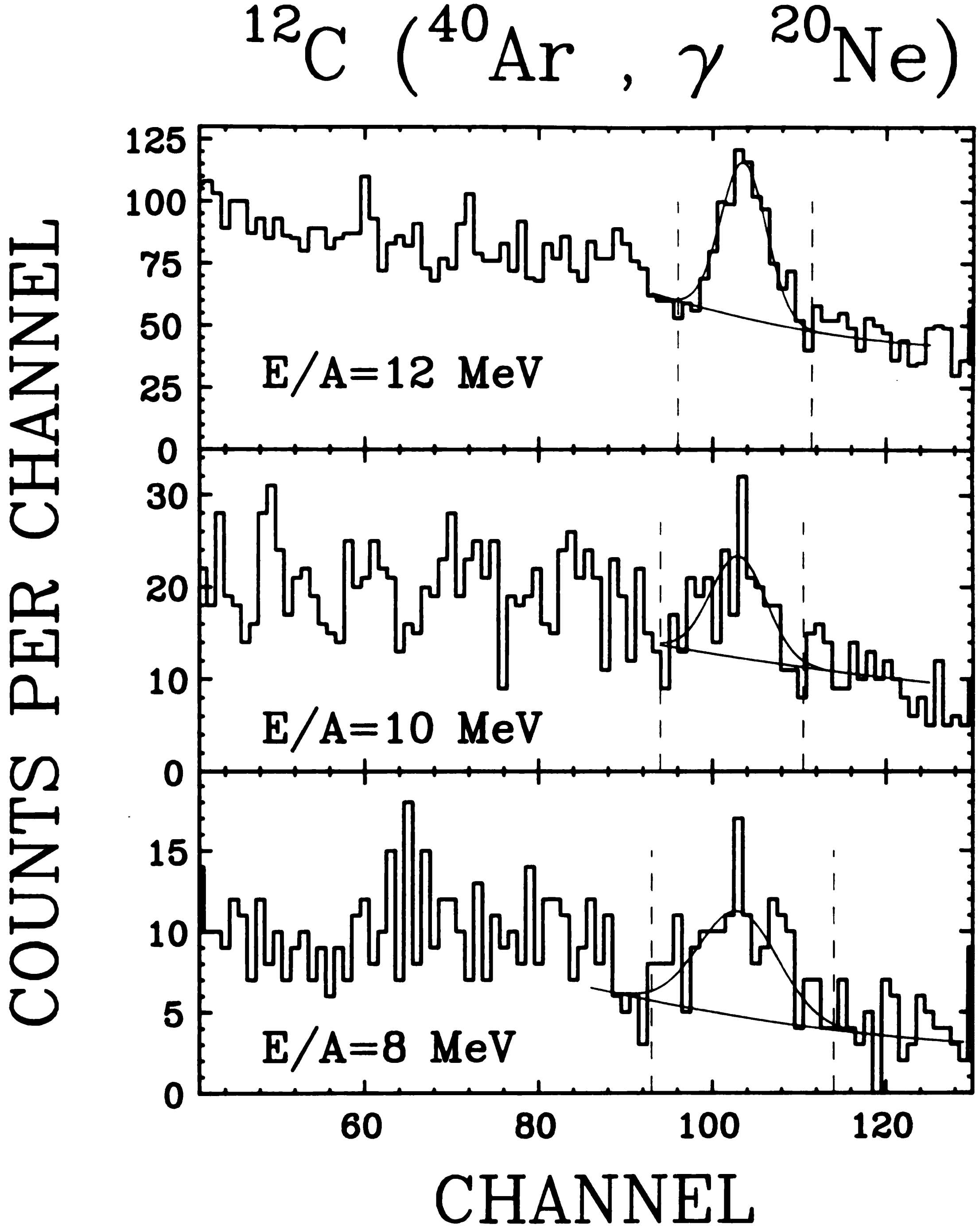

Figure IV.5.1 An example of the γ-ray peak fittings for ^{20}Ne. See the text for detail.

CHAPTER V: POPULATION DISTRIBUTION II
(HEAVY RESIDUAL FRAGMENTS)

V.1 Introduction

Continuum gamma-rays with high multiplicities have been observed previously in heavy-ion reactions [e.g., Ne77, Ha75, Si76, Ne75]. A study of the energy spectra [Ne77] of these gamma-rays showed that the multiplicity spectra have peaks at energies around 1-3 MeV, and these gamma-rays have been interpreted to be associated with the "yrast and statistical cascade" [Ne77].

It is well known that, in reactions well above the Coulomb barrier, the compound nucleus is formed with relatively high angular momentum and high excitation energy. The overall decay of this excited compound nucleus includes strong contributions from the emission of light particles, such as neutron, proton, and alpha-particle emission, and fission competition becomes important for the decay of the compound nucleus with high angular momentum. However, since light particle evaporation removes a relatively small amount of angular momentum, the decay of the composite system is heavily influenced by the yrast line. The emission of light particles will, in general, continue until the system eventually cools down to the point at which gamma-ray emission starts. The primary population distributions of nuclear states in the heavy residual fragment region, therefore, may be governed by the maximum angular momentum involved in the entrance channel, fission of the compound nucleus to produce sizable complex fragments, and the competition between light particle evaporation and gamma-ray emission.

Information about the population distributions of the bound states can be obtained from gamma-ray emission, as shown Ch. IV. Under the assumption of complete fusion, the emission of gamma-rays observed in coincidence with the heavy residual fragments should reflect the dependence on the statistical decay-chain which is associated with the excitation energy and spin, the shape of the yrast line, and the dinuclear dynamics in the entrance channel; but not on the Boltzmann distribution which prevails apparently in the production of complex fragments. It is, therefore, interesting to compare the experimentally observed intensity of gamma-rays from the heaviest fragments with those predicted by the statistical model [Pü77] in order to study a fundamental aspect of the formation of the composite system.

In the present reaction, if a compound nucleus was formed, the excitation energy would be about 92 MeV at E/A=8 MeV, 113 MeV at E/A=10 MeV, and 131 MeV at E/A=12 MeV. These values are sufficient to evaporate a number of nucleons or alpha-particles, and as a consequence, the residual fragments will be deflected from the original beam direction due to the recoil of the emitted particles. Hence, by employing reverse kinematics, which provides a large laboratory energy for the center-of-mass frame, and by placing the particle detectors at small angles relative to the beam direction, the evaporation residues can be detected. This also enables the measurement of gamma-ray emission in coincidence with these fragments, and therefore the population distribution of the particle-stable-excited states. Although the individual isotope separation is not available, the clear Z-identification of the heavy residual fragments in the particle telescopes, which is shown in Figures III.1.3(a-c), is essential for this measurement.

V.2 Statistical Model

The CASCADE nuclear evaporation code [Pü77], as modified by Harakeh for low energy heavy-ion reactions, predicts the population distribution of the evaporation residues, and is based on the statistical theory for compound-nucleus reactions (Hauser-Feshbach theory). This model assumes that projectile and target form a compound nucleus in statistical equilibrium, and then the compound nucleus decays by emission of light particles (alpha-particle, proton, or neutron). Hauser-Feshbach formulas are applied in this model in order to calculate the intensities of the various decay modes of the compound nucleus. Fission has been neglected in the decay mode of the compound nucleus in this model, however an effort to take it into account is made by cutting off the highest partial waves in the compound nucleus. No estimation for pre-equilibrium emission is made in this model.

Following Ref. Pü77, the cross section for the formation of the compound nuclei from projectile and target nuclei with zero spin and even parity for both, which is relevant to the present reaction, is given by

$$\sigma_{CN} \propto \sum_{\ell,\pi} (2\ell+1)\, T_{\ell}(E) \;, \quad (V.1)$$

where ℓ represents the spin of the compound nucleus, and E is a center-of-mass energy. The summation over spin ℓ is restricted by the parity selection rule $\pi = \pi_P \pi_T (-1)^\ell = (-1)^\ell$, where π_P and π_T represent parities for projectile and target nucleus, respectively. The transmission coefficients $T_\ell(E)$ are approximated by a Fermi distribution [Pü77]

$$T_\ell = \frac{1}{1 + \exp[(\ell - \ell_0)/d]} , \quad (V.2)$$

where ℓ_0 corresponds to the critical or maximum angular momentum for fusion, whichever is smaller, and the diffuseness d is responsible for cutting off a portion of the highest partial waves.

The decay width for emitting a particle x from an excited nucleus of excitation energy E_1, spin J_1, and parity π_1 to form a product nucleus of E_2, J_2, and π_2 is given by [Pü77]

$$\Gamma_x(\varepsilon_x) = \frac{\rho_2(E_2, J_2, \pi_2)}{2\pi \rho_1(E_1, J_1, \pi_1)} \sum_{S=|J_2 - s_x|}^{J_2 + s_x} \sum_{L=|J_1 - S|}^{[\pi]} T_L^x(\varepsilon_x) , \quad (V.3)$$

where ε_x represents the kinetic energy of particle x (equal to $E_1 - E_2 -$ separation energy), ρ_i $(i=1,2)$ is the level density, s_x and L are the spin and the orbital angular momentum of particle x, respectively, and the channel spin $S = J_2 + s_x$. Again, the summation over L is limited by the parity selection rule, and the transmission coefficients T_L^x are obtained from the optical model.

An analytical form of the Fermi gas level density is applied in the very high excitation energy region (liquid-drop region), while in the low energy region, either the experimentally known levels or the analytical formulas can be used. The yrast line is calculated as [Pü77]

$$E_{rot}(J) = \frac{J(J+1)\hbar^2}{2I} + \Delta \ , \quad (V.4)$$

where I represents the moment of inertia, and Δ is a pairing energy which determines the zero point of the effective excitation energy. The appropriate input of the moment of inertia comprises a crucial point of the calculation for the population near the yrast line. A careful study of the experimentally known high-spin states was carried out in the current calculation to obtain a proper shape of the yrast line for each nucleus. The density parameter (a), pairing energy (Δ) in Eq. V.4, and the fraction of the moment of inertia relative to the rigid body (I/I_0) used as the input parameters for the calculation are given in Table V.2.1.

In the evaluation of the gamma-ray intensities, the experimentally known level information, including the gamma-branching ratios, has been used for the low-lying states. For the very high-lying states about which little is known, the model calculates the gamma-decay rate $R_\gamma d\varepsilon_\gamma$ from a state (excitation E_1, spin J_1, parity π_1) to another state (E_2, J_2, π_2) according to a formula [Pü77],

$$\Gamma_\gamma(\varepsilon_\gamma) = \frac{\rho(E_2,J_2,\pi_2)}{2\pi\rho(E_1,J_1,\pi_1)} \sum_L \xi_L f_L(\varepsilon_\gamma) \ , \quad (V.5)$$

where ρ represent the density of states, L denotes the multipolarity of the gamma-ray, and $\xi_L f_L(\varepsilon_\gamma)$ are energy dependent strengths. Only E1, M1, and E2 transitions are considered in this model.

The maximum angular momentum ℓ_{max}=39 $\hbar$, which is obtained with r_{max} = $1.2(A^{1/3}+A_2^{1/3})$ fm, is used in the CASCADE code calculation in order to reproduce the mass distribution spectra better than with ℓ_{cr}=32 $\hbar$ [Wi80, Mo86b]. Although the proper use of the maximum angular momentum is critical in the mass distribution spectra, it was found that the relative gamma-ray intensities for the transition along near the yrast line are not very sensitive to ℓ_{max}. As a matter of fact, it was found that the broad shape of the predicted primary population distribution (or the relative population densities of nuclear states) in a spin-excitation energy space depends mainly on the function of the excitation energy range in the decay array, even though the yrast line concentration prevails in most cases. A couple of examples of the calculation are shown in Figures V.2.1(a-b) for ^{42}Ca and ^{38}Ar. Thick solid line represents the yrast line. Competition between nucleons, alpha-particle, and gamma-ray are also shown in the figures (upper dotted line denote partial nucleon decay width of 50% and lower line denote partial gamma-ray decay width of 50%). Thin solid lines drawn in the figures represent the shape of the primary population distributions. The unit used in the population-density grid is $\frac{mb}{MeV\bullet\hbar}$. Dotted lines divide the spin-excitation energy space into the gamma-ray decaying region, alpha-particle decaying region, and nucleon decaying region according to the decay probabilities as in Eqs. V.3 and V.5. Yrast-line dominance in the population distribution can be seen in the figure for both the nuclei. However, one should note that the population along the yrast line is rather sensitive to the moment of inertia, as mentioned earlier.

Table V.2.1 Input parameters for CASCADE calculation

Charge	Mass	a	Δ	I/I_0
24	52	8.83	2.64	1.1
24	51	8.48	0.29	1.1
24	50	8.24	1.73	1.1
24	49	8.09	-0.31	1.1
24	48	8.00	1.38	1.1
23	51	8.97	0.77	1.1
23	50	8.59	-1.04	1.1
23	49	8.35	-0.18	1.1
23	48	8.20	-1.65	1.1
23	47	8.10	-0.57	1.1
23	46	8.21	-1.92	1.0
22	50	9.12	2.51	1.0
22	49	8.73	0.12	1.0
22	48	8.47	1.60	1.0
22	47	8.31	-0.48	1.0
22	46	8.22	1.25	1.1
22	45	8.34	-0.74	1.1
22	44	8.97	1.62	1.0
21	49	9.27	0.65	1.0
21	48	8.86	-1.16	1.1
21	47	8.60	-0.30	1.1
21	46	8.43	-1.78	1.0
21	45	8.33	-0.69	1.1
21	44	8.46	-3.05	1.05
21	43	8.60	-1.87	1.2
21	42	8.75	-2.19	1.1
20	46	8.72	1.55	1.0
20	45	8.55	-0.57	1.0
20	44	8.45	1.20	0.93
20	43	8.58	-0.83	1.0
20	42	8.73	1.27	1.15
20	41	8.89	-1.26	0.80
20	40	10.05	2.02	0.85
19	45	8.70	-0.37	1.0
19	43	8.43	-0.76	1.0
19	42	8.56	-2.54	0.80
19	41	8.72	-0.94	1.0
19	40	8.88	-2.29	0.90
19	39	10.54	0.17	1.0
19	38	9.03	-2.35	0.85
18	41	8.55	-0.90	0.88
18	40	8.71	1.05	0.80
18	39	8.87	-1.02	0.84
18	38	9.03	1.03	0.87
18	37	9.02	-1.07	0.83

Table V.2.1 (cont'd.)

Charge	Mass	a	Δ	I/I_0
18	36	9.52	1.55	0.85
17	39	8.70	-0.99	0.85
17	38	8.86	-2.33	0.85
17	37	9.03	-1.06	0.77
17	36	9.02	-2.39	0.78
16	37	8.86	-1.04	0.60
16	36	9.03	1.57	0.60
16	35	9.02	-1.08	0.60
16	34	9.01	1.10	0.60
16	33	9.01	-1.10	0.60
15	34	9.02	-2.42	0.60
15	33	9.01	-1.10	0.60
15	32	9.01	-2.45	0.60
14	31	9.01	-1.11	0.60
14	30	9.00	1.23	0.60

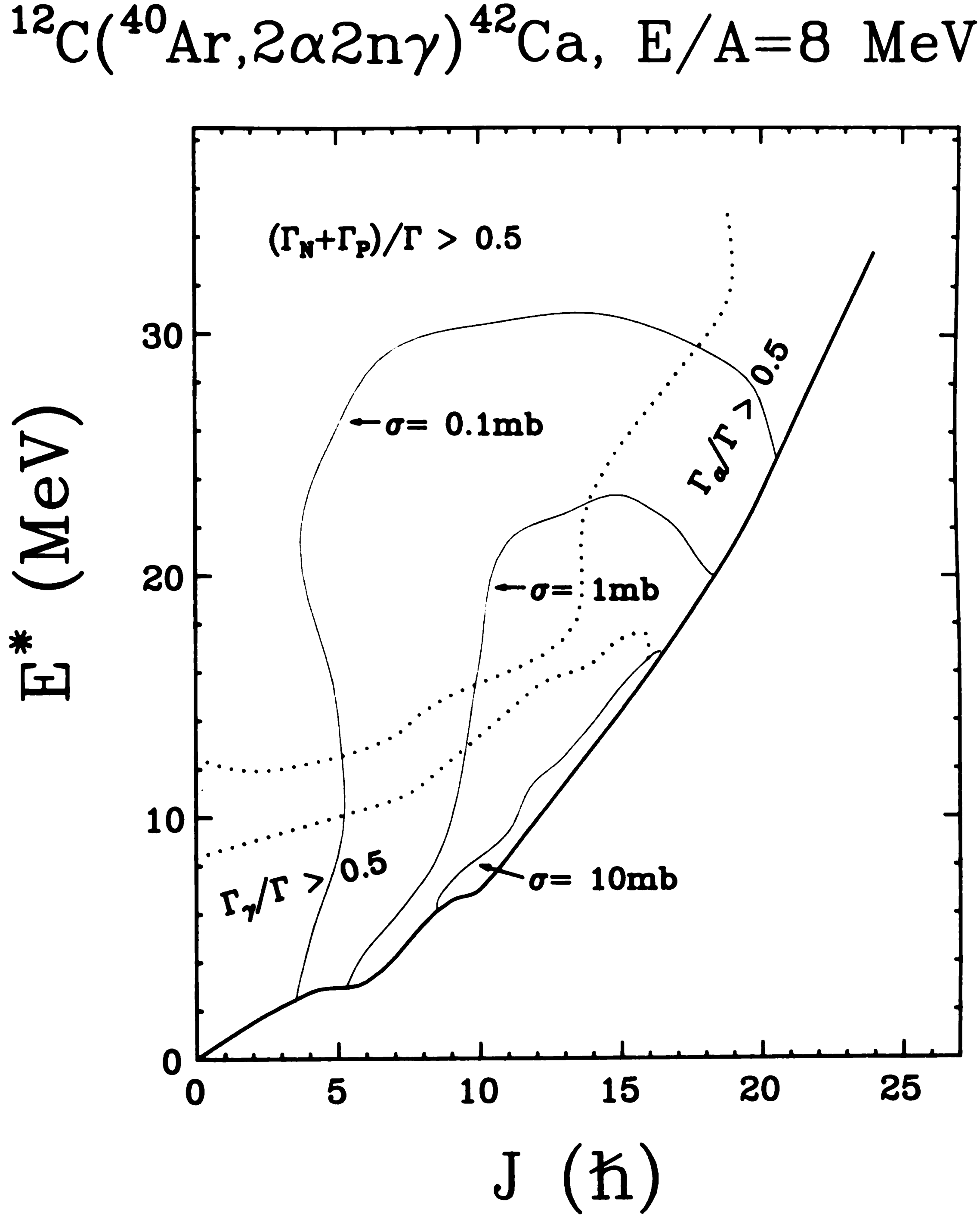

Figure V.2.1 Predicted primary population density distribution by the CASCADE code [Pü77]. See the text for detail. a) For ^{42}Ca.

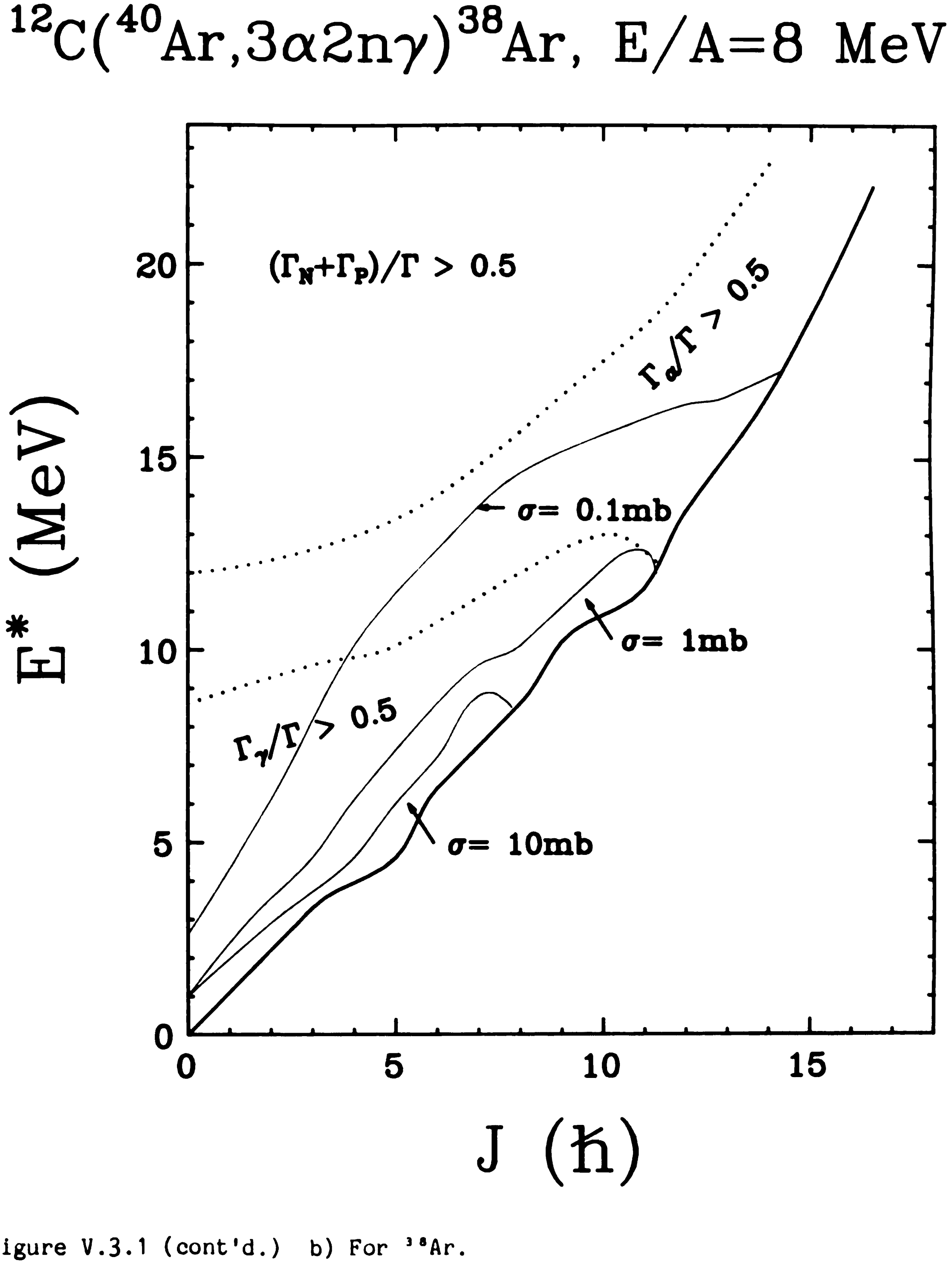

Figure V.3.1 (cont'd.) b) For ^{38}Ar.

V.3 Population of Nuclear States

Figures from V.3.1 to V.3.7 show the Doppler shift corrected gamma-ray spectra for the Ge counters in coincidence with isotopes of Ti, Sc, Ca, K, Ar, Cl, and S, respectively, at E/A=8 MeV. Gamma-ray peaks with sufficient statistics are labeled with their energies in units of KeV in these figures, where the number before the colon(:) in each label represents the mass number. Statistics at E/A=10 and 12 MeV are limited because of the limited energy range set in the Δ_2E-silicon detector. The identification of the gamma-ray peaks was carried out in a manner which was based on the experimentally known spin and excitation energy of each state and the gamma-branching ratios. Even though broad features of the gamma-ray peaks can be obtained with the NaI(Tl) scintillation detectors [Figures V.3.8(a-c) are shown as an example for K at each beam energy], one can use only the Ge counters to determine the separate gamma-ray intensities. Peaks at low gamma-ray energy appeared with a relatively good resolution, however the Doppler broadening which mainly comes from the finite geometrical shape of the gamma-ray detectors have widened the widths of peaks at higher gamma-ray energies, which makes the separation of the closely located gamma-ray peaks difficult or impossible.

Tables from V.3.1 to V.3.7 show the observed gamma-ray intensities (I_γ) at E/A=8 MeV/A. Comparison with those predicted by either the CASCADE code [Pü77], which is described in the following section, and/or the Boltzmann thermal distribution with a temperature of $\kappa T=2.76$ MeV, which is calculated for E/A=8 MeV by the Fermi gas model, is also given in the tables. The calculation of the Boltzmann distribution was carried out for some of the less heavy fragments (e.g., S, Cl), for which the statistical model [Pü77] predicts little populations, and it was done only for those nuclei which have relatively well known level information. Errors included in these tables represent the statistical uncertainties which are due to the least-square fitting procedure of the Gaussian function plus background, as discussed in Sec. IV.5. Since the total cross section of each Z is not available for the heavy residual fragments in the present experiment, and since the limited energy range also disables the determination of the relative population ratios between isotopes by means of the gamma-ray intensities (because the energy range for each isotope with the same Z will differ), the comparison of the observed cross sections with those predicted is not practical for these fragments. A future experiment designed specifically for heavy fragments would be very useful.

The observed strong transitions for each isotope are described in the following subsections:

V.3.1 Titanium (Ti)

The strongest gamma transition for Z=22 in the present reaction is along $6.24(10^+) \rightarrow 4.90(8^+) \rightarrow 3.30(6^+) \rightarrow 2.01(4^+) \rightarrow 0.89(2^+) \rightarrow 0(0^+)$ [Ra82, Po81] with ^{46}Ti. Gamma-rays along $3.60(\frac{17}{2}^-) \rightarrow 3.02(\frac{15}{2}^-) \rightarrow 1.47(\frac{11}{2}^-) \rightarrow 0(\frac{7}{2}^-)$ [Fo78] and $0.74(\frac{5}{2}^-) \rightarrow 0.33(\frac{3}{2}^-) \rightarrow 0.04(\frac{3}{2}^-)$ [Ka84] are observed with ^{45}Ti. Some of the low-lying transitions in ^{47}Ti and ^{48}Ti [Wa86a] can be also seen in Figure V.3.1, however the statistics are limited.

Table V.3.1 shows the observed gamma-ray intensities in ^{45}Ti and ^{46}Ti, respectively, at E/A=8 MeV. According the CASCADE calculation [Pü77], most of the bound states in ^{46}Ti are produced by decays of two protons and four neutrons (2P4N) from the compound nucleus, ^{52}Cr, while the residual fragments of ^{45}Ti are formed through decays of an alpha-particle and three neutrons (α3N). Since the excitation-energy range of the primary population of ^{46}Ti extends only over the low energy region, the gamma-ray transitions between high-spin states depends mainly on the shape of the yrast line. On the other hand, the primary population distribution of ^{45}Ti will be scattered widely over the excitation energy region, which means that the gamma-ray intensities are sensitive to the shape of the yrast line. This is supported by the observed data; the gamma-ray intensities along the yrast line in ^{45}Ti are roughly constant (high-spin states above 5.42 MeV are not well known experimentally [Ka84]), while the transition of $6.24(10^+) \rightarrow 4.90(8^+)$ is apparently weaker than those between low-lying states.

V.3.2 Scandium (Sc)

Transitions of $3.57(11^+) \rightarrow 2.67(9^+) \rightarrow 0.97(7^+) \rightarrow 0.27(6^+)$ in ^{44}Sc [En78] and $3.69(\frac{19}{2}^-) \rightarrow 2.11(\frac{15}{2}^-) \rightarrow 1.24(\frac{11}{2}^-) \rightarrow 0(\frac{7}{2}^-)$ in ^{45}Sc [Le78] are observed. The state of $0.27(6^+)$ MeV in ^{44}Sc is an isomeric state with $\tau_{1/2}$=2.44 days, hence the transition of this state to the ground state could not be observed in the present experiment.

Fragments of ^{45}Sc are predicted to be produced by decays of αP2N from the compound nucleus and ^{44}Sc by decays of αP3N according to the statistical model [Pü77]. The excitation range for both the nuclei extends over from the low energy to the intermediate energy region. The observed gamma-ray intensities for these nuclei are shown in Table V.3.2. Data for ^{45}Sc indicate a fair agreement with the prediction, although the prediction shows no enhancement for the population of the 1.24 ($\frac{11}{2}^-$) MeV state while a larger population of this state or a large feeding to this state from states inside the yrast line is indicated by the data. The isomeric (or high-spin) character of the $3.57(11^+)$ MeV state in ^{44}Sc leads to the prediction of a large population for this state. Although the uncertain spin assignments for the 4.11 and 3.98 MeV states limit the comparison to only the low-lying transitions, a rough agreement between the predicted and the observed gamma-ray intensities is provided for ^{44}Sc.

V.3.3 Calcium (Ca)

The strongest transition line of those observed for $Z=20$ is along $7.75(11^-) \rightarrow 7.37(10^-) \rightarrow 6.55(9^-) \rightarrow 5.74(7^-) \rightarrow 4.10(5^-) \rightarrow 3.19(6^+) \rightarrow 2.75(4^+) \rightarrow 1.52(2^+) \rightarrow 0(0^+)$ in ^{42}Ca [En78, Eg78b, Ke80, He81]. A sequence of the E2 transitions along $4.72(6^+) \rightarrow 3.25(4^+) \rightarrow 1.52(2^+)$ is also observed with ^{42}Ca. The transition of $2.75(\frac{15}{2}^-) \rightarrow 1.68(\frac{11}{2}^-) \rightarrow 0(\frac{7}{2}^-)$ is the main one in ^{43}Ca and also that along $5.93(\frac{19}{2}^-) \rightarrow 5.16(\frac{17}{2}^-) \rightarrow 4.39(\frac{15}{2}^-)$ [En78, Be78, Be79] which flows down inside the yrast line is observed.

The observed gamma-ray intensities for ^{42}Ca and ^{43}Ca are compared with those predicted by the CASCADE code in Table V.3.3. Data for ^{42}Ca and ^{43}Ca show a major disagreement with the CASCADE code prediction for the transitions between states inside the yrast line, for example, E_{γ}=776 and 761 KeV in ^{43}Ca and E_{γ}=1462 and 1729 KeV in ^{42}Ca. The observed gamma-ray intensities for these transitions are comparable to those for yrast line transitions, while the predicted values are nearly negligible compared to the latter. It is also obvious that the model fails to predict the relative populations for the yrast-line states, especially in the low-lying transitions in ^{42}Ca. The model predicts larger populations than observed for the high-lying states, or smaller populations for the low-lying states. One has to remember that both the predicted and the observed gamma-ray intensities are normalized to a certain transition, hence the terms "larger" and "smaller" are relative.

Gamma-ray intensities under the assumption of a Boltzmann thermal distribution with κT=2.76 MeV are calculated by virtue of the relatively well known level information and compared with those observed for ^{42}Ca in Table V.3.3. Since the 3.19 MeV is a long-lived state with $\tau_{1/2}$=5.4 ns, a substantial decrease in the observed gamma-ray intensities from decay of that state is expected. Nevertheless, the Boltzmann distribution calculation predicts smaller populations than those observed for the high-lying states, and larger populations for the low-lying states. A rough agreement for the transitions inside the yrast line is quite remarkable. These results seem to show that statistical emission is still an important process in the population of this nucleus, however there exists a possibility that a Boltzmann distribution may also play an important role in the population of the low-lying states.

V.3.4 Potassium (K)

Gamma-rays along $2.54(7^+) \rightarrow 0.89(5^-) \rightarrow 0(4^-)$ [En78] are observed with ^{40}K. ^{41}K have two strong transition lines; $4.99(\frac{19}{2}^-) \rightarrow 4.28(\frac{15}{2}^-) \rightarrow 2.76(\frac{11}{2}^-) \rightarrow 1.29(\frac{7}{2}^-)$ and $3.90(\frac{15}{2}^+) \rightarrow 2.77(\frac{13}{2}^+) \rightarrow 2.53(\frac{11}{2}^+) \rightarrow 1.68(\frac{7}{2}^+) \rightarrow 0(\frac{3}{2}^+)$ [En78, Eg78a, Li78, St86]. The transition of the 1.29 MeV state to the ground state could not be observed because of the long half-life of $\tau_{1/2}$=7.2 ns. The transition of $4.60(9) \rightarrow 3.56(8) \rightarrow 1.95(7^+) \rightarrow 1.38(6^+) \rightarrow 0.67(5^-) \rightarrow 0.26(4^-) \rightarrow 0.11(3^-) \rightarrow 0(2^-)$ [En78, Wa75] is the strongest one for ^{42}K.

Fragments of these isotopes are at least three light particles less than the compound nucleus. For ^{40}K, decay of 2α1P3N from the compound nucleus of ^{52}Cr with the excitation energy 92 MeV will cool down the residual fragment significantly. The predicted excitation energy range of the primary population distribution for ^{40}K is from 0 to 8 MeV only, which means that the population of fragments for this nucleus will be concentrated in the very low-lying states. However the observed gamma-ray intensities for ^{40}K, which are given in Table V.3.4 along for ^{41}K and ^{42}K, show that the CASCADE prediction underestimates substantially the populations at high excitation energy region in ^{40}K. This can be interpreted to mean that the evaporation process of the compound nucleus may not be the main exit channel to produce ^{40}K. In Table V.3.4, one may also note that the CASCADE calculation overestimates the population of high-lying states and underestimates it for states inside the yrast line for the case of ^{41}K. Data for ^{42}K show a rough agreement, however the long half-life, $\tau_{1/2}$=1.1 ns, of the 0.68 MeV state complicates the overall comparison for this nucleus.

V.3.5 Argon (Ar)

Gamma-rays along $6.41(6^+) \rightarrow 4.59(5^-) \rightarrow 4.48(4^-) \rightarrow 3.81(3^-) \rightarrow 2.17(2^+) \rightarrow 0(0^+)$ [En78, Aa79] in ^{38}Ar are from the main transition, while ^{39}Ar also had a strong transition of $5.55(\frac{17}{2}^+) \rightarrow 4.54(\frac{15}{2}^+) \rightarrow 3.99(\frac{13}{2}^+) \rightarrow 2.65(\frac{11}{2}^-) \rightarrow 0(\frac{7}{2}^-)$ [En78, Wa87]. Gamma-rays in ^{40}Ar are relatively weak (E_γ=1461 KeV will be the strongest transition for ^{41}Ar), and this indicates that the quasi-elastic scattering of the projectile (^{40}Ar) is not an important process in the production of these fragments.

Data for ^{38}Ar and ^{39}Ar are given in Table V.3.5. Level information including spin, energy, and gamma-branching ratio of each state is relatively well known for ^{38}Ar, which encourages a thermal calculation for gamma-ray intensities. The rough agreement between the prediction of the CASCADE code and the observations for ^{38}Ar is somewhat surprising, while the thermal calculation with the Boltzmann distribution overestimates the populations at low-lying states. For ^{39}Ar, the statistical prediction overestimates the population of high-lying states.

V.3.6 Chlorine (Cl)

Transitions along $2.52(5^-) \rightarrow 0.79(3^+) \rightarrow 0(2^+)$ in ^{36}Cl [En78] and those along $5.27(\frac{13}{2}^-) \rightarrow 4.55(\frac{11}{2}^-) \rightarrow 4.01(\frac{9}{2}^-) \rightarrow 3.10(\frac{7}{2}^-) \rightarrow 0(\frac{7}{2}^-)$ in ^{37}Cl [En78] are observed. Also, gamma-ray of 638 KeV [$1.31(4^-) \rightarrow 0.67(5^-)$]

and 755 KeV [0.76(3^-) → 0(2^-)] were observed with ^{38}Cl, while the isomeric state, 0.67 MeV, has the half-life, $\tau_{1/2}$=715 ms [En78].

Since the CASCADE calculation predicts little cross section for the nucleus with charge equal to 17 or smaller while the experimental cross sections for those nuclei are comparable to Z=18, 19, or 20, a comparison of it with the observed values becomes less plausible. In particular, the negligible cross section predicted by the model for ^{36}Cl disagrees with the data directly, and this encourages a calculation of the thermal population distribution. This could be done because of the large amount of information on the levels and gamma-branching ratios that exist for this nucleus. The calculated gamma-ray intensities from the CASCADE code are compared with those observed for ^{37}Cl. The results are shown in Table V.3.6. The same argument made for ^{42}Ca can be applied to these nuclei; there is an overestimation of the populations at high-lying states by the CASCADE code calculation and an underestimation by the Boltzmann thermal calculation.

V.3.7 Sulfur (S)

Transitions of 1.97($\frac{5}{2}^+$) → 0($\frac{3}{2}^+$) and 0.84($\frac{1}{2}^+$) → 0($\frac{3}{2}^+$) are observed with ^{33}S [En78, Ra85]. 5.69(5^-) → 4.62(3^-) → 3.30(2^+) → 2.13(2^+) → 0(0^+) in ^{34}S [En78, Ra85] is the strongest gamma-ray sequence in this isotope.

Table V.3.7 shows results for ^{33}S and ^{34}S. A comparison with the thermal calculation is carried out for both nuclei in this table. Even though there exist uncertainties which arise from the limited level

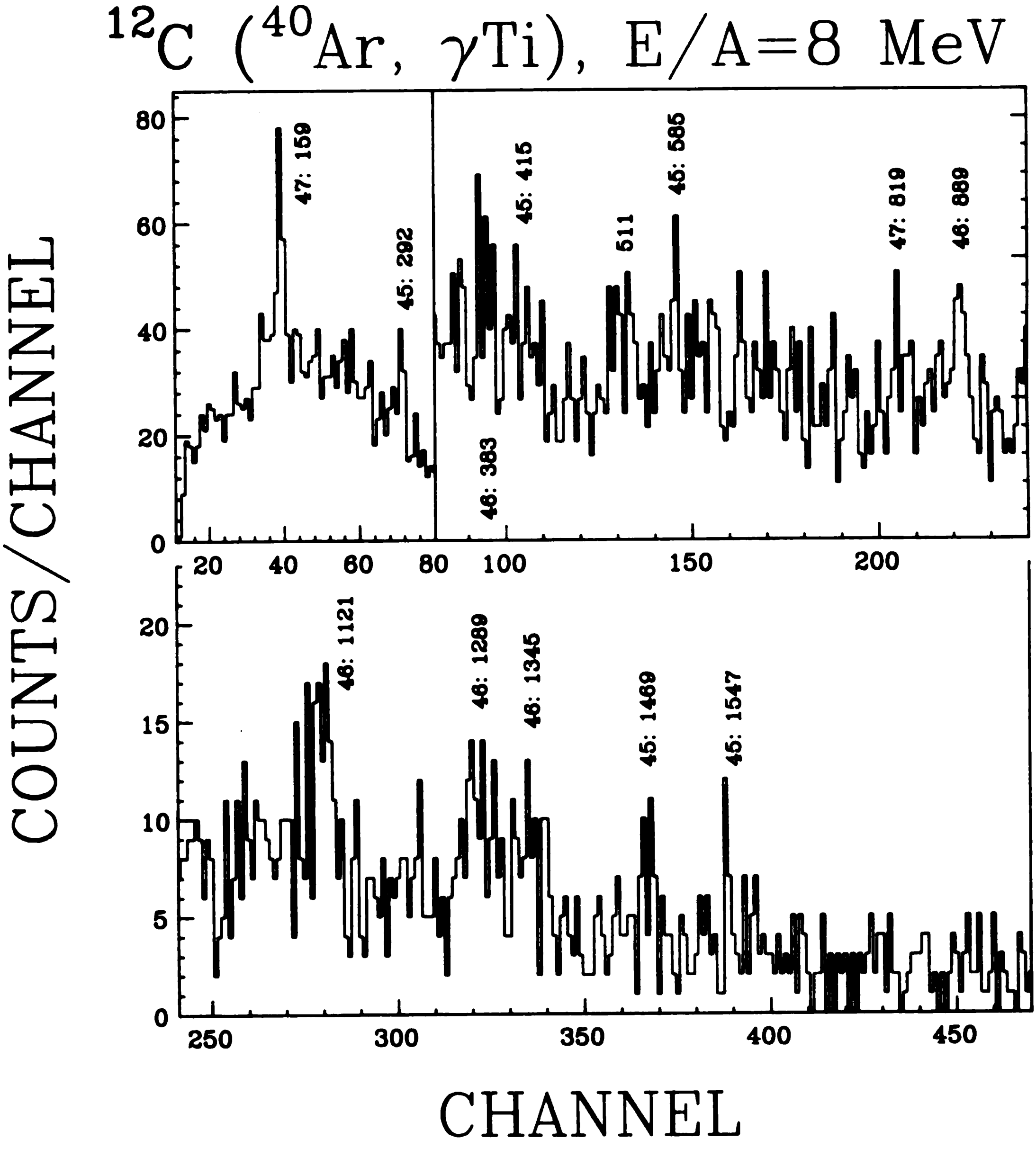

Figure V.3.1 Doppler-shift corrected Y-ray energy spectra (Ge) in coincidence with Titanium (Ti).

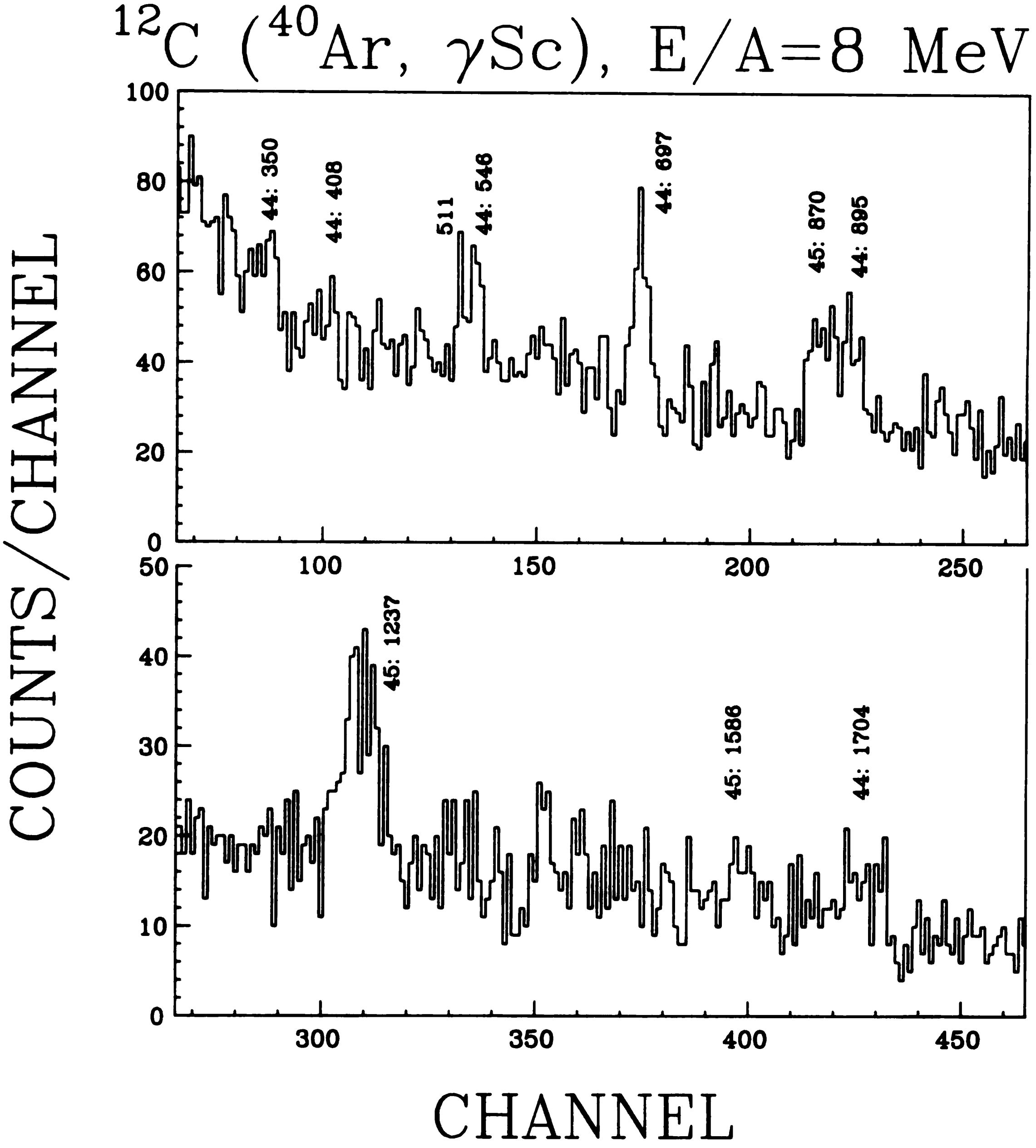

Figure V.3.2 Same as in Figure V.3.1 with Scandium (Sc).

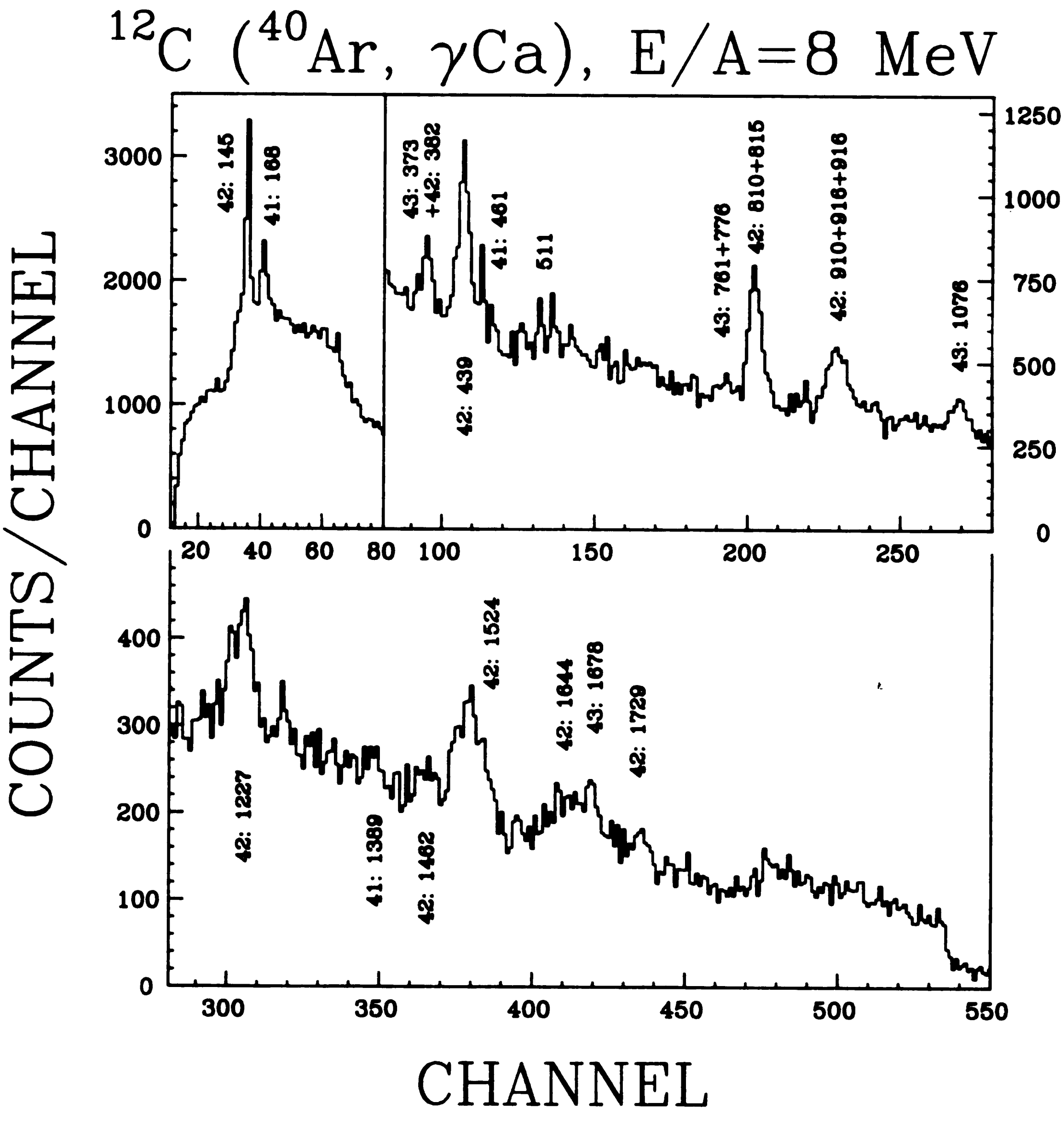

Figure V.3.3 Same as in Figure V.3.1 with Calcium (Ca).

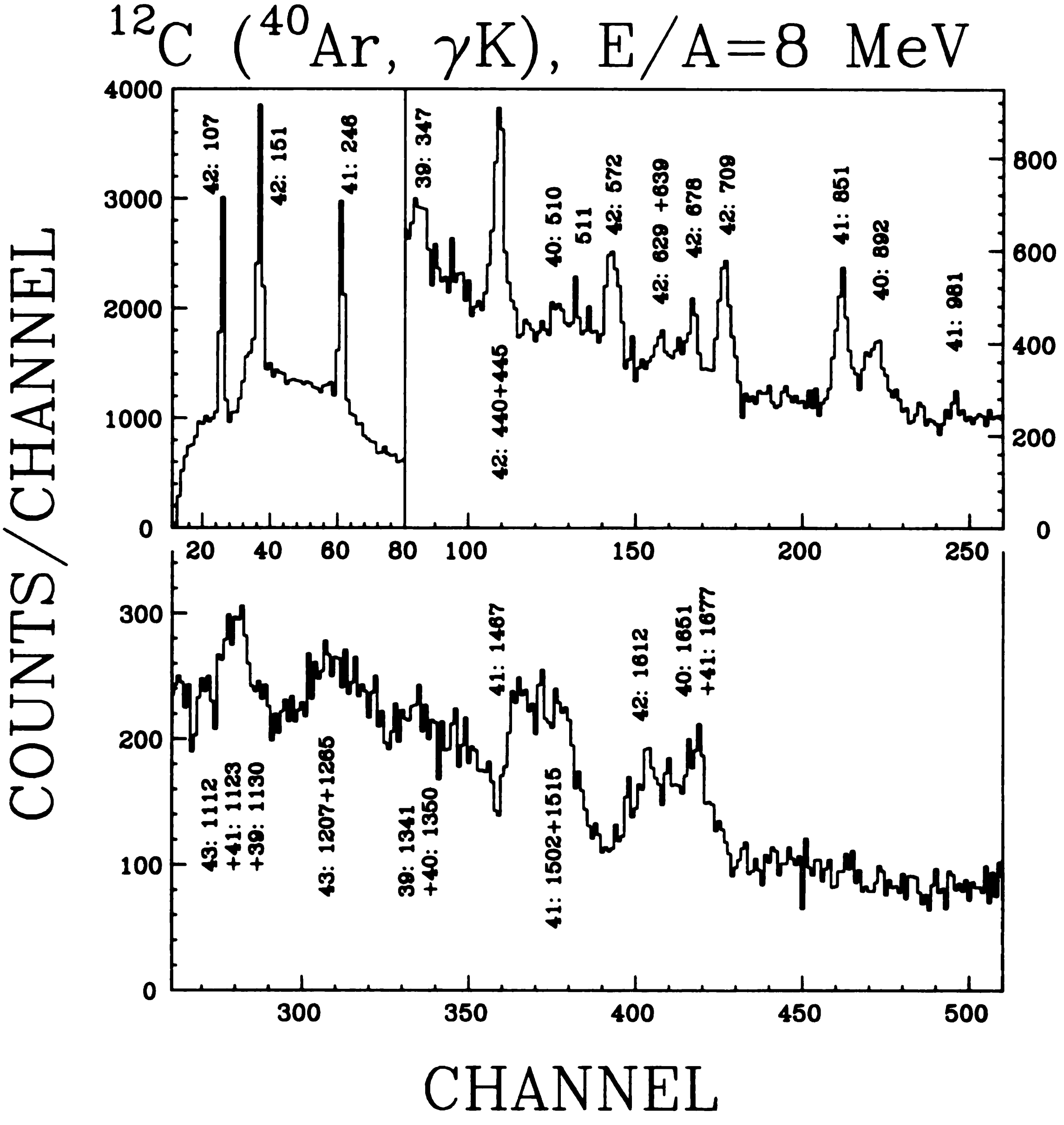

Figure V.3.4 Same as in Figure Figure V.3.1 with Potassium (K).

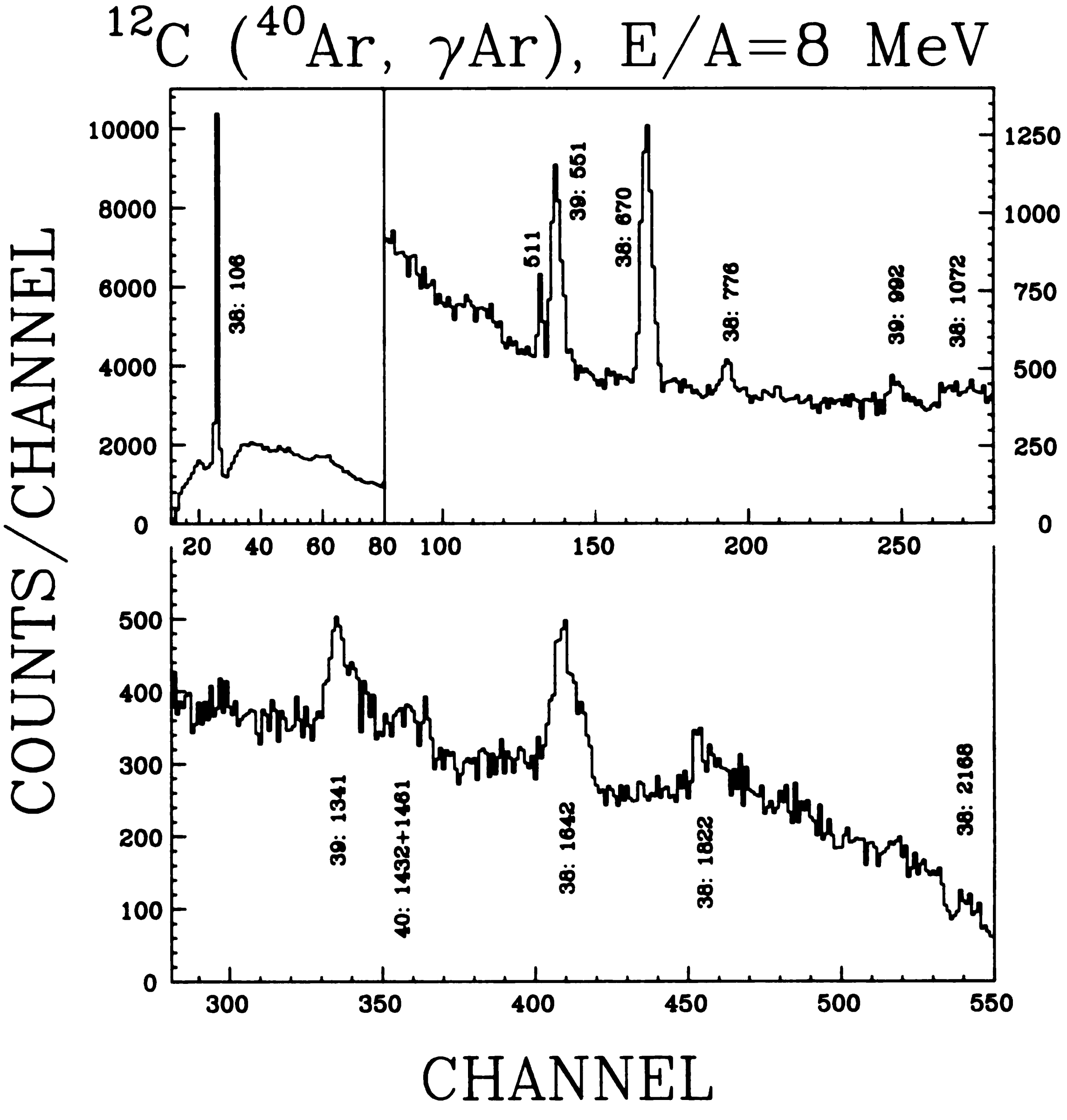

Figure V.3.5 Same as in Figure Figure V.3.1 with Argon (Ar).

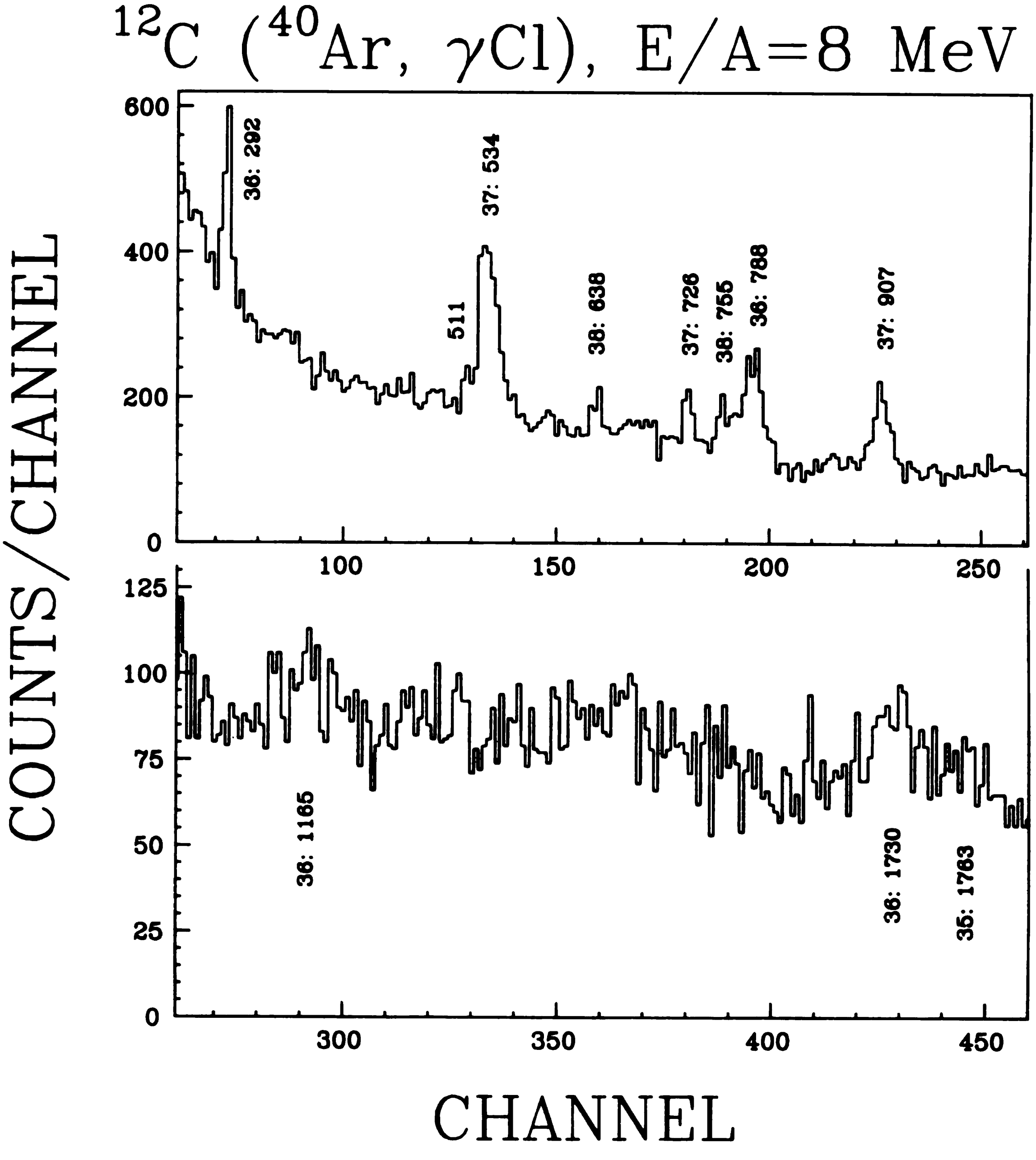

Figure V.3.6 Same as in Figure Figure V.3.1 with Chlorine (Cl).

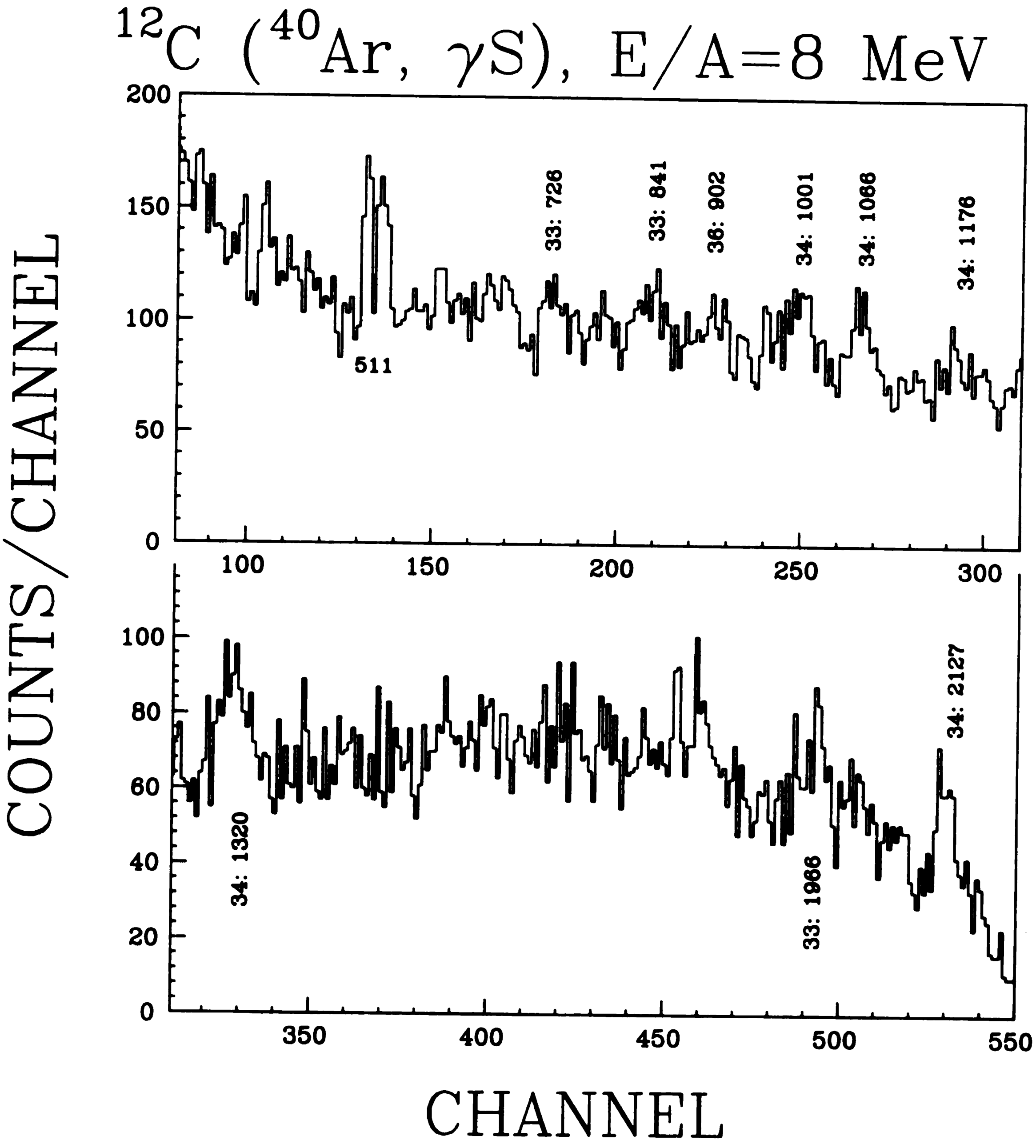

Figure V.3.7 Same as in Figure Figure V.3.1 with Sulfur (S).

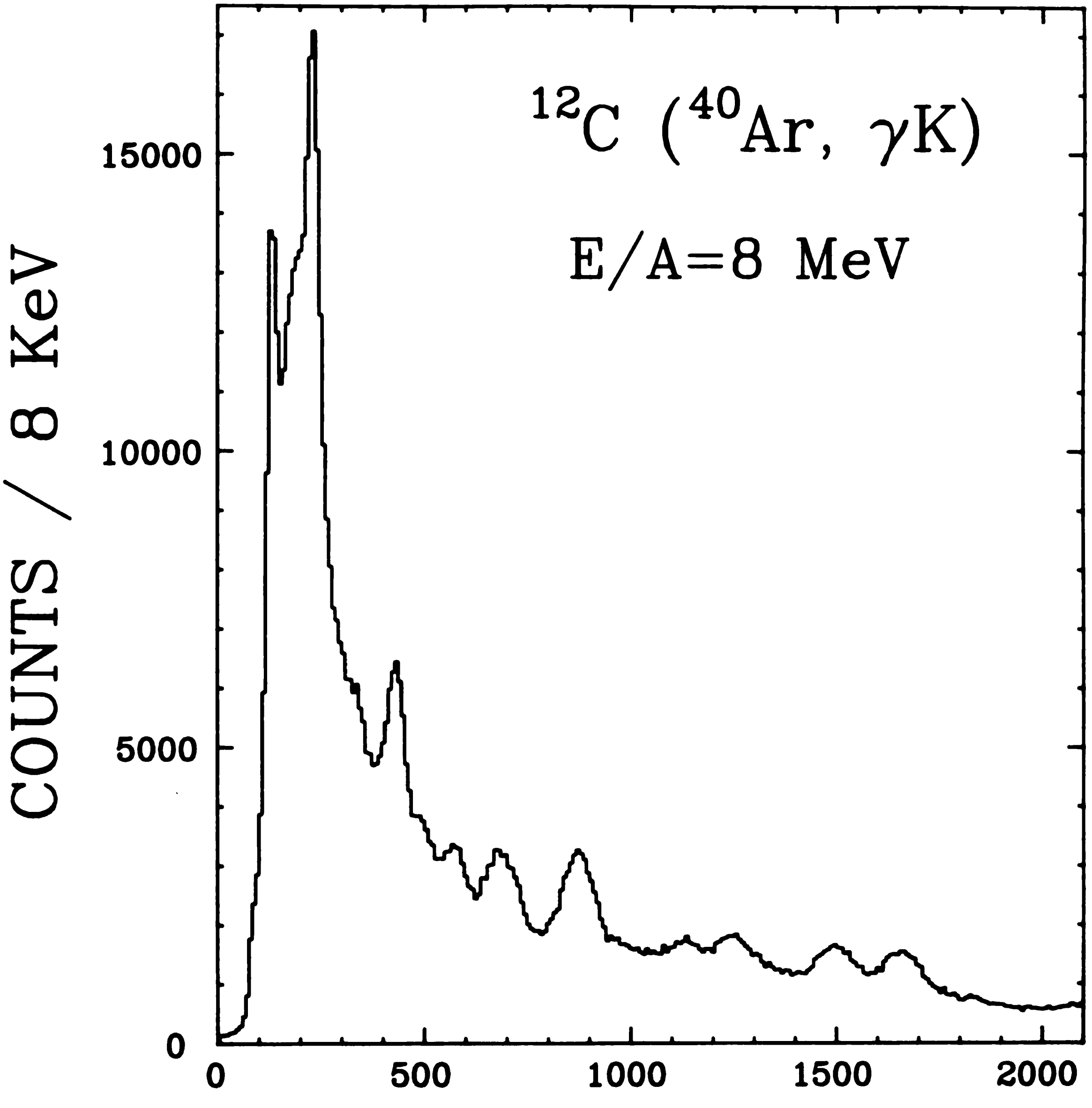

Figure V.3.8 Doppler-shift corrected γ-ray energy spectra (NaI) in coincidence with Potassium (K). a) At E/A=8 MeV.

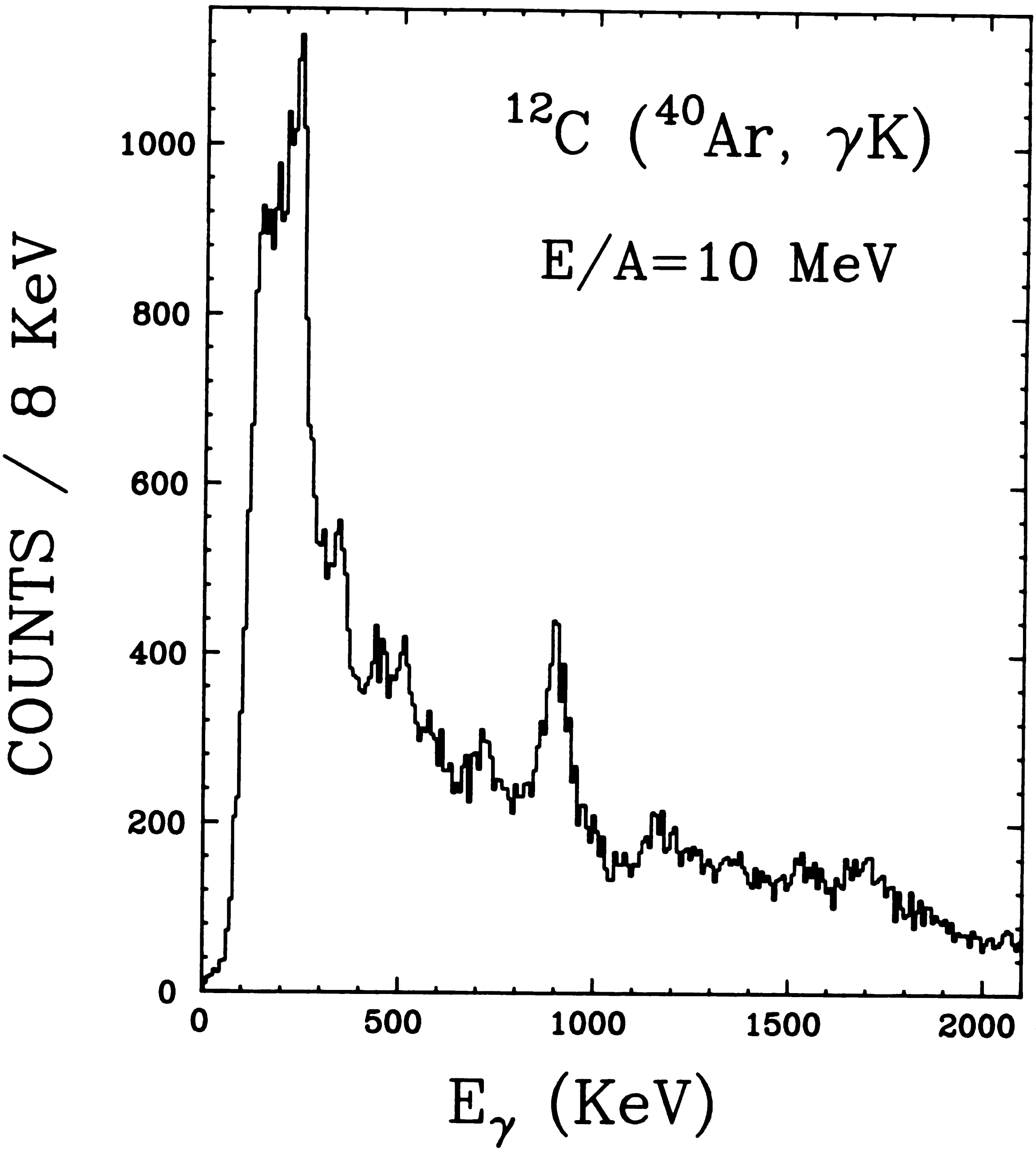

Figure V.3.8 (cont'd.) b) At E/A=10 MeV.

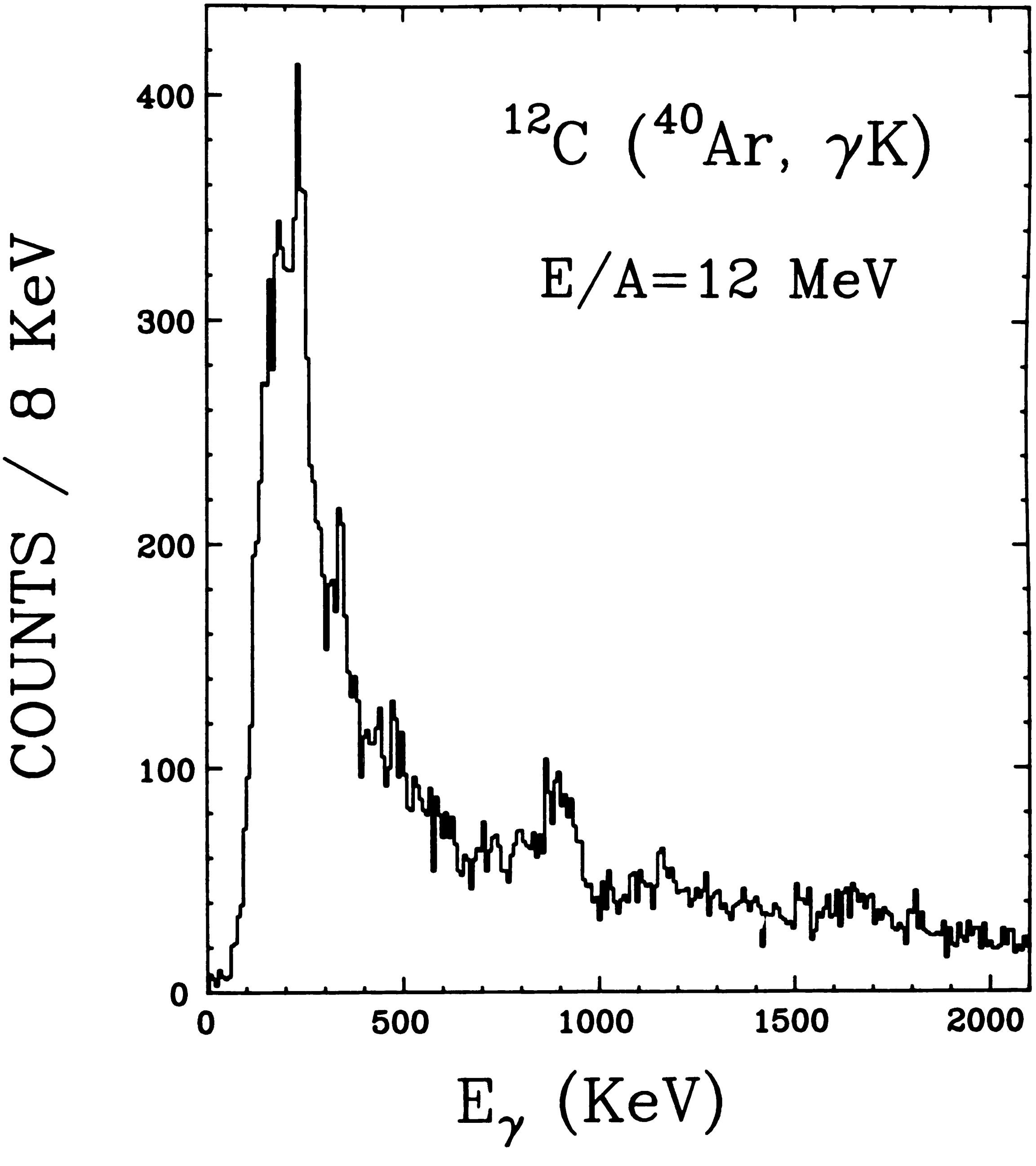

Figure V.3.8 (cont'd.) c) At E/A=12 MeV.

Table V.3.1 Relative gamma-ray intensities at E/A=8 MeV. a) For ^{45}Ti.

E_γ (KeV)	Decay	B.R. (%)	N_γ	Eff. (%)	I_γ	
					observed[1]	CASC.[2]
585	$3.60(\frac{15}{2}^-) \rightarrow 3.02(\frac{13}{2}^-)$	82	45±20	0.322	14±6	15
1547	$3.02(\frac{15}{2}^-) \rightarrow 1.47(\frac{11}{2}^-)$	80	24±12	0.128	19±9	17
1469	$1.47(\frac{11}{2}^-) \rightarrow 0(\frac{7}{2}^-)$	100	25±10	0.135	19±7	19

[1] Total number of gamma rays emitted during the entire runs through 4π angle (unit: 1000 counts).

[2] Predictions by the CASCADE code [Pü77] (normalized to E_γ=1469 KeV).

Table V.3.1 (cont'd.) b) For ^{46}Ti.

E_γ (KeV)	Decay	B.R. (%)	N_γ	Eff. (%)	I_γ	
					observed[1]	CASC.[2]
1345	$6.24(10^+) \rightarrow 4.90(8^+)$	100	25±11	0.147	17±8	16
1289	$3.30(6^+) \rightarrow 2.01(4^+)$	100	58±24	0.154	38±16	28
1121	$2.01(4^+) \rightarrow 0.89(2^+)$	100	57±15	0.176	33±8	33
889	$0.89(2^+) \rightarrow 0(0^+)$	100	68±29	0.217	31±13	35

[1],[2] Same as in Part a) except for a normalization to E_γ=1121 KeV.

Table V.3.2 Relative gamma-ray intensities at E/A=8 MeV. a) For ^{44}Sc.

E_γ (KeV)	Decay	B.R. (%)	N_γ	Eff. (%)	I_γ observed[1]	CASC.[2]
546[3]	$4.11(\ ?\ ) \to 3.57(11^+)$	100	85±23	0.346	25±7	
408[3]	$3.98(\ ?\ ) \to 3.57(11^+)$	100	92±25	0.480	19±5	
895	$3.57(11^+) \to 2.67(9^+)$	100	134±45	0.216	57±21	51
1704	$2.67(9^+) \to 0.97(7^+)$	100	72±26	0.117	62±22	59
697	$0.97(7^+) \to 0.27(6^+)$	100	175±27	0.270	65±10	65
350[4]	$0.35(4^+) \to 0(2^+)$	100	101±50	0.573	18±9	4

[1],[2] Same as in Table V.3.1 except for a normalization to E_γ=697 KeV.

[3] Uncertain spin assignment (no predicted value is given).

[4] $\tau_{1/2}$(0.35 MeV)=3.1 ns

Table V.3.2 (cont'd.) b) For ^{45}Sc.

E_γ (KeV)	Decay	B.R. (%)	N_γ	Eff. (%)	I_γ observed[1]	CASC.[2]
1586	$3.69(\frac{19}{2}^-) \to 2.11(\frac{15}{2}^-)$	100	52±20	0.125	50±17	59
870	$2.11(\frac{15}{2}^-) \to 1.24(\frac{11}{2}^-)$	100	182±61	0.221	87±28	87
1237	$1.24(\frac{11}{2}^-) \to 0(\frac{7}{2}^-)$	100	203±30	0.160	127±19	95

[1],[2] Same as in Table V.3.1 except for a normalization to E_γ=870 KeV.

Table V.3.3 Relative gamma-ray intensities at E/A=8 MeV. a) For ^{42}Ca.

E_γ	Decay	B.R.	N_γ	Eff.	I_γ		
(KeV)		(%)		(%)	observed[1]	CASC.[2]	ther.[3]
382	$7.75(11^-) \rightarrow 7.37(10^-)$	100	867±200	0.518	167±39	310	87
815	$7.37(10^-) \rightarrow 6.55(9^-)$	100					
+810	$6.55(9^-) \rightarrow 5.74(7^-)$	72	2338±130	0.235	995±55	960	810
145	$6.55(9^-) \rightarrow 6.41(8^-)$	28	1647±115	0.947	174±12	174	174
916	$6.41(8^-) \rightarrow 5.49(6^-)$	72					
+909	$4.10(5^-) \rightarrow 3.19(6^+)$	67	1700±390	0.211	806±185	407	1180
1644	$5.74(7^-) \rightarrow 4.10(5^-)$	54	585±280	0.121	483±231	279	399
439[4]	$3.19(6^+) \rightarrow 2.75(4^+)$	100	2785±300	0.441	632±68	595	3610
1227	$2.75(4^+) \rightarrow 1.52(2^+)$	99	2359±350	0.161	1465±217	710	5530
1524	$1.52(2^+) \rightarrow 0(0^+)$	100	2090±185	0.130	1608±142	716	8710
1462	$4.72(6^+) \rightarrow 3.25(4^+)$	45	510±210	0.135	378±156	18	362
1729	$3.25(4^+) \rightarrow 1.52(2^+)$	55	577±240	0.115	502±209	13	600

---

[1],[2] Same as in Table V.3.1 except for a normalization to E_γ=145 KeV.

[3] Predictions of thermal distribution with κT=2.76 MeV (normalized to E_γ=145 KeV).

[4] $\tau_{1/2}$(3.19 MeV)=5.4 ns.

Table V.3.3 (cont'd.) b) For ^{43}Ca.

E_γ	Decay	B.R.	N_γ	Eff.	I_γ	
(KeV)		(%)		(%)	observed[1]	CASC.[2]
776	$5.93(\frac{19}{2}^-)\rightarrow 5.16(\frac{17}{2}^-)$	100				
+761	$5.16(\frac{17}{2}^-)\rightarrow 4.39(\frac{15}{2}^-)$	64	485±115	0.247	196±47	64
1076	$2.75(\frac{15}{2}^-)\rightarrow 1.68(\frac{11}{2}^-)$	100	816±130	0.183	446±71	446
1678	$1.68(\frac{11}{2}^-)\rightarrow 0(\frac{7}{2}^-)$	100	963±490	0.118	731±245	692
373	$0.37(\frac{5}{2}^-)\rightarrow 0(\frac{7}{2}^-)$	100	227±100	0.532	43±19	123

[1],[2] Same as in Table V.3.1 except for a normalization to E_γ=1076 KeV.

Table V.3.4 Relative gamma-ray intensities at E/A=8 MeV. a) For ^{40}K.

E_γ	Decay	B.R.	N_γ	Eff.	I_γ	
(KeV)		(%)		(%)	observed[1]	CASC.[2]
1350	$6.23(10^-)\rightarrow 4.88(9^+)$	100	270±120	0.176	185±82	40
510	$4.88(9^+)\rightarrow 4.37(8^+)$	36	354±80	0.372	95±21	34
1651[3]	$2.54(7^+)\rightarrow 0.89(5^-)$	89	342±160	0.120	285±133	321
892	$0.89(5^-)\rightarrow 0(4^-)$	100	1699±220	0.216	787±102	787

---

[1],[2] Same as in Table V.3.1 except for a normalization to E_γ=892 KeV.

[3] $\tau_{1/2}$(2.54 MeV)=1.1 ns

Table V.3.4 (cont'd.) b) For ^{41}K.

E_γ	Decay	B.R.	N_γ	Eff.	I_γ	
(KeV)		(%)		(%)	observed[1]	CASC.[2]
246	$2.77(\frac{13}{2}^+)\to 2.53(\frac{11}{2}^+)$	100	3503±155	0.838	418±19	611
851	$2.53(\frac{11}{2}^+)\to 1.68(\frac{7}{2}^+)$	100	1215±180	0.225	540±80	719
1677	$1.68(\frac{7}{2}^+)\to 0(\frac{3}{2}^+)$	100	928±135	0.118	786±115	786
709	$4.99(\frac{19}{2}^-)\to 4.28(\frac{15}{2}^-)$	100	1418±90	0.266	533±34	460
1502	$4.28(\frac{15}{2}^-)\to 2.77(\frac{13}{2}^+)$	20				
+1515	$4.28(\frac{15}{2}^-)\to 2.76(\frac{11}{2}^-)$	80	856±190	0.131	653±145	543
1467	$2.76(\frac{11}{2}^-)\to 1.29(\frac{7}{2}^-)$	100	1067±180	0.135	790±133	535
1294[3]	$1.29(\frac{7}{2}^-)\to 0(\frac{3}{2}^+)$	100				

[1],[2] Same as in Table V.3.1 except for a normalization to E_γ=1677 KeV.

[3] $\tau_{1/2}$(1.29 KeV)=7.2 ns.

Table V.3.4 (cont'd.) c) For ^{42}K.

E_γ (KeV)	Decay		B.R. (%)	N_γ	Eff. (%)	I_γ	
						observed[1]	CASC.[2]
1043	4.60(9)	→3.56(8)	100	115±50	0.188	198±86	148
1612	3.56(8)	→1.95(7^+)	100	537±225	0.123	437±182	211
572	1.95(7^+)	→1.38(6^+)	100	1123±95	0.329	341±29	260
678[3]	1.38(6^+)	→0.70(5^-)	90	760±165	0.278	273±60	300
440	0.70(5^-)	→0.26(4^-)	96	1534±240	0.440	349±55	349
151	0.26(4^-)	→0.11(3^-)	100	2556±190	0.919	278±21	372
107	0.11(3^-)	→ 0(2^-)	100	3191±380	0.970	329±39	402

[1],[2] Same as in Table V.3.1 except for a normalization to E_γ=440 KeV.

[3] $\tau_{1/2}$(1.38 KeV)=1.1 ns.

Table V.3.5 Relative gamma-ray intensities at E/A=8 MeV. a) For ^{38}Ar.

E_γ (KeV)	Decay	B.R. (%)	N_γ	Eff. (%)	I_γ observed[1]	CASC.[2]	ther.[3]
1822	$6.41(6^+) \to 4.59(5^-)$	100	832±250	0.109	763±229	471	223
106	$4.59(5^-) \to 4.48(4^-)$	90	8500±1600	0.970	876±165	1210	936
776	$4.59(5^-) \to 3.81(3^-)$	10	585±105	0.245	239±43	135	104
670	$4.48(4^-) \to 3.81(3^-)$	100	3690±190	0.281	1310±70	1310	1310
1642	$3.81(3^-) \to 2.17(2^+)$	100	2067±265	0.121	1710±220	1570	1855
2168	$2.17(2^+) \to 0(0^+)$	100	520±160	0.032[4]	1630±500	1760	2701

[1],[2] Same as in Table V.3.1 except for a normalization to E_γ=670 KeV.

[3] Predictions of thermal distribution with κT=2.76 MeV (normalized to E_γ=670 KeV).

[4] Limited detection efficiency.

Table V.3.5 (cont'd.) b) For ^{39}Ar.

E_γ (KeV)	Decay	B.R. (%)	N_γ	Eff. (%)	I_γ observed[1]	CASC.[2]
992	$5.54(\frac{17}{2}^+) \to 4.54(\frac{15}{2}^+)$	100	736±155	0.197	374±79	569
551	$4.54(\frac{15}{2}^+) \to 3.99(\frac{13}{2}^+)$	100	1996±280	0.343	582±82	694
1341	$3.99(\frac{13}{2}^+) \to 2.65(\frac{11}{2}^-)$	100	1271±215	0.147	865±146	865

[1],[2] Same as in Table V.3.1 except for a normalization to E_γ=1341 KeV.

Table V.3.6 Relative gamma-ray intensities at E/A=8 MeV. a) For ^{36}Cl.

E_γ (KeV)	Decay	B.R. (%)	N_γ	Eff. (%)	I_γ observed[1]	I_γ ther.[2]
292	$2.81(6^-) \to 2.52(5^-)$	39	488±51	0.701	70±7	28
1730[3]	$2.52(5^-) \to 0.79(3^+)$	96	250±50	0.115	217±43	173
788	$0.79(3^+) \to 0(2^+)$	100	870±220	0.241	361±91	361
1165	$1.17(1^+) \to 0(2^+)$	100	148±60	0.170	87±35	151

[1] Total number of gamma rays emitted during the entire runs through 4π angle (unit: 1000 counts).

[2] Predictions of thermal distribution with κT=2.76 MeV (normalized to E_γ=788 KeV).

[3] $\tau_{1/2}$(2.52 MeV)=1.6 ns

Table V.3.6 (cont'd.) b) For ^{37}Cl.

E_γ (KeV)	Decay	B.R. (%)	N_γ	Eff. (%)	I_γ observed[1]	I_γ CASC.[2]
726	$5.27(\frac{13}{2}^-) \to 4.55(\frac{11}{2}^-)$	100	270±40	0.260	104±15	288
534	$4.55(\frac{11}{2}^-) \to 4.01(\frac{9}{2}^-)$	100	1240±260	0.354	350±73	340
907	$4.01(\frac{9}{2}^-) \to 3.10(\frac{7}{2}^-)$	69	613±76	0.213	288±36	288

[1],[2] Same as in Table V.3.1 except for a normalization to E_γ=907 KeV.

Table V.3.7 Relative gamma-ray intensities at E/A=8 MeV. a) For ^{33}S.

E_γ (KeV)	Decay	B.R. (%)	N_γ	Eff. (%)	I_γ observed[1]	I_γ ther.[2]
1966	$1.97(\frac{5}{2}^+) \rightarrow 0(\frac{3}{2}^+)$	100	270±60	0.101	267±59	210
841	$0.84(\frac{1}{2}^-) \rightarrow 0(\frac{3}{2}^-)$	100	213±50	0.228	93±22	93

[1] Total number of gamma rays emitted during the entire runs through 4π angle (unit: 1000 counts).

[2] Predictions of thermal distribution with κT=2.76 MeV (normalized to E_γ=841 KeV).

Table V.3.7 (cont'd.) b) For ^{34}S.

E_γ (KeV)	Decay	B.R. (%)	N_γ	Eff. (%)	I_γ observed[1]	I_γ ther.[2]
1001	$5.69(5^-) \rightarrow 4.69(4^+)$	52	375±72	0.195	192±37	136
1066	$5.69(5^-) \rightarrow 4.62(3^-)$	48	300±54	0.184	163±29	126
1320	$4.62(3^-) \rightarrow 3.30(2^+)$	76	376±46	0.150	251±31	252
1176	$3.30(2^+) \rightarrow 2.13(2^+)$	56	213±48	0.168	127±29	127
2127	$2.13(2^+) \rightarrow 0(0^+)$	100	377±80	0.047[3]	802±170	1390

[1],[2] Same as in Part a) except for a normalization to E_γ=1176 KeV.

[3] Limited detection efficiency.

information for these nuclei, and also the calculation again predicts a little larger populations at low-lying states, a calculation of the Boltzmann thermal distribution shows only minor disagreement with the observed data.

The comparable magnitude of the observed cross sections for Si and P, as well as S and Cl, represent a major disagreement with the mass spectra calculated by CASCADE code. As shown in Ch. III, although it is understood that the production of complex fragments with masses lighter than half the compound nucleus is mainly due to the binary-decay process of the composite system [Ch86a, Mc85, So83], the origin of heavy fragments (masses between the symmetric-fission product and the projectile nucleus, e.g., Si, P, S, Cl) is somewhat ambiguous; they could be the binary-decay reaction partners of the complex fragments or residual fragments of the composite system in the incomplete fusion rather than in the complete fusion. Perhaps both processes are responsible for the production of these fragments [Mi85]. This is supported by the large yields of these fragments (Si, P, S, Cl, etc.) in comparison with those for the complex fragments (Li, Be, B, etc.). If the binary-decay process was the main channel to populate these less heavy residual fragments, the yields for these fragments should have been comparable to those for the complex fragments. Massive cluster transfer reactions with distinct Q-values and high, but less than ℓ_{cr}, angular momenta in the entrance channel have been introduced by Morgenstern et al. [Mo86b] in order to obtain a new insight into the reaction mechanism of incomplete-fusion events. However, without much detailed knowledge of the incomplete-fusion mechanism, for example, break-up of the target nucleus or the projectile nucleus, any attempt to estimate the contribution from the incomplete-fusion process may not be plausible. In Ch. III, the average velocity for the heavy residual fragments at a small angle (θ=6° in Ref. Mo84b, θ=2.5° in Ref. Mo86b, and θ=11° in the present experiment) seem to differ from one to another, and this complicates the determination of the average momentum transfer.

Most gamma-ray peaks observed in coincidence with heavy residual fragments turned out to belong to the transitions between high-spin states, especially along the yrast-lines, which agrees with the basic assumption of the statistical model. However the transitions from the lower-spin states to the higher-spin states become observable as the mass of the heavy fragments decreases. Predictions by the CASCADE code [Pü77] seem to agree roughly with the experimental data for the population distribution of the high-spin states in isotopes of Ti and Sc. Disagreement arises for some isotopes with $Z < 21$. In this less heavy residual fragment region, the statistical model [Pü77] predicts, in general, larger populations for higher-lying states or smaller ones for lower-lying states. A thermal calculation, which is based on the assumption of the Boltzmann distribution with κT=2.76 MeV, which is predicted for E/A=8 MeV in the Fermi gas model, generally predicts the opposite way; smaller populations for high-lying states or larger ones for lower-lying states. Uncertainties in the level information do not seem to explain the discrepancy for the latter case. However, the rough agreement of the data with the thermal calculation for sulfur isotopes may imply that the binary-decay process becomes more important in the fragment forming channel as the mass gets lighter in this heavy residual fragment region. The surprising result for ^{38}Ar, which shows a rough agreement between the CASCADE code prediction and the observed data, may be interpreted to mean that the compound-nucleus decay dominates in the production of fragments of this nucleus. This may be also supported by the larger gamma-ray intensities for ^{38}Ar than for ^{39}Ar, which is consistent with the CASCADE code calculation.

In conclusion, the CASCADE statistical model calculation predicts the population distributions of the nuclear states in the heavy residual fragments with masses close to the maximum mass in the reaction. This indicates that the statistical emission of the very light particles from the complete-fusion product (compound nucleus) is a dominant process in the production of those heavier residual fragments. However neither the CASCADE code alone nor the Boltzmann thermal distribution with the Fermi gas model temperature alone shows major agreement with the data for fragments of $Z<21$. Perhaps the incomplete-fusion process may contribute significantly to the production of these less heavy residual fragments [Mi85]. Alternatively, as no attempt has ever been made before to apply the CASCADE code to predict the population distributions of nuclear states in the heavy residual fragments, one may suspect the credibility of the predictions for the population distributions of nuclear states by the model. Nonetheless, an indication of the resemblance of the population distributions among the low-lying states in the less heavy residual fragments to the Boltzmann thermal distribution and a rough agreement between the data and thermal calculation for sulfur isotopes may be taken to imply that the binary-decay process of compound nucleus also plays an appreciable role in the production of the heavy residual fragments, and possibly a major role as the mass gets lighter.

CHAPTER VI: SUMMARY AND CONCLUSIONS

In continuation of a study of the statistical equilibrium in the nuclear system [Mo86a], the reaction of ^{40}Ar + ^{12}C at E/A=8, 10, and 12 MeV was studied. Gamma-ray energy spectra were obtained for gamma-rays in coincidence with complex fragments and heavy residual fragments. Particle singles inclusive spectra for the entire mass region ($3 \leq Z \leq 22$) were also obtained owing to the excellent particle identification of the silicon surface barrier particle telescopes. The use of the reverse kinematics in the present experiment enabled the detection of the heavy residual fragments. Population distributions of nuclear states in complex fragments up to the symmetric-fission limit and also those in heavy residual fragments are investigated for the first time by the measurement of the gamma-ray intensities.

Diagrams of the observed peak velocities for complex fragments indicate the existence of a Coulomb velocity which is determined mainly by the Coulomb repulsion energy in the binary decay process. The rough coincidence between the center of the Coulomb velocities and the origin of center-of-mass frame is taken as evidence that the complex fragments are produced mainly from the compound nuclei via binary-decay processes. A rough agreement between the median velocity of the backward-scattering and forward-scattering peaks and the calculated value of $V_{CM}\cos\theta_{lab}$ enhances the characterization of compound-nucleus emission for complex fragments. No major differences in the velocity diagrams or the comparison of median velocities are observed between different beam energies.

Analysis of the simultaneous events for complex fragments in the particle singles runs provides another dimension in a study of the origin of these fragments. These events belong mostly to either between telescope-1 and 4 or between telescope-2 and 3, which define two scattering planes that intersect along the beam line. Very few simultaneous events of complex fragments with large values of Z_1+Z_2 were observed in the combinations of telescopes which define planes out of the beam line. This indicates that the moving source of the complex fragments must proceed in the beam direction. For the events with smaller Z_1+Z_2, comparatively large contribution from the "out-of-plane" combinations is observed, which may be due to the incomplete fusion or continuous light particle emission after binary decay from the compound nucleus; in both cases, the simultaneous events are not necessarily confined to the "in-plane" combinations. A large number of events with total charge ($Z=24$) were observed at $E/A=8$ MeV for intermediate fragments ($Z>6$), while few were observed at $E/A=10$ and 12 MeV. The estimated average values of Z_1+Z_2 (about 23, 22, and 21 at $E/A=8$, 10, and 12 MeV, respectively) are roughly consistent with the prediction basing on the complete-fusion reaction.

The shift in the centroid velocity of heavy residual fragments away from $v_{CM}\cos\theta_{lab}$ is usually considered to be due to incomplete fusion in the entrance channel [Hi87, Mo84b]. At $\theta_{lab}=11°$, the measured centroid velocities for various fragments deviate from the predicted values. An obvious trend is that, as the mass increases, the centroid velocity decreases with respect to the predicted velocity of $v_{CM}\cos\theta_{lab}$, which indicates a tendency of the projectile break-up in the incomplete fusion. This result disagrees with the abrasion model [Ch87a] and also with the results presented in Ref. Mo84b, in which a tendency of the target break-up in the reverse kinematics is exhibited. Hopefully, further measurements of the cross sections of evaporation residues with a wider mass range at various angles will help to solve this puzzle.

As an alternative to the moving source fits [We82, Ja83] for the complex fragments, the kinetic energy spectra in the center-of-mass frame were fitted by a Maxwell-Boltzmann function in order to check the internal consistency of the slope parameters between complex fragments. The range of values was 2.7MeV-3.7MeV at E/A=8MeV, 3.4MeV-4.2MeV at E/A=10MeV, and 3.5MeV-4.5MeV at E/A=12MeV, which shows the higher slope parameter for the higher beam energy. A general trend that the slope parameter decreases as the mass of the complex fragments gets heavier at the same beam energy, which implies the lower temperatures for the heavier complex fragments, are understood by the time evolution of the temperature in a hot-equilibrated nuclear system [Bo86]. Nevertheless, the slope parameters are very comparable to the predicted temperatures by the Fermi Gas model, which are 2.8, 3.1, and 3.5 MeV at E/A=8, 10, 12 MeV, respectively, after taking the rotational energy into account. The Coulomb shift parameter from the fitting is in a rough agreement with the calculated Coulomb barrier potential for each isotope.

The relative population distribution of nuclear states among the bound states were studied by the measurement of the gamma-ray intensities in coincidence with the complex fragments. The deduced temperatures, which reflect the relative populations of nuclear states under the assumption of a simple Boltzmann distribution, are shown for a summary in Figure VI.1.1 for the entire complex fragment region. For ^{7}Li, ^{7}Be, and ^{10}B, the deduced temperatures show a good agreement with the predicted temperatures under the statistical equilibrium and also with the slope parameters up to E/A=10 MeV. Comparison of this result with a earlier study by Morrissey et al. [Mo86a] shows that these fragments are produced from the equilibrated compound system, however a correction must be made in the predicted temperatures in the Fermi gas model by the subtraction of the rotational energy from the maximum possible excitation energy in the full-momentum transfer reaction. At E/A=12 MeV, while the temperature from ^{10}B roughly agrees with that predicted, those from ^{7}Li and ^{7}Be are significantly lower than predicted. This is consistent in part with the result in Ref. Mo86a, in which Morrissey et al. observed low temperatures from population distributions at E/A=12 MeV and higher beam energies, however in the present data the light fragments (^{7}Li, ^{7}Be, and ^{10}B) did not give the same temperature at E/A=12 MeV. This discrepancy is understood as to be due to the effect of preferential feeding from higher-A nuclear systems on the population distributions of these fragments. In the determination of the ^{7}Li gamma-fraction, contamination of the primary population of ^{8}Be ground state to the ^{7}Li singles inclusive spectra has been taken into account by means of a statistical theory [To88, Ha87] and a Monte-Carlo simulation [Bl86], and it has been estimated to be 10% at E/A=8 MeV, 4% at E/A=10 MeV, and negligible at E/A=12 MeV.

This study has been extended more broadly in the present experiment by the observation of the relative population of nuclear states in the intermediate fragments (A>12). Temperatures extracted from the gamma-ray intensities in coincidence with ^{16}N, ^{17}O, ^{18}O, ^{19}F, ^{20}Ne, ^{21}Ne,

^{22}Ne, and ^{23}Na show a fluctuation ranging from 0.2 MeV to infinity. No significant difference is observed between different beam energies, which implies that the fluctuation may be due to some other physical effect; in this thesis, a qualitative investigation regarding the effect of the preferential feeding to certain states from the higher-A nuclear unbound states [Ha88, Ha87, Mo85a, Mo84a, St83] on the measured temperature has been carried out. The quantum statistical model [Fi87, St83] looks successful in explaining this. Especially, as shown in Figure IV.4.4b, the low gamma-fraction predicted by the quantum statistical model for ^{17}O $[0.841(\frac{1}{2}^+) \rightarrow 0(\frac{5}{2}^+)]$ agrees remarkably well with the data, while the predicted gamma-fraction from the primary distribution is much higher than the experimental result. Low temperatures from ^{7}Li and ^{7}Be at E/A=12 MeV may also be due to the preferential feedings to the ground states of these mirror nuclei. However, the model appears to overestimate the preferential feedings to certain states in certain nuclei. In conclusion, the observed relative population distributions of nuclear states in the complex fragment region indicate that these fragments are produced from the equilibrated compound system, however the preferential feedings from the higher-A nuclear systems may have to be taken into account in the determination of the nuclear temperatures.

Finally, the observed relative population distributions of bound states in the heavy residual fragments are compared with the CASCADE code calculation [Pü77]. The predicted yrast-line dominance of the gamma-ray transitions agrees roughly with the data for the nuclei close to the compound nucleus, which indicates that those fragments are formed from the compound nuclei in the full-momentum transfer reactions through the statistical emission of the very light particles. The enhancement of the states inside the yrast line and also of the low-lying states are indicated only for nuclei far lighter than the compound nucleus. One does not see any radical change between any neighboring isotopes, however, one does see a notable trend of changing from the yrast-line dominant population distributions to the Boltzmann distributions. The Boltzmann distribution could be accidentally just a combination of the population distributions from the compound nuclei in the complete fusion and from the composite systems in the incomplete fusion with various momentum transfers [Mo86b]. No further and more specific conclusions regarding the production of the heavy residual fragments, for instance, the fraction of the incomplete-fusion reaction with a certain type of cluster transfer, the fraction of fission products, and the overall contribution from the complete-fusion process, have been drawn in the present measurement. It is strongly hoped in this thesis that this new challenging measurement of the relative population distributions of nuclear states in the heavy residual fragments by the detection of the gamma-rays in coincidence with these fragments will help future understanding in this field.

In conclusion, for the low energy reactions up to 12 MeV/nucleon in the present experiment, the complex fragments are mainly produced from the compound nuclei through a binary-decay process. The rough agreement of the measured temperatures with those predicted after taking the rotational energy and the preferential feedings into account indicates that the compound system reaches thermal equilibrium before it starts emitting complex fragments. Heavy residual fragments with masses near the compound nucleus are formed mainly from the compound nuclei via the statistical emission of the light particles. However, as the mass of the residual fragments decreases away from the compound nucleus, contributions from the decay of the composite systems in the incomplete-fusion reactions and also from the binary-decay process of the compound nuclei may be more responsible for the production of the less heavy residual fragments. In addition, it appears that the new nuclear temperature measurement works roughly for fragments of $A>10$, too, however in this region, the nuclear structure is too complicated for a simple thermal model. Future improved measurements of this type will help to understand the physics of statistical equilibrium of hot nuclear matter and its decay modes.

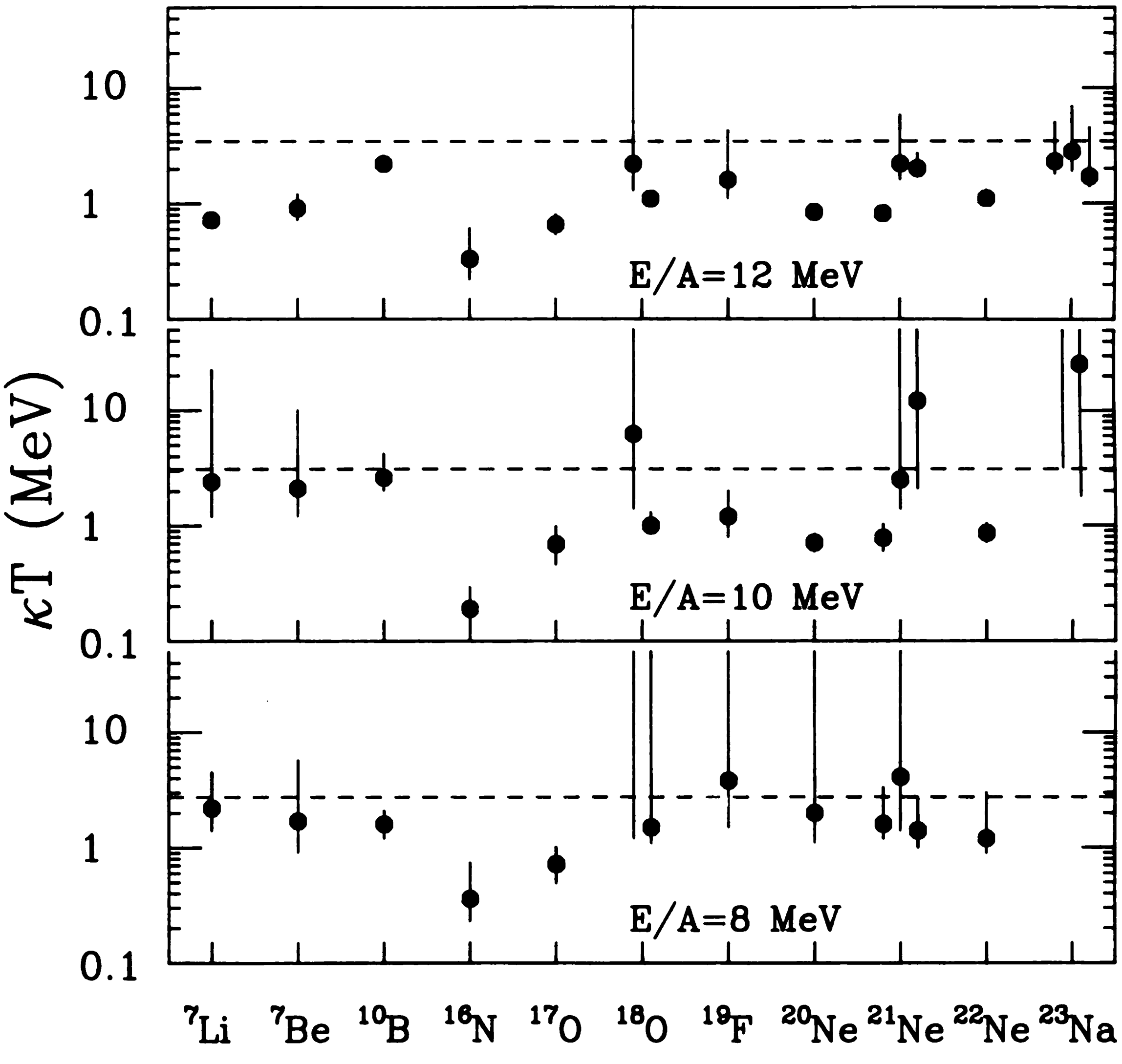

Figure VI.1.1 Summary for the temperature measurements in the complex fragment region. See Figures IV.3.3 and IV.4.3(a-c) for detail.

LIST OF REFERENCES

A

Aa79 H.J.M. Aarts, G.A.P. Engelbertink, H.H. Eggenhuisen, and L.P. Ekström, Nucl. Phys. A321, 515 (1979)

Aj83 F. Ajzenberg-Selove, Nucl. Phys. A392, 1 (1983), and references therein

Aj84 F. Ajzenberg-Selove, Nucl. Phys. A413, 1 (1984), and references therein

Aj85 F. Ajzenberg-Selove, Nucl. Phys. A433, 1 (1985) ; Errtum Nucl. Phys. A449, 155 (1986), and references therein

Aj86 F. Ajzenberg-Selove, Nucl. Phys. A460, 1 (1986), and references therein

B

Ba74 R. Bass, Nucl. Phys. A231, 45 (1974)

Be78 A.H. Behbehani, A.M. Al-Naser, C.J. Lister, P.J. Nolan, and J.F. Sharpey-Schafer, Phys. Lett. 74B, 219 (1978)

Be79 A.H. Behbehani, A.M. Al-Naser, A.J. Brown, L.L. Green, A.N. James, C.J. Lister, N.R.F. Rammo, J.F. Sharpey-Shafer, L.H. Zybert, R. Zybert, and P.J. Nolan, J. Phys. (London) G 5, 1117 (1979)

Bi75 J.N. Bishop and H.T. Fortune, Phys. Rev. Lett. 34, 1350 (1975)

Bl86 C. Bloch, W. Benenson, E. Kashy, D.J. Morrissey, R.A. Blue, R.M. Ronningen, and H. Utsunnomiya, Phys. Rev. C 34, 850 (1986).

Bo84 David H. Boal, Phys. Rev. C 30, 749 (1984)

Bo86 David H. Boal and Julian C. Shillcock, Phys. Rev. C 33, 549 (1986)

Br76 H.C. Britt, B.H. Erkkila, R.H. Stokes, H.H. Gutbrod, F. Plasil, R.L. Ferguson, and M. Blann, Phys. Rev. C 13, 1483 (1976)

Bu55 U.L. Businaro and S. Gallone, Nuovo Cimento 1, 629 (1955)

C

Ch83 Y. Chan, M. Murphy, R.G. Stokstad, I. Tserruya, S. Wald, and A. Budzanowski, Phys. Rev. C 27, 447 (1983)

Ch86a R.J. Charity, M.A. McMahan, D.R. Bowman, Z.H. Liu, R.J. McDonald, G.J. Woznaik, L.G. Moretto, S. Bradley, W.L. Kehoe, A.C. Mignerey, and M.N. Namboodiri, Phys. Rev. Lett. 56, 1354 (1986)

Ch86b C.B. Chitwood, D.J. Fields, C.K. Gelbke, D.R. Klesch, W.G. Lynch, M.B. Tsang, T.C. Awes, R.L. Ferguson, F.E. Obenshain, F. Plasil, R.L. Robinson, and G.R. Young, Phys. Rev. C 34, 858 (1986)

Ch87a Roberty Charity, Nucl. Phys. A471, 225c (1987)

Ch87b R.J. Charity, D.R. Bowman, Z.H. Liu, R.J. McDonald, M.A. McMahan, G.J. Wozniak, L.G. Moretto, S. Bradeley, W.L. Kehoe, and A.C. Mignerey, LBL-22447 (1987)

Ch87c Z. Chen, C.K. Gelbke, W.G. Gong, Y.D. Kim, W.G. Lynch, M.R. Maier, J. Pochodzalla, M.B. Tsang, F. Saint-Laurent, D. Ardouin, H. Delagrange, H. Doubre, J. Kasagi, A. Kyanowski, A. Pèghaire, J. Pèter, E. Rosato, G. Bizard, F. Lefèbvres, B. Tamain, J. Quèbert, and Y.P. Viyogi, Phys. Rev. C 36, 2297 (1987)

Co74 S. Cohen, F. Plasil, and W.J. Swiatecki, Ann. Phys. (N.Y.) 82, 557 (1974).

E

En78 P.M. Endt and C. van der Leun, Nucl Phys. A310, 1 (1978), and references therein

Eg78a H.H. Eggenhuisen, L.P. Ekström, G.A.P. Engelbertink, H.J.M. Aarts, and W.G.J. Langeveld, Nucl. Phys. A299, 175 (1978)

Eg78b H.H. Eggenhuisen, L.P. Ekström, G.A.P. Engelbertink, and H.J.M. AArts, Nucl. Phys. A305, 245 (1978)

F

Fi84 D.J. Fields, W.G. Lynch, C.B. Chitwood, C.K. Gelbke, M.B. Tsang, H. Utsunomiya, and J. Aichelin, Phys. Rev. C 30, 1912 (1984)

Fi86 D.J. Fields, W.G. Lynch, T.K. Nayak, M.B. Tsang, C.B. Chitwood, C.K. Gelbke, R. Morse, J. Wilczynski, T.C. Awes, R.L. Ferguson, F. Plasil, F.E. Obenshain, and G.R. Young, Phys. Rev. C 34, 536 (1986)

Fi87 D.J. Fields, C.K. Gelbke, W.G. Lynch, and J. Pochodzalla, Phys. Lett. 187B, 257 (1987)

Fo66 P.D. Forsyth, H.T. Tu, and W.F. Hornyak, Nucl. Phys. 82, 33 (1966)

Fo85 H.T. Fortune and Richard Eckman, Phys. Rev. C 31, 2076 (1985)

G

Go78 J. Gosset, J.I. Kapusta, and G.D. Westfall, Phys. Rev. C 18, 844 (1978).

Go81 J. Gomez del Campo and R.G. Stokstad, Oak Ridge National Laboratory Technical Report ORNL-TM-7295 (1981)

Go84 J. Gomez del Campo, J.A. Biggerstaff, R.A. Dayras, D. Shapira, A.H. Snell, P.H. Stelson, and R.G. Stokstad, Phys. Rev. C 29, 1722 (1984)

Gr84 K. Grotowski, Z. Majka, R. Płaneta, M. Szczodrak, Y. Chan, G. Guarino, L.G. Moretto, D.J. Morrissey, L.G. Sobotka, R.G. Stokstad, I. Tserruya, S. Wald, and G.J. Wonzniak, Phys. Rev. C 30, 1214 (1984)

H

Ha75 G.B. Hagemann, R. Broda, B. Herskind, M. Ishihara, S. Ogaza, and H. Ryde, Nucl. Phys. A245, 166 (1975)

Ha87 Detlev Hahn and Horst Stöcker, Phys. Rev. C 35, 1311 (1987)

Ha88 Detlev Hahn and Horst Stöcker, Nucl. Phys. A476, 718 (1988)

He81 P. Herges, H.V. Klapdor, and T. Oda, Phys. Lett. 106B, 167 (1981)

He83 W. Henning, Nucl. Phys. A400, 295c (1983)

Hi87 J.D. Hinnefeld, J.J. Kolata, D.J. Henderson, R.V.F. Jenssens, D.G. Kovar, K.T. Lesko, G. Rosner, G.S.F. Stephans, A.M. van den Berg, B.D. Wilkins, F.W. Prosser, S.V. Reinert, and P.L. Gonthier, Phys. Rev. C 36, 989 (1987)

J

Ja82 U. Jahnke, H.H. Rossner, D. Hilscher, and E. Holub, Phys. Rev. Lett. 48, 17 (1982)

Ja83 B.V. Jacak, G.D. Westfall, C.K. Gelbke, L.H. Harwood, W.G. Lynch, D.K. Scott, H. Stöcker, M.B. Tsang, and T.J.M. Symons, Phys. Rev. Lett. 51, 1846 (1983)

Jo75 Charles J. Joachain, Quantum Collision Theory, North-Holland Publishing Company, 29 (1975)

K

Ka84 J. Kasagi, K. Itoh, T. Kishimoto, M. Sasaki, and H. Ohnuma, Nucl. Phys. A414, 206 (1984)

Ke80 Th. Kern, P. Betz, E. Bitterwolf, F. Glatz, and H. Ropko, Z. Phys. A 294, 51 (1980)

Ki75 H.J. Kim, R.L. Robinson, and W.T. Milner, Phys. Rev. C 11, 2108 (1975)

Kn60 W.J. Knox, A.R. Quinton, and C.E. Anderson, Phys. Rev. 120, 2120 (1960)

L

Le78 Tables of Isotopes, 7th ed., edited by C.M. Lederer and V.S. Shirley (Wiley-Interscience, New York, 1978), and references therein

Li78 C.J. Lister, A.M. Al-Naser, A.H. Behbehani, L.L. Green, P.J. Nolan, and J.F. Sharpey-Schafer, J. Phys. G 4, 907 (1978)

M

Mc85 M.A. McMahan, L.G. Moretto, M.L. Padgett, G.J. Wozniak, L.G. Sobotka, and M.G. Mustafa, Phys. Rev. Lett. 54, 1995 (1985)

Mi85 W. Mittig, A. Cunsolo, A. Foti, J.P. Wieleczko, F. Auger, B. Berthier, J.M. Pascaud, J. Quebert, and E. Plagnol, Phys. Lett. 154B, 259 (1985)

Mo75 Luciano G. Moretto, Nucl. Phys. A247, 211 (1975)

Mo84a D.J. Morrissey, W. Benenson, E. Kashy, B. Sherrill, A.D. Panagiotou, R.A. Blue, R.M. Ronningen, J. van der Plicht, and H. Utsunomiya, Phys. Lett. 148B, 423 (1984).

Mo84b H. Morgenstern, W. Bohne, W. Galster, K. Grabisch, and A. Kyanowski, Phys. Rev. Lett. 52, 1104 (1984)

Mo85a D.J. Morrissey, W. Benenson, E. Kashy, C. Bloch, M. Lowe, R.A. Blue, R.M. Ronningen, B. Sherrill, H. Utsunomiya, and I. Kelson, Phys. Rev. C 32, 877 (1985).

Mo85b David J. Moses, Morton Kaplan, John M. Alexander, D. Logan, M. Kildir, Louis C. Vaz, N.N. Ajitanand, E. Duek, and M.S. Zisman, Z. Phys. A 320, 229 (1985)

Mo86a D.J. Morrissey, C. Bloch, W. Benenson, E. Kashy, R.A. Blue, R.M. Ronningen, and R. Aryaeineyad, Phys. Rev. C 34, 761 (1986).

Mo86b H. Morgenstern, W. Bohne, W. Galster, and K. Grabisch, Z. Phys. A 324, 443 (1986)

Mo87 L.G. Moretto and G.J. Wozniak, LBL - preprint LBL-24558 (1987)

Mo88 L.G. Moretto, M. Ashworth, and G.J. Wozniak, LBL-24722 (1988)

N

Ne70 Donald O. Nellis, W.E. Tucker, and Ira L. Morgan, Phys. Rev. C 1, 847 (1970)

Ne75 J.O. Newton, J.C. Lisle, G.D. Dracoulis, J.R. Leigh, and D.C. Weisser, Phys. Rev. Lett. 34, 99 (1975)

Ne77 J.O. Newton, I.Y. Lee, R.S. Simon, M.M. Aleonard, Y. El Masri, F.S. Stephens, and R.M. Diamond, Phys. Rev. Lett. 38, 810 (1977)

P

Pl74 F. Plasil, Proceedings of the International Conference and Reactions between Complex Nuclei (R.L. Robinson, F.K. Mcgowan, J.B. Ball, J.H. Hamilton, Eds.), 107, North-Holland Publishing Co., Amsterdam (1974), and references therein

Pl79 F. Plasil and R.L. Ferguson, Physics and Chemistry of Fission (Proc. Symp. Jülich, 1979) Vol.1, 521, IAEA, Vienna (1980), and references therein

Po81 A.R. Poletti, E.K. Warburton, and J.W. Olness, Phys. Rev. C 23, 1550 (1981)

Po85 J. Pochodzalla, W.A. Friedman, C.K. Gelbke, W.G. Lynch, M. Maier, D. Ardouin, H. Delagrange, H. Doubre, C. Gregoire, A. Kyanowski, W. Mittig, A. Peghaire, J. Peter, F. Lefebvres, B. Tamain, and J. Quebert, Phys. Rev. Lett. 55, 177 (1985)

Pü77 F. Pühlhofer, Nucl. Phys. A280, 267 (1977)

R

Ra82 N.R.F. Rammo, P.J. Nolan, L.L. Green, A.N. James, J.F. Sharpey-Schafer, and H.M. Sheppard, J. Phys. (London), G 8, 101 (1982)

Ra85 S. Raman, R.F. Carlton, J.C. Wells, E.T. Jurney, and J.E. Lynn, Phys. Rev. C 32, 18 (1985)

Re72 M.J. Renan, J.P. Sellschop, R.J. Keddy, and D.W. Mingay, Phys. Rev. C 6, 12 (1972)

Ro83 G. Rosner, D.G. Kovar, P. Chowdhury, D. Henderson, H. Ikezoe, R.V.F. Janssens, W. Khun, C.S.F. Stephans, B. Wilkins, F. Prosser, Jr., J. Kolata, and J. Hinnefeld, Bull. Am. Phys. Soc. 28, 670 (1983)

Ro84 H.H. Rossner, J.R. Huizenga, and W.U. Schröder, Phys. Rev. Lett. 53, 38 (1984)

S

Si76 R.S. Simon, M.V. Banaschik, P. Colombani, D.P. Soroka, F.S. Stephens, and R.M. Diamond, Phys. Rev. Lett. 36, 359 (1976)

Si86 Arnold J. Sierk, Phys. Rev. C 33, 2039 (1986)

Sm86 M.J. Smithson, D.L. Watson, and H.T. Fortune, J. Phys. (London) G 12, 985 (1986)

So83 L.G. Sobotka, M.L. Padgett, G.J. Wozniak, G. Guarino, A.J. Pacheco, L.G. Moretto, Y. Chan, R.G. Stokstad, I. Tserruya, and S. Wald, Phys. Rev. Lett. 51, 2187 (1983)

So84 L.G. Sobotka, M.A. McMahan, R.J. McDonald, C. Signarbieux, G.J. Wozniak, M.L. Padgett, J.H. Gu, Z.H. Liu, Z.Q. Yao, and L.G. Moretto, Phys. Rev. Lett. 53, 2004 (1984)

St77 R.G. Stokstad, R.A. Dayras, J. Gomez del Campo, P.H. Stelson, C. Olmer, and M.S. Zisman, Phys. Lett. 70B, 289 (1977)

St78 W.A. Sterrenburg, G. van Middelkoop, J.A.G. de Raedt, A. Holthuizen, and A.J. Rutten, Nucl. Phys. A306, 157 (1978)

St83 H. Stöcker, G. Buchwald, G. Graebner, P. Subramanian, J.A. Maruhn, W. Greiner, B.V. Jacak, and G.D. Westfall, Nucl. Phys. A400, 63c (1983)

St85 G.S.F. Stephans, D.G. Kovar, R.V.F. Janssens, G. Rosner, H. Ikezoe, B. Wilkins, D. Henderson, K.T. Lesko, J.J. Kolata, C.K. Gelbke, B.V. Jacak, Z.M. Koenig, G.D. Westfall, A. Szanto de Toledo, E.M. Szanto, and P.L. Gonthier, Phys. Rev. Lett. 161B, 60 (1985)

St86 J.A. Stander, W.J. Naudé, R. Saayman, and J.W. Koen, Z. Phys. A 325, 163 (1986)

T

Tō81 J. Tōke and W.J. Swiatecki, Nucl. Phys. A372, 141 (1981)

To88 M. Tohyama, private communication

V

Va85 A. Vander Molen, R. Au, R. Fox, and T. Glynn, Nucl. Instrum. and Meth. A236, 359 (1985)

Vi79 S.E. Vigdor, D.G. Kovar, P. Sperr, J. Mahoney, A. Menchaca-Rocha, C. Olmer, and M.S. Zisman, Phys. Rev. C 20, 2147 (1979)

Vi82 V.E. Viola, Jr., B.B. Back, K.L. Wolf, T.C. Awes, C.K. Gelbke, and H. Breuer, Phys. Rev. C 26, 178 (1982)

Vo84 R. Vodhanel, M.K. Brussel, R. Moreh, W.C. Sellyey, and T.E. Chapuran, Phys. Rev. C 29, 409 (1984)

W

Wa75 E.K. Warburton, J.J. Kolata, and J.W. Olness, Phys. Rev. C 11, 700 (1975)

Wa81 E.K. Warburton and D.E. Alburger, Phys. Rev. C 23, 1234 (1981)

Wa86 E.K. Warburton, C.W. Beausang, D.B. Fossan, L. Hildingsson, W.F. Piel Jr., and J.A. Becker, Phys. Rev. C 34, 136 (1986)

Wa87 E.K. Warburton, Phys. Rev. C 35, 2278 (1987)

We76 G.D. Westfall, J. Gosset, P.J. Johansen, A.M. Poskanzer, W.G. Meyer, H.H. Gutbrod, A. Sandoval, and R. Stock, Phys. Rev. Lett. 37, 1202 (1976).

We82 G.D. Westfall, B.V. Jack, N. Anantaraman, M.W. Curtin, G.M. Crawley, C.K. Gelbke, B. Hasselquist, W.G. Lynch, D.K. Scott, B.M. Tsang, M.J. Murphy, T.J.M. Symons, R. Legrain, and T.J. Majors, Phys. Lett. 116B, 118 (1982)

We84 G.D. Westfall, Z.M. Koenig, B.V. Jacak, L.H. Harwood, G.M. Crawley, M.W. Curtin, C.K. Gelbke, B. Hasselquist, W.G. Lynch, A.D. Panagiotou, D.K. Scott, H. Stöcker, and M.B. Tsang, Phys. Rev. C 29, 861 (1984)

Wi73 J. Wilczynsky, Nucl. Phys. A216, 386 (1973)

Wi80 W.W. Wilcke, J.R. Birkelund, H.J. Wollersheim, A.D. Hoover, J.R. Huizenga, W.U. Schröder, and L.E. Tubbs, At. Data. Nucl. Data. Tables 25, 389 (1980)

Wo72 G.J. wozniak, H.L. Harney, K.H. Wilcox, and Joseph Cerny, Phys. Rev. Lett. 28, 1278 (1972)

X

Xu86 H.M. Xu, D.J. Fields, W.G. Lynch, M.B. Tsang, C.K. Gelbke, M.R. Maier, D.J. Morrissey, J. Pochodzalla, D.G. Sarantites, L.G. Sobotka, M.L. Halbert, D.C. Hensley, D. Hahn, and H. Stöcker, Phys. Lett. 182B, 155 (1986)